A STUDY OF THE HIGH-TEMPERATURE AUTOIGNITION AND THERMAL DECOMPOSITION OF HYDROCARBONS

By

David Charles Horning

Report No. TSD-135

JUNE 2001

A STUDY OF THE HIGH-TEMPERATURE AUTOIGNITION AND THERMAL DECOMPOSITION OF HYDROCARBONS

by

David Charles Horning

Report No. TSD-135

June 2001

High-Temperature Gasdynamics Laboratory
Department of Mechanical Engineering
Stanford University

Abstract

The autoignition of propane, n-butane, n-heptane, n-decane, and ethylene has been studied in the reflected shock region of a shock tube over the range of 1250-1750 K, 1-6 atm, and mixture compositions of 2-20% oxygen with an equivalence ratio of 0.5 to 2.0. The time of ignition was determined from CH emission (431 nm) traces measured at the shock tube endwall. Ignition time correlations for n-butane and n-heptane have been developed to assess the sensitivity of the ignition delay to a variety of parameters (e.g., temperature, pressure, and mixture composition) and to facilitate comparisons of the current data to previous studies and the predictions of detailed models. The correlations presented herein reveal that the ignition time sensitivities of both n-butane and n-heptane to key parameters are markedly similar, leading to the presentation of a unique correlation form in which the stoichiometric ignition time data for propane, n-butane, n-heptane, and n-decane are correlated into a single expression. Direct comparisons to previous ignition time studies further validate the correlations presented. Also, ignition time measurements for ethylene are presented, which reveal that the ignition time behavior of this fuel is quite dissimilar from that of the n-alkanes.

In addition, the thermal decomposition of propane, n-butane, n-heptane, and n-decane has been studied at a pressure of nominally 1 atm over the temperature range of 1500-2100 K. The temporal variation of ethylene was measured during the pyrolysis of these fuels using a new ultraviolet absorption diagnostic (174 nm). All four n-alkanes were found to rapidly decompose into ethylene, with the ethylene yield increasing with the molecular size of the fuel. An analysis of detailed mechanisms was performed to elucidate the main pathways by which the n-alkanes decompose, and to determine the key reactions that control the predicted ethylene time-history. For the pyrolysis of propane and n-butane, it was found that modifications to the initial fuel decomposition rates greatly improved the agreement between the predicted and measured ethylene time-histories. Also, a comparison of three detailed n-heptane mechanisms

revealed marked differences among these models regarding their predicted time-histories of key species.

Table of Contents

List of Figures

CHAPTER 7

CHAPTER 8

APPENDIX C

List of Tables

Chapter 1

Introduction

Although factors such as the volatility of energy prices and the growing concern for pollution control have motivated the development of alternative energy sources, the combustion of fossil fuels remains the primary source of energy throughout the world, accounting for approximately 85% of the total energy consumption worldwide. In an effort to improve energy efficiency and reduce pollutant emissions, substantial investments have been made in research related to the development and implementation of advanced combustion technologies. To ensure high efficiency and good operational performance are achieved, these new combustion systems must be compatible with the desired operating fuel, which is largely dependent on the ignition characteristics of the fuel.

The ignition of a combustible mixture may be quantified by its ignition delay time, which is defined as the time interval required for the mixture to spontaneously ignite at some prescribed set of conditions. Spontaneous ignition, also referred to as autoignition, results when the chemical interaction of a fuel and oxidizer rapidly accelerates, thereby causing the mixture to ignite. This is in contrast to forced ignition, in which an external source (e.g., sparkplug) is employed to initiate the combustion process. The ignition delay time is essentially a macroscopic measurement of the ignition process, which may be readily obtained by a variety of methods. By varying the set of relevant parameters (e.g., temperature, pressure), the ignition time sensitivity to each parameter may be ascertained, thus enabling the ignition time of a specific fuel to be determined over a range of conditions.

1.1 MOTIVATION

Although numerous ignition time studies have been previously conducted, many hydrocarbon species relevant to practical fuels have not been extensively studied. Thus, it is necessary to expand the current database of ignition time measurements to include a wider range of fuels and conditions. Also, due to the large number of hydrocarbons that exist in practical fuels, it is clearly advantageous to develop a method that will reduce the number of experimental studies needed to determine the ignition delay characteristics of hydrocarbons. For example, if the autoignition behavior of a few representative fuels from a given class of hydrocarbons can be shown to be quite similar, it may not be necessary to study every fuel within this class in great detail.

There is also some concern regarding the interpretation and accuracy of some previous ignition time studies. Certain experimental methods may be susceptible to large measurement errors due to non-idealities inherent in experimental work. Furthermore, advances in technology continuously lead to the development of improved experimental methods, which enable more precise measurements to be obtained. Therefore, it is of interest to obtain ignition time measurements of improved accuracy and reduced scatter in order to increase the quality of the empirical ignition time database.

When performing experimental studies, it is necessary to compare current results to past measurements in order to assess the agreement among studies and build upon past knowledge. However, there is often very little overlap among ignition time studies regarding the experimental conditions at which measurements were obtained, making it difficult to directly compare results. Also, there is currently no standard method by which ignition time results are presented. For example, the method employed by some studies is to develop a correlation that expresses the ignition time of a particular fuel as a function of the relevant parameters. However, the choice of parameters is arbitrary, leading to a variety of different correlation forms, and making it difficult to compare these studies. Establishing a method that enables ignition time measurements to be directly compared when obtained over different conditions would clearly be beneficial.

2

While ignition time measurements are useful in characterizing the ignition process from a macroscopic perspective, a more detailed understanding of the complex reaction mechanisms by which a fuel oxidizes is also necessary. This may be provided by detailed chemical mechanisms, which enable the combustion process to be analyzed on a more microscopic level. These mechanisms may include hundreds of elementary reactions and dozens of individual species, and thus temporal measurements of key species are needed to aid in the development and refinement of these mechanisms. Such measurements also enable a more rigorous validation of these mechanisms than that provided by ignition times alone.

1.2 CURRENT STUDY

High-temperature ignition and thermal decomposition measurements have been obtained for propane, n-butane, n-heptane, n-decane, and ethylene. All measurements were obtained using the reflected shock technique and accompanying emission and absorption diagnostics. Ignition times were measured over the temperature range of 1250-1750 K, pressure range of 1-6 atm, and mixture compositions of 2-20% oxygen with an equivalence ratio of 0.5 to 2.0. Ignition time correlations for n-butane and n-heptane have been developed to assess the sensitivity of the ignition process to a variety of parameters (e.g., temperature, equivalence ratio), and to facilitate comparisons to previous experimental studies and detailed models. These correlations also enable the ignition delay characteristics of different fuels to be directly compared. Ignition time results for propane and n-decane are also presented to provide a more thorough comparison of the ignition time behavior among the n-alkanes. In addition, ignition time measurements are presented for ethylene, which is a species that is predicted to have a major role in the combustion of many hydrocarbons.

The thermal decomposition of propane, n-butane, n-heptane, and n-decane was studied over the temperature range of 1500-2100 K in an argon bath. The time-history of ethylene was measured during the pyrolysis of these fuels using an ultraviolet lamp absorption diagnostic (174 nm). The resulting ethylene time-histories and maximum ethylene yields

measured for each fuel were then utilized to provide a more detailed comparison among the *n*-alkanes, and to aid in the determination of the major chemical channels by which these fuels decompose. The ethylene measurements of each fuel were also compared to the predictions of detailed models to assess the accuracy of these mechanisms and to facilitate the analysis of the experimental data. Also, the initial fuel decomposition reactions of both the propane and *n*-butane mechanisms were adjusted to determine the effect of these reactions on the predicted ethylene time-histories and ignition delays.

Chapter 2

Background

This chapter provides an overview of the various experimental systems utilized to obtain ignition time measurements, and the method of defining the ignition time in each case. In addition, a variety of correlation forms are presented that have been used in previous studies to analyze and present ignition time measurements. This chapter concludes with a discussion of the important uncertainties that should be considered when conducting ignition time studies in shock tubes.

2.1 PREVIOUS EXPERIMENTAL METHODS

Ignition time studies have been conducted using a variety of different experimental methods, such as jet-stirred reactors [1], continuous flow reactors [2-6], rapid compression machines [7-15], constant volume bombs [16-19], and shock tubes [20-25]. Therefore, when comparing ignition time data from different studies, it is important to consider how the experimental method utilized in each study may affect the measured ignition time. For example, depending on the method by which the fuel and oxidizer are mixed, physical processes (i.e., mixing, vaporization, atomization) may have a significant effect on the measured ignition time. Furthermore, because the definition of the ignition time is not unique, studies that utilize similar experimental apparatuses may not necessarily employ the same definition for the ignition time. For example, in some studies the onset of ignition is inferred from a pressure trace, while in others this definition is based on the time-history of an intermediate species (e.g., CH). Thus, different values may be obtained among studies that do not utilize the same criteria to quantify the ignition time.

A jet-stirred reactor (JSR) is often composed of a ceramic cavity, into which a high-speed jet of fuel and air is injected via a small nozzle. The fuel and air are typically premixed prior to entering the reactor, and liquid fuels are often vaporized by a preheater before premixing occurs. Impingement of the jet against the reactor wall causes a vigorous mixing and recirculation of the gases that sustains the combustion process and creates a nearly homogeneous reaction zone.
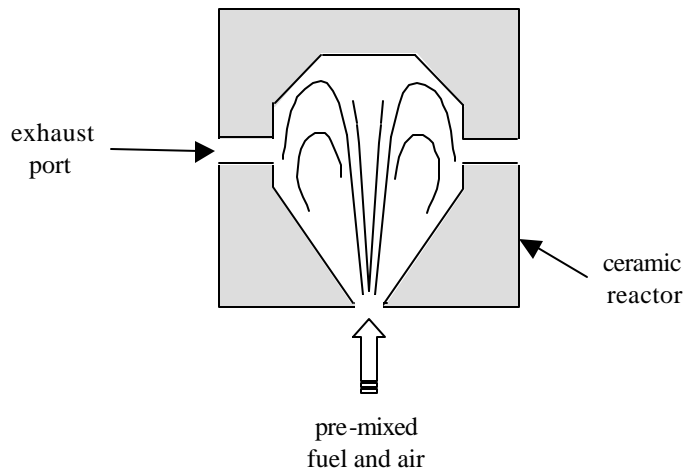
Fig. 2.1 Jet-stirred reactor.

The ignition time in a JSR is determined by increasing the reactor loading (i.e., fuel-air mass flow rate) until the flame is blown out, which may be inferred from the sudden drop in reactor temperature. The definition of the ignition time is based on the reactor residence time, which is calculated from the reactor volume, fuel-air mass flow rate, and the average gas density in the JSR [1].

In a continuous flow reactor (CFR), a blower and preheater force a high-temperature stream of air though a long duct. Downstream of the preheater, the fuel is injected into the air stream through a nozzle. Liquid fuels may either be vaporized before they are injected into the air stream, or special nozzles are employed to rapidly atomize and vaporize the liquid fuel upon injection, thereby minimizing the effect of physical processes on the measured ignition delay

6

time. However, regardless of the phase of the fuel when it is injected in the air stream, there is still a finite physical delay time due to the mixing of the fuel and air that is necessary before ignition is achieved.
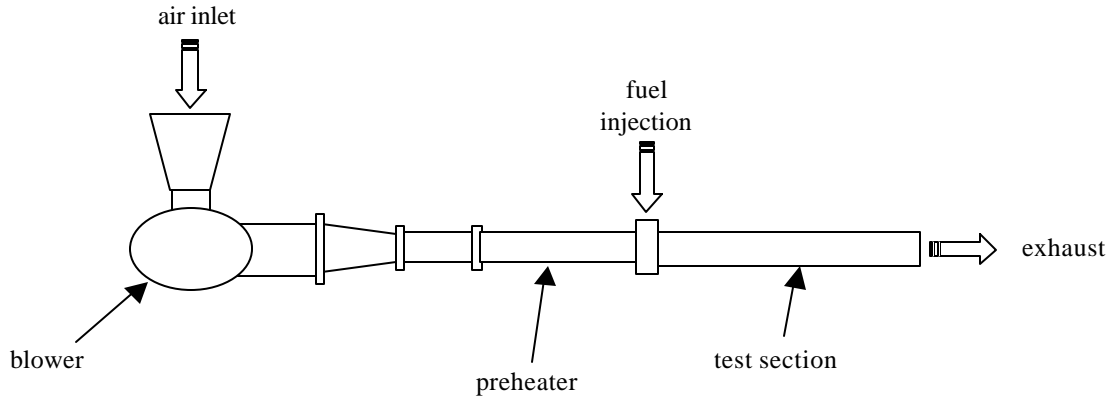
Fig. 2.2 Continuous flow reactor.

The ignition time in a CFR is usually defined as the time interval required for the fuel to ignite, which may be calculated from the average velocity of the air stream and the distance between the fuel nozzle and flame front. The location of the flame front is usually determined visually through windows mounted in the test section, or by adjusting the flow rate of the air stream until the flame front is stabilized at the exit of the test section.

A rapid compression machine (RCM) is a single-shot, piston-cylinder compression device. The compression chamber is initially charged to a prescribed pressure with a gaseous fuel-oxygen-diluent test mixture. The composition of the diluent - which is typically a mixture of carbon dioxide, argon, and/or nitrogen - is varied to regulate the end-of-compression temperature and pressure. Compressed air actuates a high-speed air gun, which is connected to a sliding cam. When the air gun is fired, the cam is pulled forward, forcing an adjoining piston into the compression chamber. This rapid compression of the test mixture causes an abrupt rise in the temperature and pressure of the test gas.
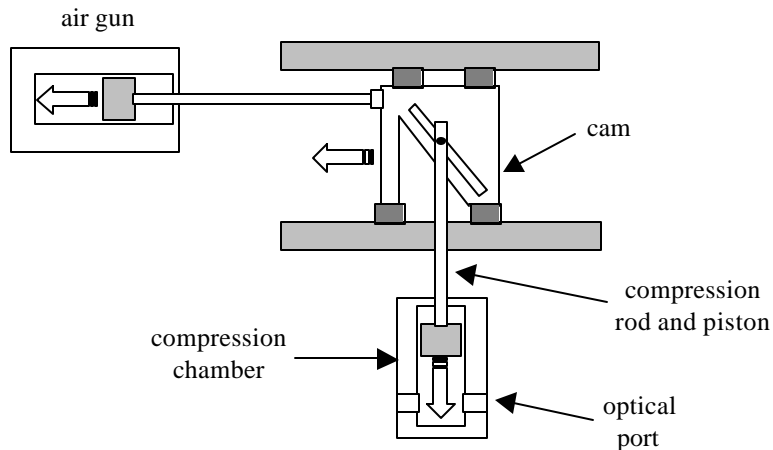
Fig. 2.3 Rapid compression machine.

The ignition time in a RCM is defined as the time interval between the end of the compression stroke and the time of ignition. Ignition is usually inferred from either a pressure trace, or the time-history of an intermediate species (e.g., CH, OH), which is measured via optical ports in the compression chamber. Due to the finite time required for compression (typically 20-60 μs), a RCM is usually utilized in low-temperature (< 1000 K) studies, for which the ignition time is relatively long compared to the compression time.

A constant-volume bomb (CVB) is essentially an electrically-heated pressure vessel. It is initially filled with an oxygen-diluent mixture to a set pressure, and subsequently heated to a prescribed temperature. A high-pressure nozzle then injects a fuel into the CVB, similar to the method employed for direct-injection automotive engines. When testing liquid fuels, the nozzle is often designed to rapidly atomize the fuel, thereby increasing the rate of vaporization and mixing as it is injected into the CVB. However, similar to the CFR method, these physical processes will still contribute to the overall ignition delay, and thus must be considered when interpreting CVB ignition time data.
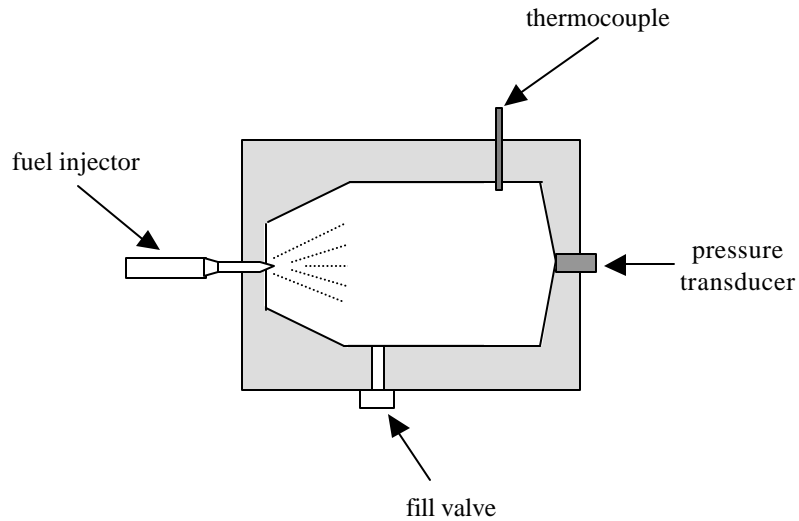
Fig. 2.4 Constant-volume bomb.

The ignition time in a CVB is often defined as the time interval between the injection of the fuel and the initial rise in pressure that results from combustion of the fuel. Due to the difficulty in electrically heating the CVB to high temperatures, a CVB is typically limited to low-temperature (< 1000 K) ignition time studies. Also, when testing liquid fuels, there may be a substantial drop in the temperature and pressure inside the CVB as the fuel vaporizes, which makes it difficult to precisely determine the conditions for the experiment.

A shock tube utilizes a shock wave to almost instantaneously (< 1 μs) compress a test mixture to a desired temperature and pressure. A diaphragm initially separates the shock tube into two sections - a driver section and driven section. The driven section is initially filled with the test mixture, and the driver section is filled with a high-pressure driver gas (e.g., helium) until the pressure differential across the diaphragm causes it to rupture. As the high-pressure driver gas expands into the driven section, a shock wave is formed which travels down the length of the shock tube, and compresses the test gas. When the shock wave reaches the shock tube endwall, it is reflected back towards the driven section, which further compresses the test mixtures. The test-time of most shock tubes is typically limited to under a few milliseconds, and

9

therefore shock tube ignition time studies are often conducted at relatively high temperatures (> 1000 K).
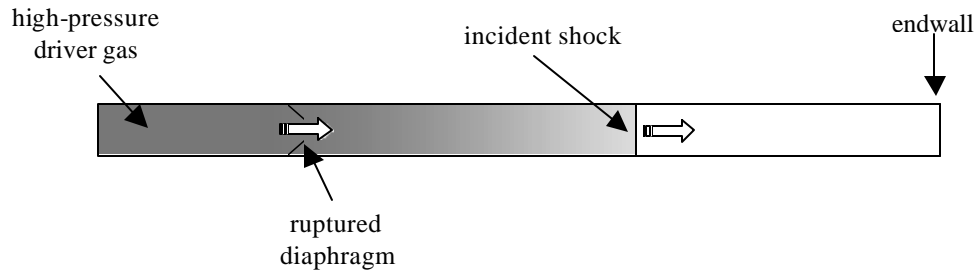
Fig. 2.5 Shock tube.

In shock tubes, ignition time measurements are often obtained in the reflected shock region, near the shock tube endwall, although in some studies the ignition time is measured in the incident shock region. The ignition time is defined as the time interval between shock arrival, which is determined from a pressure trace, and the onset of combustion, which is usually inferred from either a pressure trace or the time-history of an intermediate combustion species (e.g., CH, OH).

2.2 IGNITION TIME CORRELATIONS

A number of different methods have been employed in analyzing ignition time measurements. Perhaps the most useful method involves performing a regression analysis on the experimental data, and using the resultant empirical regression coefficients to express the ignition time as a function of key parameters. The development of correlations facilitates the comparison of ignition time data among studies, and enables the ignition time sensitivity to a particular parameter to be explicitly stated. However, a variety of correlation forms have been previously employed, making it difficult to directly compare the results from different studies. Listed below are examples of some of the correlation forms found in the literature.

$$\boldsymbol{t} = Z \, [fuel]^{\,a} \, [O_2]^{\,b} \, \boldsymbol{r}^{\,r} \, e^{\,B/T} \qquad\qquad [17]$$

$$\boldsymbol{t} = Z \, [fuel]^{\,a} \, [O_2]^{\,b} \, [Ar]^{\,c} \, e^{\,E/RT} \qquad\qquad [20]$$

$$\boldsymbol{t} = (P/RT)^{\,y} \, e^{\,A+B/T} \qquad\qquad [22]$$

$$\boldsymbol{t} = Z \, \boldsymbol{f}^{\,k} \, P^{\,n} \, e^{\,E/RT} \qquad\qquad [27]$$

where Z is simply a scaling constant, $[i]$ is the concentration of reactant i, T is the mixture temperature, $\boldsymbol{f}$ is the mixture equivalence ratio, $\boldsymbol{r}$ and P are the total mixture density and pressure, respectively, R is the universal gas constant, and a, b, c, r, B, E, y, A, k, and n are the empirically determined regression coefficients.

Another application for correlations is that they provide a method of scaling ignition time data to different conditions. This is especially useful when attempting to compare ignition time results that have been obtain at different conditions. For example, ignition time measurements obtained at low pressure may be scaled to higher pressures using the empirically determined pressure sensitivity. However, the uncertainty inherent in scaling ignition time data becomes more problematic if the ignition time sensitivity to a given parameter does not follow a simple mathematical relationship. This may not be explicitly apparent from the results of a regression analysis, and therefore the accuracy of correlations should be analyzed with respect to the experimental data that was utilized to derive them.

Ignition time correlations may also be useful in the development of reduced chemical mechanisms. For example, when a detailed fluid mechanical model is utilized to model the combustion process, a reduced reaction mechanism is typically employed due to the limits of computational power. These reduced mechanisms generally utilize a simple two- or three-step global reaction scheme to model the conversion of the fuel and oxygen to products. Therefore, the accuracy of a reduced mechanism may be improved by employing an ignition time correlation to represent the initial reaction of the fuel and oxygen, with subsequent global reactions accounting for the remainder of the reaction processes, as shown schematically in Fig. 2.6.

11

$$\text{Fuel} + O_2 \quad \underset{\text{correlation}}{\overset{\text{ignition time}}{\Longrightarrow}} \quad CO + H_2 \quad \Longrightarrow \quad CO_2 + H_2O$$
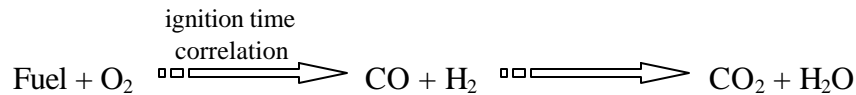
Fig. 2.6 Example two-step reaction mechanism utilizing an ignition time correlation.

2.3 UNCERTAINTIES IN SHOCK TUBE STUDIES

In order to improve the accuracy of the ignition time measurements for the present study, past works were carefully assessed in order to build upon the improvements and recommendations suggested previously. In addition, a sensitivity analysis was performed to determine which uncertainties are likely to be most problematic in obtaining high quality ignition time measurements. These uncertainties have been subdivided into two general classes - parametric uncertainties and measurement uncertainties. Parametric uncertainties are defined as those due to uncertainties in the relevant test parameters (i.e., pressure, temperature, mixture composition), while measurement uncertainties are associated with the inaccuracies inherent in measuring and quantifying the ignition time.

2.3.1 Parametric Uncertainties

The key parameters that determine the ignition time of a combustible mixture are its composition and the local conditions (i.e., pressure and temperature). Based on the results of numerous ignition time studies, it is readily apparent that the ignition time is far more sensitive to temperature than any of the other parameters. Hence, it is concluded that the largest source of error in shock tube ignition time measurements is due to the uncertainty in the post-shock temperature. The ignition time temperature sensitivity is typically specified in terms of a global activation energy, which for many hydrocarbons is in the range of 35-50 kcal/mol. As shown in Table 2.1, significant errors in the measured ignition time will result if the post-shock temperature is not accurately determined.

Table 2.1 Sensitivity of the ignition time to uncertainties in temperature.

12

Temperature	Ignition time uncertainty (at 1400 K)	
uncertainty [K]	E = 35 kcal/mol	E = 50 kcal/mol
5	4.4%	6.2%
10	8.5%	11.9%
20	16.1%	22.2%

Most previous shock tube studies base the uncertainty of the reflected shock temperature on the errors associated with determining the incident shock speed at the shock tube endwall. However, for test mixtures that have a high concentration of species with relatively large specific heat capacities (e.g., liquid fuels), the uncertainty of the test mixture composition must also be considered. For example, for a stoichiometric mixture of 2% *n*-heptane, a 10% uncertainty in the fuel mole fraction will result in approximately a 15 K uncertainty in the reflected shock temperature. Uncertainty in the test mixture composition may be especially important when studying liquid fuels since these fuels often have relatively high heat capacities, and thus have a larger effect on the post-shock temperature. Furthermore, liquid fuels may have very low vapor pressures, which makes it difficult to accurately measure their concentration within a test mixture.

In addition to the test mixture composition, the reflected shock temperature is also dependent on the initial temperature of the test gas and the incident shock velocity. Fortunately, the reflected shock temperature is relatively insensitive to the initial temperature of the mixture. For example, a 1% uncertainty in the initial temperature (i.e., 3 K) will result in an uncertainty of about 1 K in the reflected shock temperature. However, uncertainties in the shock velocity are much more critical, and therefore most shock tubes are designed to measure the incident shock velocity to a very high degree of accuracy. For reflected shock measurements, the velocity of the incident shock at the endwall is achieved by utilizing a series of pressure transducers - spaced axially along the shock tube wall - to determine the velocity profile of the incident shock. This profile is then extrapolated to the endwall using either a linear or a second-order polynomial fit.

Non-ideal viscous effects may also lead to an uncertainty in the reflected shock temperature. That is, the interaction of the reflected shock wave with the incident shock boundary layer may cause the reflected shock temperature to slowly increase throughout the test period, and thus this temperature rise becomes more significant at longer test times. Also, since viscous effects lead to a deceleration of the incident shock velocity, the increase in the reflected shock temperature during the test period is more rapid under conditions in which the shock attenuation rate is high. For the current study, the incident shock attenuation rate was usually less than 1% per meter, and the test times sufficiently short (i.e., < 500 μs), that the increase in the reflected shock temperature is assumed have a negligible effect on the measurements reported here.

Another potential source for error when measuring ignition times is the effect of impurities. For example, an analysis using detailed modeling revealed that adding 10 ppm of H-atoms to an H_2/O_2 mixture may reduce the predicted ignition time by more than 40%. However, for larger hydrocarbons (e.g., n-butane, n-heptane) there was essentially no effect on the predicted ignition time when 10 ppm of H-atom is added to mixtures comparable to those utilized in the current study. Even so, it is advisable that prior to each test the shock tube be thoroughly evacuated to minimize the presence of residual gases from previous tests, and that the shock tube be cleaned on a regular basis to remove any stray diaphragm particles that might accumulate.

2.3.2 Measurement Uncertainties

Shock tube measurements are typically obtained in the reflected shock region, where the ignition time may be defined as the time interval between the passing of the reflected shock wave and the onset of ignition. For highly exothermic mixtures, in which ignition leads to an abrupt increase in pressure, the ignition time may be accurately measured from the pressure trace alone. However, for relatively dilute mixtures, the rise in pressure at the time of ignition is very gradual, which prevents an unequivocal determination of the ignition time. Thus, ignition time measurements that are attained from a pressure record are more appropriate for studying

test mixtures that contain a relatively large amount of fuel and oxygen relative to the diluent, thereby minimizing the uncertainty of the measurement.

In order to measure the ignition delay times of highly dilute test mixtures, a variety of diagnostics have been employed to record the time-history of a select intermediate combustion species - such as CH [23] or OH [24]. The data traces obtained by these diagnostics show a much more abrupt rise at the time ignition, relative to the pressure trace, thus allowing a more precise determination of the ignition time. However, these diagnostics are usually positioned along the shock tube sidewall, which may lead to severe errors in the ignition time measurement. Specifically, it has been shown that ignition time measurements recorded at the shock tube sidewall may be significantly shorter than those measured at the endwall due to perturbations caused by the energy release of the reaction [20]. Thus, the correct ignition delay is that which occurs at the shock tube endwall, where the ignition process proceeds in an essentially quiescent reaction zone until the time of ignition.

In contrast, the ignition delay measured at the sidewall is affected by the energy release and resulting gasdynamics of the combustion wave as it propagates from the endwall and causes an acceleration of the ignition process. The magnitude of the sidewall measurement error has been shown to be significant for highly energetic mixtures, even when the sidewall location is positioned very close to the shock tube endwall [25]. In addition, at lower temperatures, for which the ignition time becomes relatively long, the ignition process may originate as one or more distinct flame kernels due to non-uniformities such as diaphragm particles. These flame kernels may initially form at some distance from the shock tube endwall [22], thereby causing a misinterpretation of the endwall ignition time. Therefore, when employing the reflected shock technique, a method should be utilized that enables the endwall ignition time to be accurately measured.

Chapter 3

Experimental Method

This chapter contains a discussion of the experimental methods utilized in this study. The shock tube facilities are briefly described, followed by a discussion of the diagnostics employed to directly measure the fuel concentration of select test mixtures in the shock tube - IR absorption and gas chromatography. This chapter also contains a description of the diagnostics employed to measure the time-histories of CH (431 nm emission) and ethylene (174 nm absorption). Finally, the method employed to determine the ignition time at both the shock tube sidewall and endwall is presented, and the effect of energy release on the sidewall measurements is revealed.

3.1 SHOCK TUBE FACILITY

All experimental work of the current study was performed at the High Temperature Gasdynamics Laboratory (HTGL) at Stanford University. Except for the study on fuel additives (presented in Appendix C), all measurements presented were obtained in a helium-driven low-pressure shock tube (LPST). The LPST is built of stainless-steel, and is comprised of a 3.7 m driver section and a 10 m driven section, both of which have an inner diameter of 6 inches. A series of five pressure transducers, and four corresponding counter-timers, were utilized to measure the incident shock velocity profile over a distance of 1.5 m from the endwall. The shock velocity at the endwall was calculated by extrapolating the incident shock velocity profile to the endwall using a second-order polynomial fit. Reflected shock conditions were calculated from the one-dimensional shock relations and the Sandia thermodynamic database, which was expanded to include the relevant thermodynamic data for n-heptane and n-decane, as suggested by Burcat [26].

All test gases and liquid fuels were of research grade quality. Mixtures were prepared in a 14 liter stainless-steel tank, and mixed by an electrically-driven stirring rod. Liquid fuels were individually stored in glass containers, which were directly connected to the mixing manifold via an isolation valve. After initially evacuating the mixing tank and manifold, the isolation valve was opened to allow the vapor pressure of the fuel to be drawn into the mixing tank. To minimize the presence of atmospheric air in the fuel containers, a freeze-pump-thaw procedure was employed, which involved freezing each liquid fuel in a liquid nitrogen bath, and evacuating the air from the container.

3.2 FUEL MEASUREMENT

As discussed in Section 2.3.1, ignition time measurements may be subject to a high degree of experimental uncertainty if the composition of the test mixture is not accurately measured. While mixtures composed of gaseous hydrocarbons may be prepared manometrically to a high degree of accuracy, the current study has shown this method may be subject to error when preparing mixtures that are composed of fuels that are in liquid form at ambient conditions. The problem arises when, after initially filling the mixing tank with a liquid fuel vapor, the subsequent addition of the remaining mixture components (e.g., oxygen and argon) causes compression of the fuel vapor beyond its saturation limit. While the partial pressure of the fuel vapor should ideally remain constant as additional mixture components are added, this does not occur since the test gas components do not instantaneously mix. Therefore, the addition of subsequent gases may cause the fuel vapor to partially condense. Although any condensed fuel will eventually evaporate, extra time must be allowed for the gases to mix so as to ensure homogeneity of the test mixture. Furthermore, condensation of the fuel will cause errors in the measured mole fractions of the additional mixture components since the total pressure in the mixing tank will understate the actual molar quantity of the mixture components.

To minimize the condensation of the liquid fuels for the present study, the maximum vapor pressure drawn into the mixing tank was limited to less than 50% of the room temperature vapor pressure of each fuel. Furthermore, subsequent mixture components were added slowly to minimize the compression of the fuel vapor, thus enabling a more accurate measurement of the oxygen and argon mole fractions. This procedure was validated by directly measuring the in-situ fuel concentration of the test mixture in the shock tube using to two different measurement techniques - laser absorption and gas chromatography.

3.2.1 Infrared Absorption

The infrared (IR) absorption diagnostic consisted of a 3.39 μm continuous wave (cw) helium-neon (HeNe) laser. The laser output power (approx. 4.5 mW) was measured by a single thermopile detector with a surface diameter of 10 mm and a power resolution of 1 μW. The in-situ fuel mole fraction X_f of the test mixture was determined from the Lambert-Beer relationship,

$$I/I_0 = e^{-aLPX_f} \qquad \text{[Eq. 3.1]}$$

where I_0 and I are the measured laser intensity before and after filling of the shock tube, respectively, L is the path length traversed by the laser within the shock tube, P is the total fill pressure of the test mixture in the shock tube, and a is the absorption coefficient, per unit length and pressure, of the hydrocarbon to be measured.

The absorption coefficients of n-heptane and n-decane were determined experimentally from the attenuation of the IR laser beam as it passed through an absorption cell that was filled with pure fuel vapor. For each hydrocarbon, a series of absorption measurements were made over a range of fuel vapor pressures, and the absorption coefficient was calculated from the slope of a best-fit line of the laser beam transmittance (I/I_0) versus the pressure of the fuel vapor

in the absorption cell. Absorption cells of both 15 and 70 cm in length were utilized to verify the repeatability and accuracy of the absorption coefficient measurements.

To assess the relative merits of different absorption configurations and to verify the consistency of the measurements, the absorption coefficient of *n*-heptane was obtained using three different experimental set-ups. The first absorption configuration (Fig. 3.1) utilized two indium-antimonide (InSb) IR detectors to enable the intensity of both the reference beam (I_0) and absorbed laser beam (I) to be simultaneous measured. Due to the relatively high sensitivity of the InSb detectors, a neutral density (ND) filter was required to prevent detector saturation and to ensure that the laser power to each detector remained well within its linear response region.
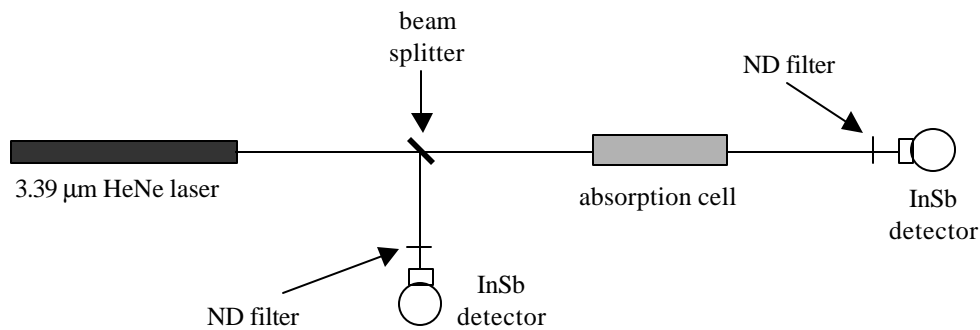
Fig. 3.1 Type I absorption configuration.

Due to the stability of the IR laser output power, a second absorption configuration was tested (Fig. 3.2) in which a single InSb detector was used to measure the IR laser power. The initial laser beam intensity (I_0) was measured with the absorption cell fully evacuated. The cell was then filled with fuel vapor, and the laser beam intensity (I) was recorded over a range of pressures. After the last absorption measurement was obtained, the absorption cell was evacuated to verify that the laser beam intensity had not changed. The laser beam transmittance was then calculated at each recorded pressure using the initial measured value of the laser beam intensity (I_0).
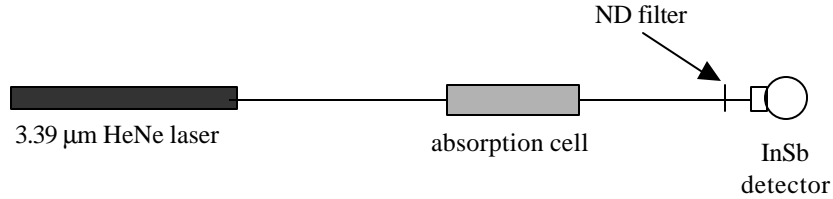
Fig. 3.2 Type II absorption configuration.

The third absorption configuration employed to measure the absorption coefficient of *n*-heptane utilized a single thermopile power meter to measure the laser beam power (Fig. 3.3), similar to the Type II configuration previously discussed. However, the large active surface area of the power meter (10 mm diameter) relative to the InSb detectors (1 mm x 3 mm) greatly facilitated the alignment of the absorption set-up. In addition, the high power capability (20 W) of the thermopile detector obviated the need to attenuate the laser beam with a neutral density filter. However, due the relatively wide spectral range over which the thermopile detector is sensitive (0.19-20 μm), a narrow bandpass filter was required to minimize the amount of background thermal radiation. The transmittance of the IR filter was approximately 80% at 3.36 μm, with a spectral half-width of approximately 0.08 μm.
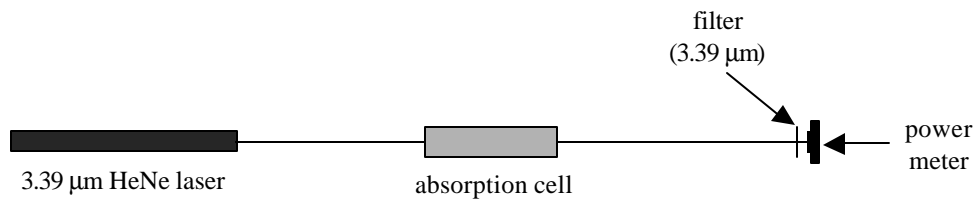
Fig. 3.3 Type III absorption configuration.

A comparison of the *n*-heptane absorption measurements (Fig. 3.4) shows that all three absorption configurations produce essentially the same value for the absorption coefficient. Therefore, due to its relative simplicity and easy alignment, the Type III absorption configuration

20

was used for the *n*-decane absorption measurements and the in-situ shock tube measurements of the gaseous test mixtures derived from liquid fuels.
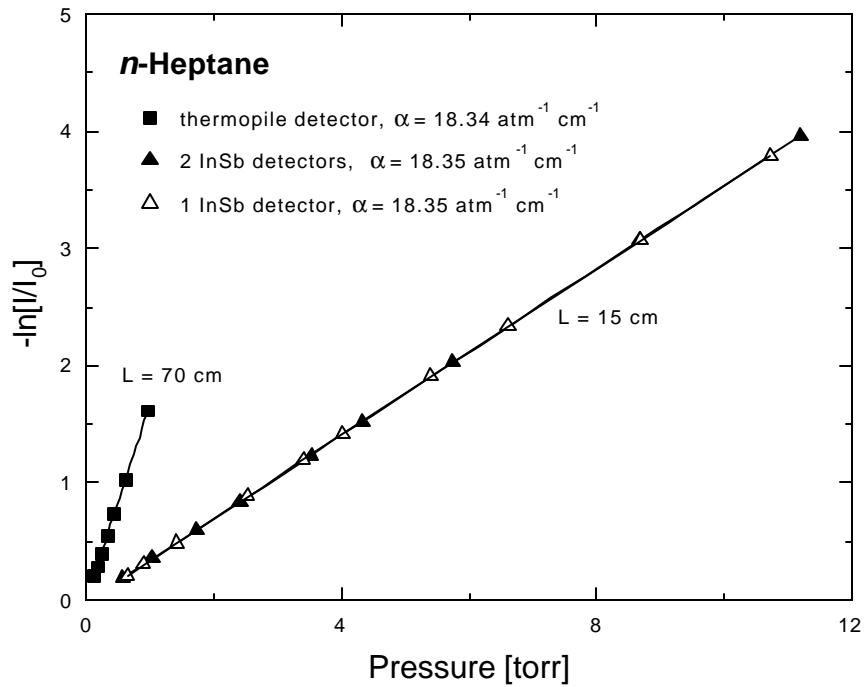
Fig. 3.4 *n*-Heptane absorption measurements at 3.39 mm, 295 K.
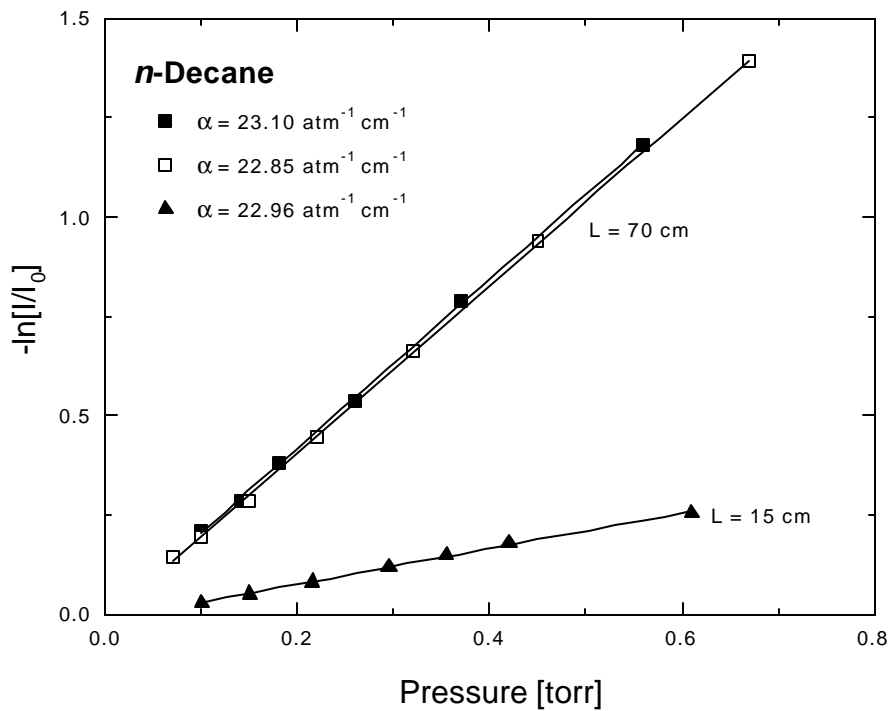
Fig. 3.5 *n*-Decane absorption measurements at 3.39 μm, 295 K.

It is also evident from the absorption measurements that there is excellent agreement between the measurements that were obtained using different absorption cell lengths, which further validates the measurements the reported here. The absorption coefficient of *n*-heptane at 295 K was measured as 18.35 atm^{-1}cm^{-1}, with an uncertainty of less than ±1%. This value is in reasonable agreement with an earlier determination by Jaynes and Beam of 20 atm^{-1}cm^{-1} [28]. The absorption coefficient of *n*-decane at 295 K was measured as 23.0 atm^{-1}cm^{-1}, with an uncertainty of approximately ±1%. This measurement is shown to be much higher than the range of values previously given by Jaynes and Beam, for which the *n*-decane absorption measurements were reported to be susceptible to a high degree of uncertainty given the low vapor pressure of the fuel. In addition, as shown in Table 3.1, the room temperature absorption coefficients of the *n*-alkanes increase with increasing molecular size. Therefore, based on this trend and the higher degree of accuracy achieved in the current study, it is concluded that the value of the *n*-decane absorption coefficient measured in this study is much more reasonable than the earlier determination of Jaynes and Beam.

Table 3.1 Absorption coefficients of *n*-alkane gases at 3.39 μm, 295 K.

n-Alkane	a [atm^{-1}cm^{-1}]	Reference
Ethane	2.7	28
Ethane	2.5	29
Propane	8.3	28
Propane	9.4	29
n-Butane	10.7	29
n-Pentane	13.6	28
n-Pentane	14.5	29
n-Hexane	18	28
n-Heptane	20	28
n-Decane	10-13	28

To determine the effect of pressure broadening on the measured absorption coefficients of *n*-heptane and *n*-decane, a series of tests were conducted in which argon and/or oxygen was added to the fuel vapor in the test cell. It was found that diluting either fuel by a factor of more than 300 had no effect on the measured absorption. In addition, although the absorption coefficient of *n*-alkane gases has been shown to be rather temperature sensitive [29], all absorption measurements were obtained with the test mixture at room temperature, which varied from nominally 70-75 °F. Therefore, the absorption coefficients of *n*-heptane and *n*-decane were not determined at higher temperatures.

As previously mentioned, the absorption configuration that was utilized to verify the fuel concentration of the liquid fuel test mixtures consisted of a single thermopile detector and an accompanying IR filter. The relatively low fuel mole fractions employed for some of the LPST experimentation necessitated the use of a triple-pass absorption system (see Fig. 3.6) in order to ensure sufficient (> 10%) laser absorption, and thus achieve a higher degree of accuracy for the measurement. Due to the slight divergence of the laser beam and the relatively long path length required for the triple-pass configuration, two calcium-fluoride lenses were used to focus the laser beam more directly onto the surface of the thermopile detector.
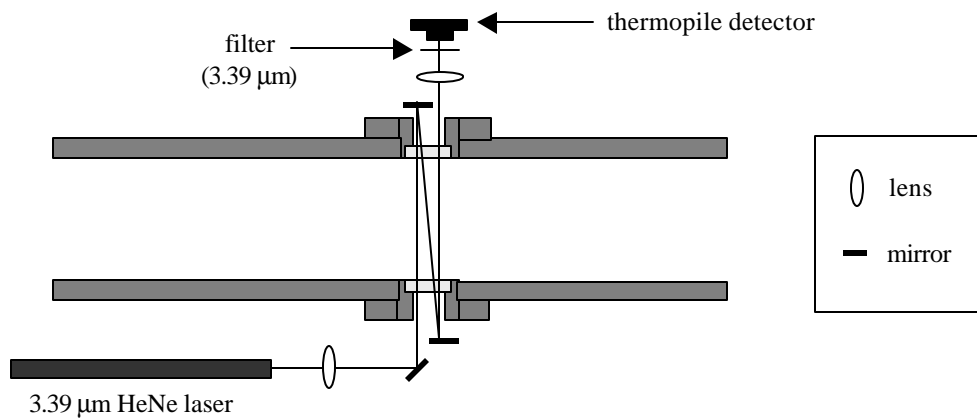
Fig. 3.6 IR absorption diagnostic utilized to measure the fuel concentration in-situ.

3.2.2 Gas Chromatography

To further validate the test mixture preparation method presented here and more confidently assess the uncertainty of the test mixture composition, a series of *n*-heptane mixtures were prepared in the high-pressure shock tube (HPST) laboratory. The HPST facilities included an SRI Instruments gas chromatograph (Model # 8610C) and accompanying data reduction software. The gas chromatograph (GC) was connected to the HPST via an isolation valve, thereby enabling the fuel concentration to be directly measured in the shock tube (see Fig. 3.7) by opening the isolation valve as the HPST was filled with the test mixture. The separation column utilized was a non-polar Supelcoport supported column with a 10% methyl silicon phase coating (SP-2100) with an 80/100 mesh size. The separation column was constructed of stainless steel, with a length of 12 inches and an outer and inner diameter of 0.125 and 0.085 inches, respectively. The GC was maintained at a constant oven temperature of nominally 46 °C, and the helium carrier gas flow rate was set to 25 mL/min for all measurements. The procedure employed to measure the *n*-heptane concentration of the test mixtures and the operation of the GC are described in the following paragraph.
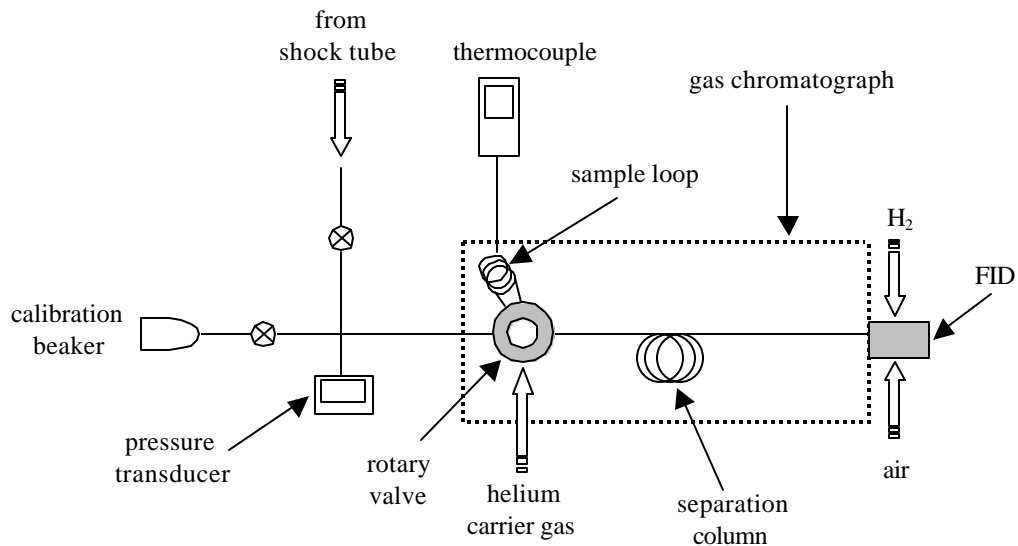
Fig. 3.7 Gas chromatograph.

Before each test, both the GC sample loop and shock tube were thoroughly evacuated. The shock tube was then filled with an *n*-heptane/O$_2$/Ar test mixture, and the isolation valve was opened to allow a small portion of the mixture to flow into the GC sample loop. The rotary valve was initially positioned such that the sample loop was isolated from the separation column. After the temperature and pressure of the test mixture in the sample loop was recorded, the rotary valve was actuated, which opened the sample loop to the helium carrier gas and the separation column. The carrier gas then pushed the test sample through the separation column, which separated the *n*-heptane from the oxygen and argon. Then fuel was then carried to the flame ionization detector (FID), which consisted of a hydrogen-air flame and a positively-charged collector electrode. As the fuel sample passed through the FID, the *n*-heptane was ignited by the hydrogen-air flame, thereby producing carbon ions. The collector electrode then detected the presence of these carbon ions, and the resulting FID signal was then transmitted to a data acquisition system, which recorded the duration and level of the signal (see Fig. 3.8). The data reduction software then calculated the time-integrated FID signal, which enabled the *n*-heptane mole fraction to be determined.
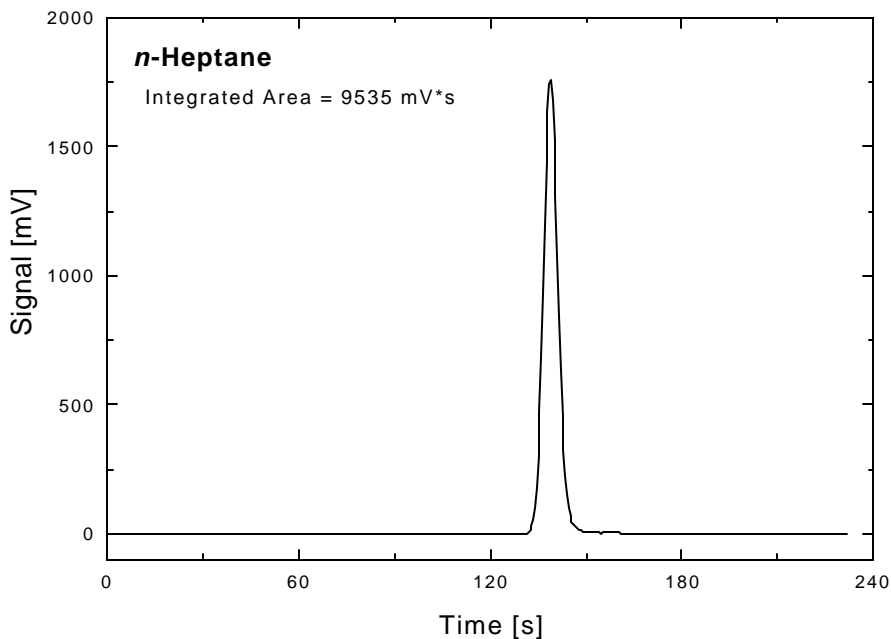
Fig. 3.8 Representative FID trace produced by the gas chromatograph.

Based on the integrated area of the FID signal, the number of moles of fuel in the sample loop may be inferred from a previously established calibration curve. The calibration curve for *n*-heptane was established using pure gaseous samples of the fuel, which were drawn into the sample loop directly from a calibration beaker containing the liquid fuel. A series of FID traces were obtained over a range of different *n*-heptane sample sizes to determine the responsiveness of the FID to various molar quantities (see Fig. 3.9). The number of moles of fuel was computed from the sample loop volume, pressure and temperature using the ideal gas equation of state. The calibration curve was found to vary from day-to-day due to slight differences in ambient conditions and the flow rates of the carrier and FID gases. Therefore, a calibration curve was established each day, just prior to conducting measurements with the GC.
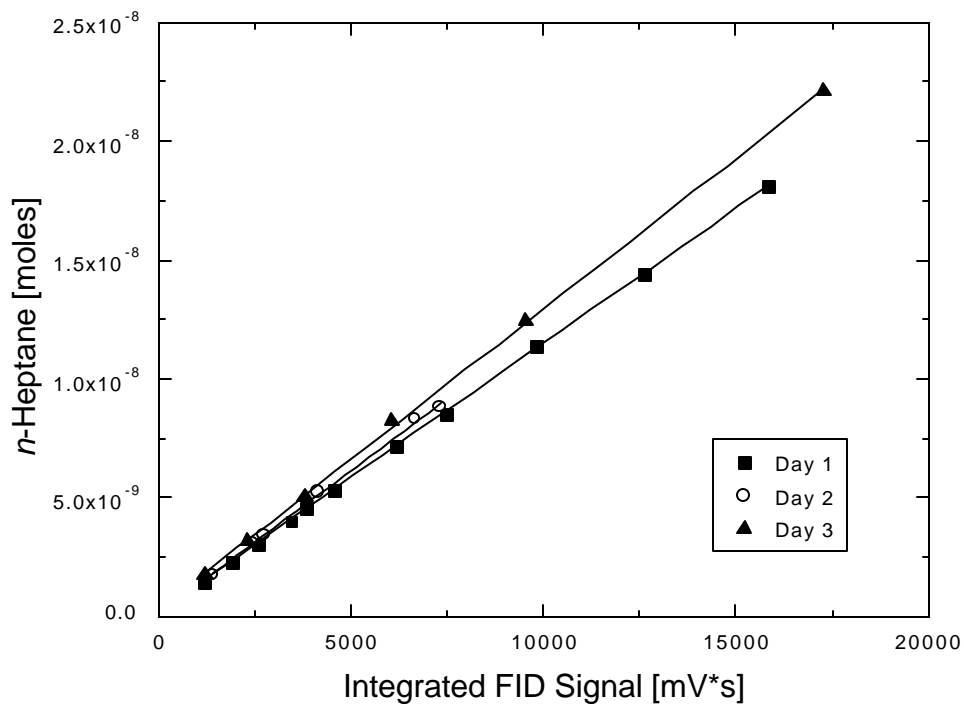
Fig. 3.9 Example gas chromatograph calibration curves.

The IR laser absorption diagnostic was also used to measure the in-situ fuel mole fraction in the HPST, thus enabling simultaneous measurements of the fuel concentration by both the gas chromatography and laser absorption. A direct comparison of the manometric, IR

26

absorption, and GC measurements is shown in Table 3.2 for a series of *n*-heptane/oxygen/argon test mixtures. The standard deviation of the fuel mole fraction was found to be nominally ±2.0% from the average of all three methods. In addition, the manometric and IR absorption measurements were found to agree within 5% for all liquid fuel test mixtures utilized in the LPST ignition time studies; GC measurements were not obtained for LPST work.

Table 3.2 Comparison of manometric, IR absorption, and gas chromatography fuel measurements.

Test mixture	Manometric [ppm]	IR absorption [ppm]	GC [ppm]	Average [ppm]	Standard deviation
1	996	1005	1043	1016	1.98%
	996	1014	1044		
2	4011	4162	3922	4025	2.21%
	4011	4116	3929		

3.3 SPECIES MEASUREMENT

A CH emission (431 nm) diagnostic was employed for all ignition time measurements to determine the onset of ignition. For a majority of these experiments, two CH diagnostics were utilized to simultaneously obtain ignition time measurements at both the shock tube sidewall and endwall locations. In addition, a lamp absorption diagnostic (174 nm) was used to record the time-history of ethylene for a series of *n*-alkane thermal decomposition experiments.

3.3.1 CH Emission Diagnostics

The emission of CH was simultaneously recorded at two locations for a majority of the ignition time work - 1) a sidewall location at a distance of 20 mm from the shock tube endwall, and 2) an endwall location, in which the emission of CH was monitored through a glass endplate (see Fig. 3.10). Initially, a second sidewall CH emission system was utilized to determine if the spatial resolution of the diagnostic had an effect on the measured ignition time (see Section 3.4.2). The sidewall CH emission collection systems consisted of a focusing lens ($f = 5$ cm), a fast (1.6 µs rise-time) silicon photodetector, and a narrow bandpass filter, centered at 431 nm with a spectral width of 10 nm. A slit was utilized to set the spatial resolution of the collection

volume, where the spatial resolution is defined as the maximum width of the collection volume within the shock tube. The endwall CH emission diagnostic simply consisted of a silicon photodetector and narrow bandpass filter, similar to the sidewall diagnostic. A slit was not necessary for the endwall measurements since the spatial resolution of this diagnostic was of no consequence to the measured ignition time (see Section 3.4.1). Furthermore, due to the wide field-of-view of the endwall detector, a focusing lens was not needed to achieve sufficient signal
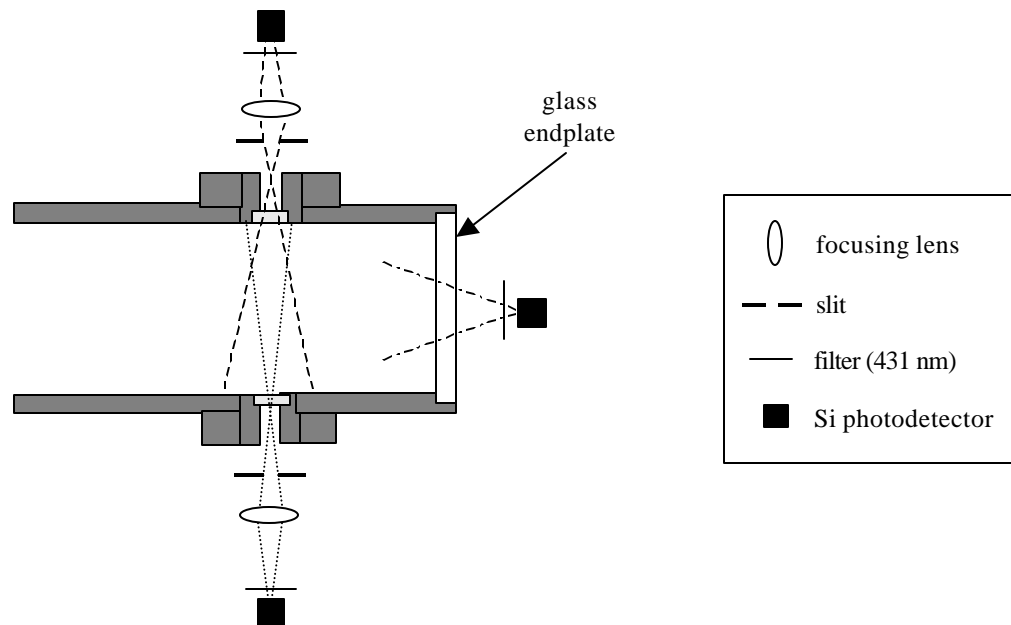
Fig. 3.10 Endwall and sidewall CH emission diagnostics.

3.3.2 Ethylene Absorption Diagnostic

The absorption of ethylene (C_2H_4) at 174 nm was achieved utilizing a microwave-lamp absorption diagnostic (Fig. 3.11). This system is an improved version of the ethylene diagnostic described previously by Zelson et al. [30], in which the earlier monochromator/PMT scheme is replaced by a fused-silica/Hamamatsu R1259 PMT. A mixture of 0.3% nitrogen, diluted in helium, was continuously pumped through a vacuum tube that was maintained at a pressure of approximately 6 torr. A microwave discharge was used to generate electronically excited N-

28

atoms, which produce a number of emission lines in the ultraviolet, including two strong lines at 174.27 and 174.53 nm. The PMT recorded the intensity of the lamp output, which passed through two 1.5 mm slits, located at each shock tube window, to set the spatial resolution of the diagnostic. The long wavelength limit of the ethylene diagnostic was restricted to under 200 nm by the spectral response of the PMT, and the short wavelength limit (approximately 165 nm) was achieved by placing a piece of fused silica directly in front of the PMT. Thus, essentially all the light detected by the PMT was from the two N-atom emission lines near 174 nm. The non-resonant signal for ethylene was found to be approximately 0.5% at both ambient and high temperature, and thus had a negligible effect on the measured ethylene trace. Power to the lamp was maintained at 30 W, with less than 1 W of reflected power.
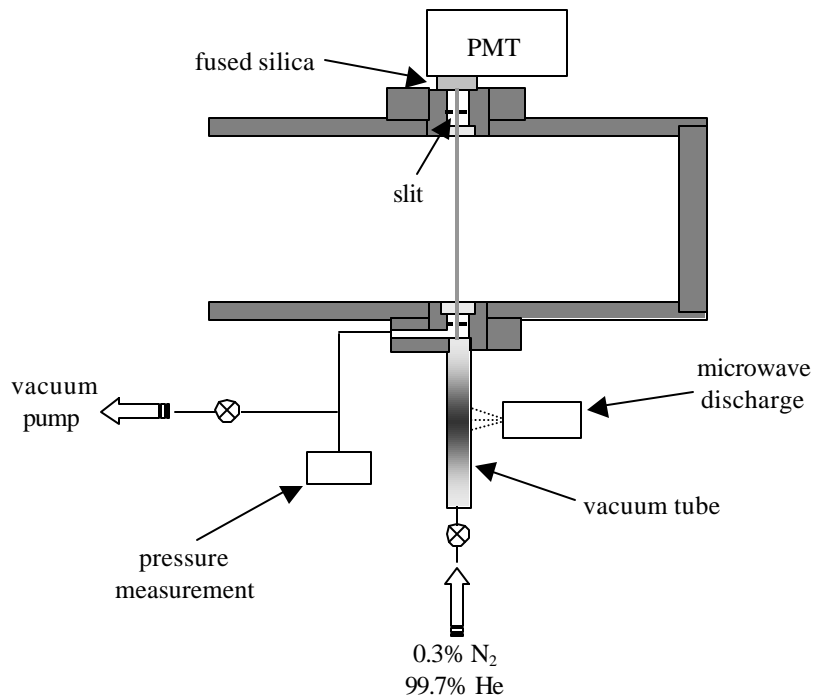
Fig. 3.11 Ethylene absorption (174 nm) diagnostic.

The high-temperature absorption coefficient of ethylene was measured from a series of experiments in which mixtures of ethylene, diluted in argon, were shock-heated and the resulting

absorption recorded. The ethylene absorption coefficient was then calculated from the measured absorption in both the incident and reflected regions based on the Lambert-Beer relationship. A representative ethylene trace is shown in Fig. 3.12.
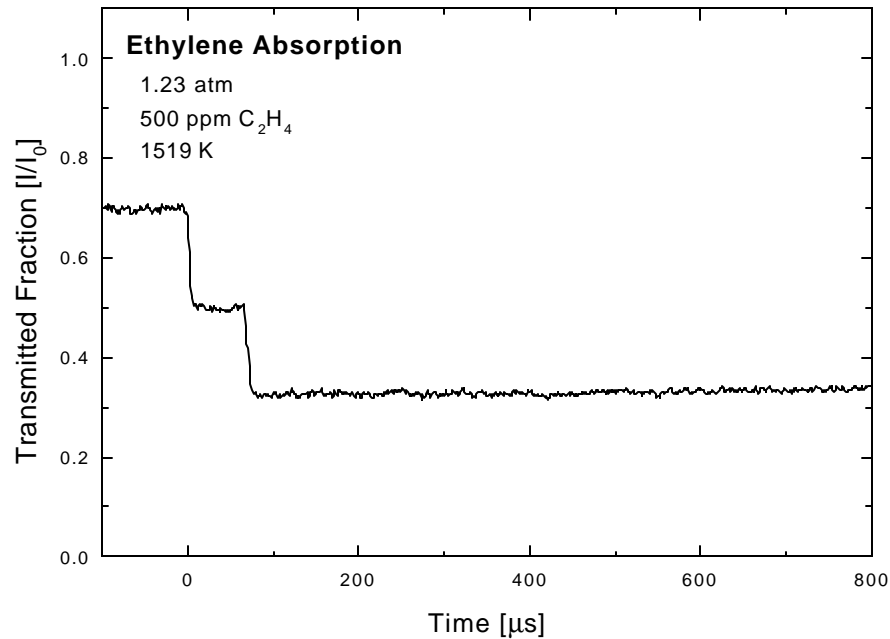
Fig. 3.12 Representative ethylene absorption trace.

In addition to ethylene, the lamp absorption diagnostic is also sensitive to hydrocarbons that contain double or triple carbon-carbon bonds, which similarly absorb near 174 nm. Therefore, the effect of potential interfering species must be considered when interpreting the ethylene absorption traces. For the high temperatures encountered in this study, large hydrocarbon species are very unstable, and will rapidly decompose into smaller species. Hence, the main interfering species for the current work were predicted to be acetylene (C_2H_2), propene (C_3H_6), and 1,3-butadiene (C_4H_6), and thus the high-temperature absorption coefficients of these species were also measured using the same procedure previously described for ethylene (see Fig. 3.13). From these measurements, and the results of detailed modeling, the measured absorption traces may be corrected to determine the time-history of ethylene.

Absorption Coefficients at 174 nm

Fig. 3.13 High-temperature absorption coefficients of select species at 174 nm.

3.4 IGNITION TIME DEFINITION

When using the reflected shock technique, the ignition time is defined as the time interval between the passing of the reflected shock wave and the onset of ignition. The arrival of the reflected shock may be accurately determined from a pressure trace, and the onset of ignition is usually inferred from an abrupt rise in pressure, or from the time-history of an intermediate combustion species, such as CH [23] or OH [24]. As discussed in Section 2.3.2, the ignition time should be measured at the shock tube endwall to obviate the potential errors associated with sidewall diagnostics. Therefore, all ignition time measurements for the current study were obtained at the shock tube endwall, using the endwall CH emission diagnostic previously described in Section 3.3.1. In addition, a sidewall CH emission collection system was also employed to determine the magnitude of the errors that may result when utilizing a sidewall diagnostic.

3.4.1 Endwall Ignition Time Definition

One method of directly measuring the ignition time at the shock tube endwall involves recording the pressure history at the endwall via a pressure transducer located in the shock tube endplate [20,25]. The ignition time at the endwall is then defined as the time interval between the arrival of the incident shock at the endwall, and the rapid rise in pressure at the time of ignition. However, as discussed in Section 2.3.2, this method may lead to uncertainties in the ignition time measurement when studying highly dilute mixtures. Therefore, a new method was developed for the current study to directly measure the ignition times of highly dilute test mixtures at the LPST endwall.

Endwall ignition time measurements were achieved utilizing a CH emission diagnostic, which viewed the test mixture through a glass endplate (see Fig. 3.10). In comparison to the pressure trace, the endwall CH emission trace shows a much more distinct increase upon ignition (see Fig. 3.14), thereby enabling the endwall ignition time to be more precisely determined for highly dilute test mixtures. A similar endwall diagnostic has been employed in the previous shock tube work of Gutman et al. [31] to measure the emission of light from the reaction $CO + O \rightarrow CO_2 + h\nu$. In that study, it was determined that the initial rise of the emission signal is largely due to the increase in the reflected shock reaction zone that results from the movement of the reflected shock away the endwall. However, at longer times (i.e., t > 35 μs) it was determined that the exponential rise in the emission signal was due to the reaction of the test mixture at the endwall. These findings suggest that the onset of ignition, measured at the endwall, should be based on the exponential rise of the CH emission trace, and not the initial rise of this signal.

The endwall ignition time was defined as the time interval between the arrival of the incident shock at the endwall, and the time at which the endwall CH emission signal reached its maximum rate of increase (see Fig. 3.14). Although the emission of CH occurs over a relatively short time period (i.e., 20-40 μs), the endwall trace shows a much longer CH emission lifetime since the endwall diagnostic viewed the test gas over the entire length of the shock tube. An

32

endwall pressure transducer was not employed for the LPST work, and thus the arrival of the incident shock at the endwall was estimated for each test from the following relationship,

$$t_{end} = t_{side} + l/V_i \qquad \text{[Eq. 3.2]}$$

where t_{end} is the estimated time of shock arrival at the endwall, t_{side} is the time at which the incident shock arrives at the sidewall measurement location, l is the distance between the sidewall measurement location and the endwall (20 mm), and V_i is the incident shock velocity at the endwall.   The time of shock arrival at the sidewall was determined from a pressure transducer located at the same axial position as the sidewall CH diagnostic, and the incident shock velocity was calculated by extrapolating the shock velocity profile to the endwall. For the conditions of the current study, the arrival of the incident shock at the endwall was found to vary from approximately 25-30 μs after its arrival at the sidewall location. Based on the uncertainly of the incident shock measurement, the time of shock arrival at the endwall was estimated to within ±0.2 μs.
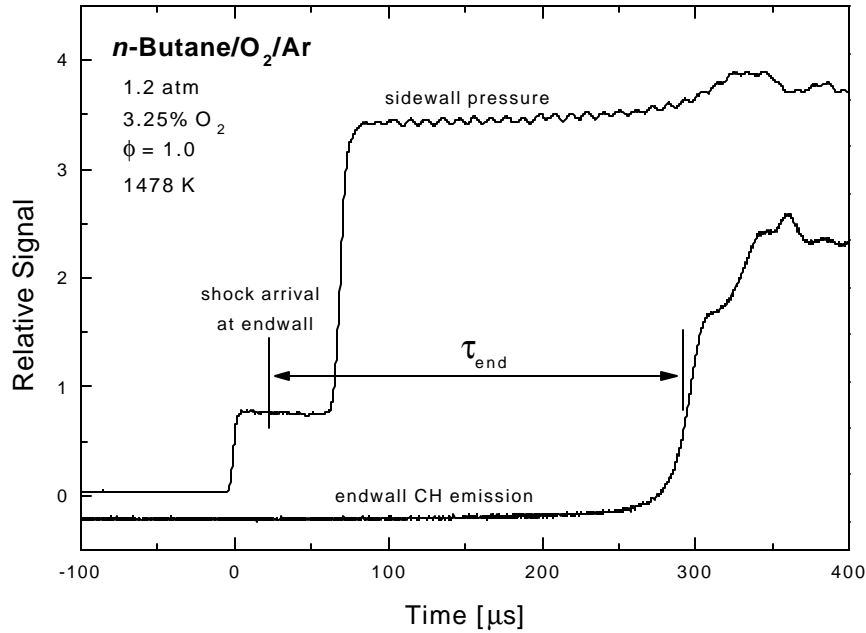
Fig. 3.14 Endwall ignition time definition.

3.4.2 Sidewall Ignition Time Definition

In addition to the endwall measurements, sidewall ignition time measurements were obtained at 20 mm from the shock tube endwall for a majority of the experiments. The sidewall ignition time was inferred from a CH emission diagnostic, as described previously in Section 3.3.1. Initially, a series of ignition time experiments were conducted using two sidewall CH emission diagnostics, each having a different spatial resolution, that were positioned at the same axial distance from the shock tube endwall (see Fig. 3.11). The purpose of these tests was to determine if the spatial resolution of the CH emission diagnostic had an effect on the measured ignition time at the sidewall.
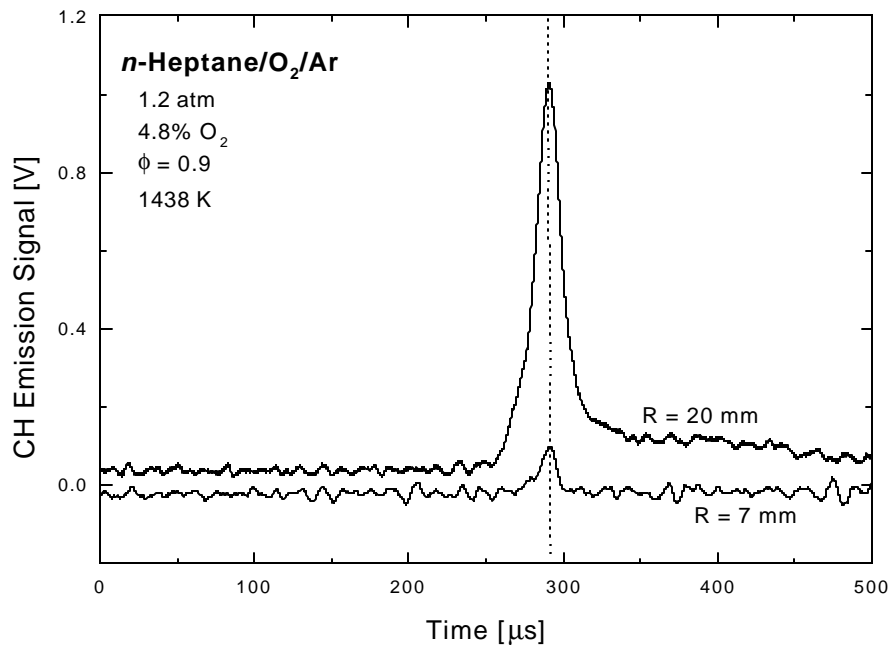
Fig. 3.15 Comparison of high- and low-resolution sidewall CH emission traces.

A comparison of the CH emission traces produced by two sidewall diagnostics, with varying spatial resolutions, is shown in Fig. 3.15. Due to its larger collection volume, the low-resolution diagnostic (R = 20 mm) is shown to produce a CH emission trace that is much broader than the high-resolution collection system (R = 7 mm). Therefore, f the sidewall ignition time were to be based on the initial rise of the CH emission trace, the spatial resolution

34

of the collection system will have a direct effect on the measured value for the ignition time. That is, measurements from a low-resolution (i.e., larger spatial resolution) collection system will yield a shorter ignition time than a corresponding high-solution collection system due to its wider field-of-view. However, the maximum signal recorded by both the low- and high-resolution CH emission diagnostics occurs at essentially the same time. This suggests that if the onset of ignition at the sidewall is defined as the time of maximum CH emission, the measured ignition time will be the essentially same for both diagnostics. Thus, all sidewall ignition times reported herein are defined as the time interval between the arrival of the reflected shock at the sidewall and the maximum of the CH emission trace, as shown in Fig. 3.16.
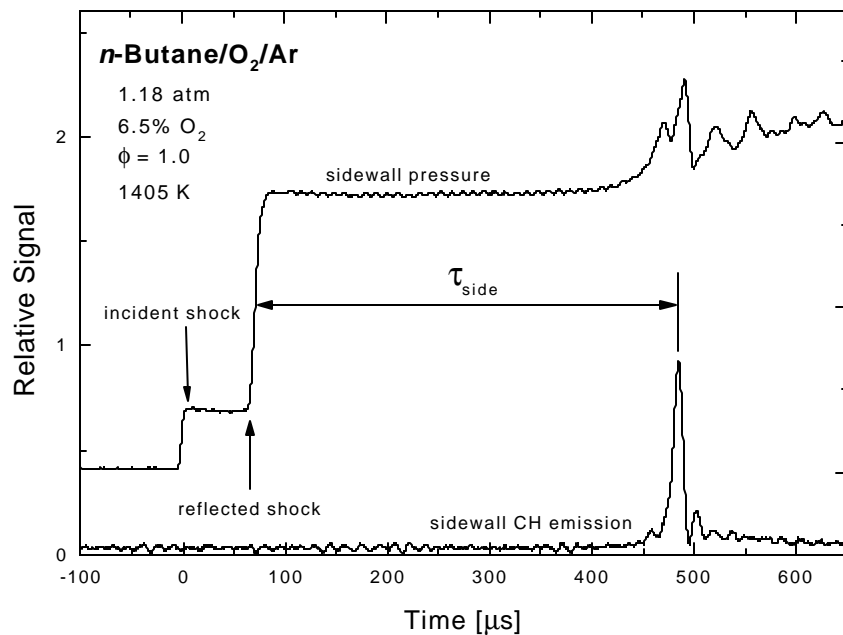
Fig. 3.16 Sidewall ignition time definition.

3.4.3 Comparison of Sidewall and Endwall Measurements

To more precisely determine the effect of energy release on the ignition time, sidewall and endwall measurements were simultaneously recorded using the CH emission diagnostics described earlier. A comparison of these measurements revealed that the measured values of the ignition time obtained at the shock tube sidewall were consistently shorter than those

35

measured at the endwall. This trend is consistent with the results found in previous shock tube experiments [20,25], however this effect was not observed in an earlier shock tube study by Seery and Bowman [32]. Schlieren photographs of the ignition process have shown that at the high temperatures of the current study, the ignition of a test mixture originates at the shock tube endwall, and the resulting combustion wave may "catch up" to the reflected shock wave [22,33]. Therefore, as combustion wave moves away from the endwall, its separation from the reflected shock may decrease, resulting in a shorter time lag between the reflected shock and combustion wave as they move away from the endwall.

The effect of the relative velocity between the reflected shock wave and the combustion wave on sidewall ignition time measurements has also been described previously via the illustration shown in Fig. 3.17 [25]. From this figure it is clear that the difference between the sidewall and endwall ignition time measurements ($\mathbf{\mathit{Dt}}$) will increase as the velocity of the combustion wave (V_c) increases relative to that of the reflected shock (V_r), or as the position of the sidewall measurement location moves further from the endwall.
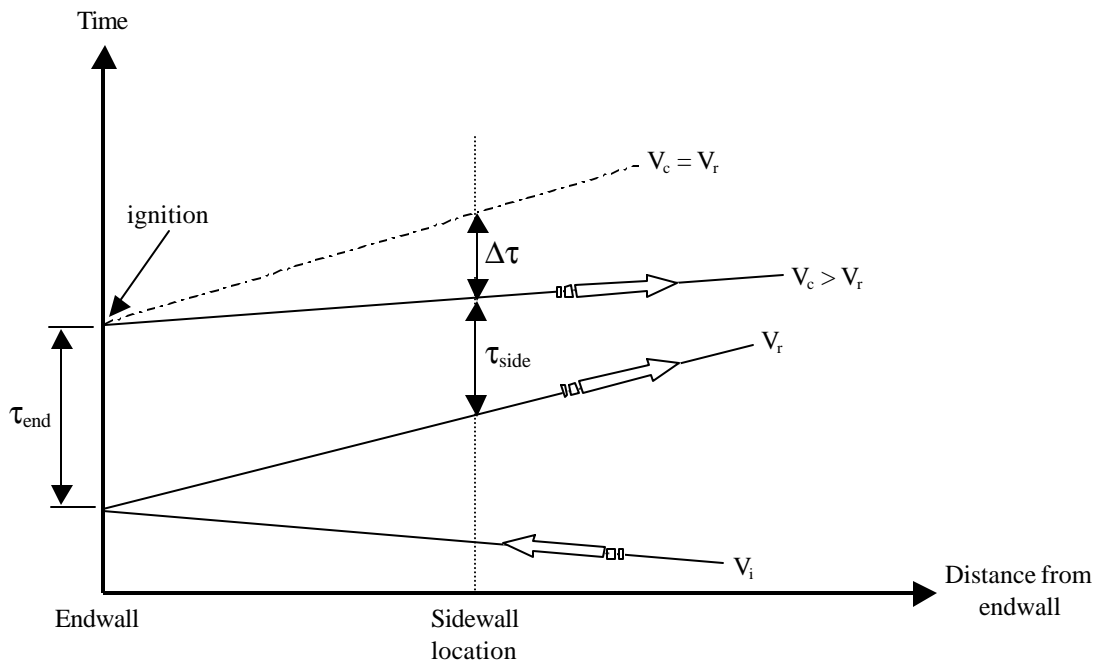
Fig. 3.17 x-t diagram of ignition process.

Representative measurements of the differences between the sidewall and endwall ignition times (Δt) are shown in Fig. 3.18 for a few stoichiometric n-heptane ignition mixtures. The data reveal that even when the sidewall measurement location is quite close to the endwall (i.e., 20 mm for this study), sidewall diagnostics may still be susceptible to significant measurement errors. In addition, the data show the measurement differences between the sidewall and endwall ignition time values increase with increasing temperature and/or increasing mixture strength. This is due to the higher combustion wave velocity that results under conditions for which the rate and magnitude of the energy release are high [33].
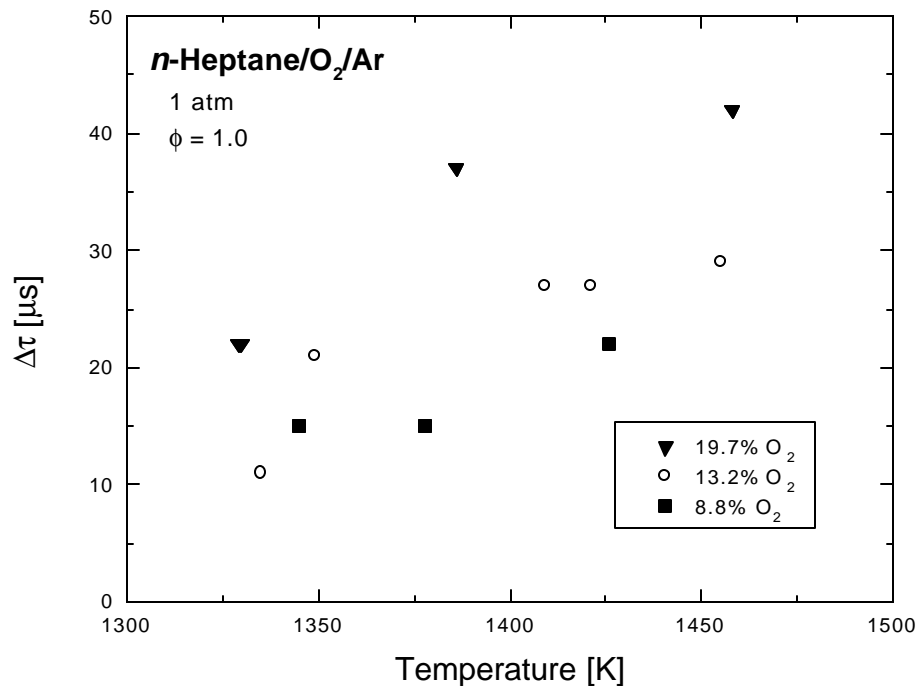
Fig. 3.18 Measured differences between sidewall and endwall ignition times.

Differences between the sidewall and endwall measurements were found to be much more significant at higher temperatures, for which Δt becomes large relative to the ignition time. As shown in Fig. 3.19, at the lowest temperatures Δt is only a few percent of the overall ignition time, but increases to over 20% at the highest temperatures. This trend leads to an overprediction of the ignition time temperature dependence, similar to the result observed in the

previous shock tube study by Burcat et al. [20]. Specifically, for the current study, the ignition time activation energy of *n*-heptane was measured as 48.1 kcal/mol based on the endwall measurements, while the sidewall measurements yielded activation energies of 55.4 kcal/mol and 60.5 kcal/mol for the 13.2% and 19.7% O_2 mixtures, respectively. Again, as shown in Fig. 3.19, it is evident that the measurements errors of the sidewall are more problematic for mixtures that are more energetic (i.e., higher fuel and oxygen concentration relative to that of the diluent).
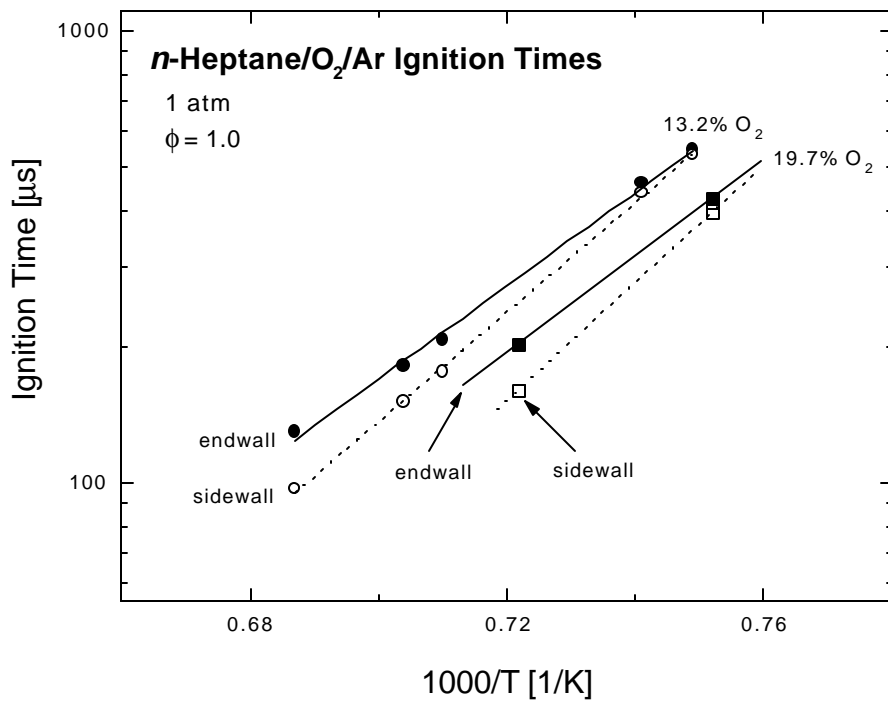
Fig. 3.19 Comparison of sidewall and endwall ignition time measurements.

Chapter 4

Ignition Time Measurements

This chapter contains the results of ignition time measurements for the fuels propane, *n*-butane, *n*-heptane, *n*-decane, and ethylene. Measurements were obtained over the temperature range of 1250-1750 K and pressure range of 1-6 atm. The test mixture composition varied from approximately 2-20% O_2, with an equivalence ratio of 0.5 to 2.0. In the initial phase of this study, ignition time behavior of *n*-butane and *n*-heptane was analyzed to assess the relative similarities and differences between these two representative *n*-alkanes. This analysis included the development of ignition time correlations for both fuels in order to directly compare the ignition time sensitivities of these fuels to a variety of parameters (e.g., fuel concentration, pressure). Based on the striking similarity between the ignition time sensitivities of *n*-butane and *n*-heptane, additional measurements were obtained for both a lower and higher order *n*-alkane - propane and *n*-decane. Furthermore, since ethylene is predicted to be a major decomposition product of many larger hydrocarbons, ignition time measurements for ethylene are presented to discern if the ignition time behavior this fuel is comparable to that of the *n*-alkanes studied in this work.

4.1 PARAMETRIC STUDY OF *n*-BUTANE AND *n*-HEPTANE IGNITION

Comparison of the ignition time behavior of *n*-butane and *n*-heptane are shown in Fig. 4.1 to 4.6. The effect of pressure on the ignition delay of *n*-butane and *n*-heptane is shown in Fig. 4.1 and 4.2, respectively, for which both fuels are shown to exhibit a systematic decrease in ignition time with increasing pressure. Furthermore, the ignition time pressure sensitivity is essentially constant over the range of pressures studied; that is, doubling the pressure from 1 to 2 atm has approximately the same effect on the ignition delay as doubling the pressure from 2 to

4 atm when the ignition time is plotted on a logarithmic scale. This suggests a functional relationship between the ignition time and pressure of the following forms,

$$\log \boldsymbol{t} \sim n \cdot P \qquad \text{[Eq. 4.1a]}$$

$$\boldsymbol{t} \sim P^{n} \qquad \text{[Eq. 4.1b]}$$

where the constant n is defined as the ignition time pressure sensitivity, which may be determined from a regression of the experimental data.

When air is utilized as an oxidizer, the relative proportions of the fuel, oxygen, and diluent (nitrogen) are uniquely defined by simply specifying the stoichiometry of the mixture since the oxygen-diluent ratio is fixed at nominally 1 to 4. However, for mixtures in which the oxygen-diluent ratio may be uniquely prescribed, as in the current study, it is necessary to specify two independent parameters to completely define the test mixture. That is, for a given stoichiometry (i.e., fuel-air ratio), the amount of fuel and oxygen relative to the diluent may varied, which in this study is termed the mixture strength. Hence, the mixture strength is effectively a measure of the dilution of the test mixture, and is quantified by the oxygen mole fraction (X_{O_2}).

The effect of mixture strength on the ignition delay of n-butane and n-heptane is shown in Fig. 4.3 and 4.4, respectively. Similar to the trend observed for an increase in pressure, an increase in mixture strength is shown to have an accelerating effect of the ignition delay of both fuels. Furthermore, the sensitivity of the ignition time to the mixture strength appears to be essentially constant for both fuels over the range of mixtures strengths studied, and thus is expected to follow the same functional relationship as shown in Eq. 4.1a and 4.1b for the pressure sensitivity.
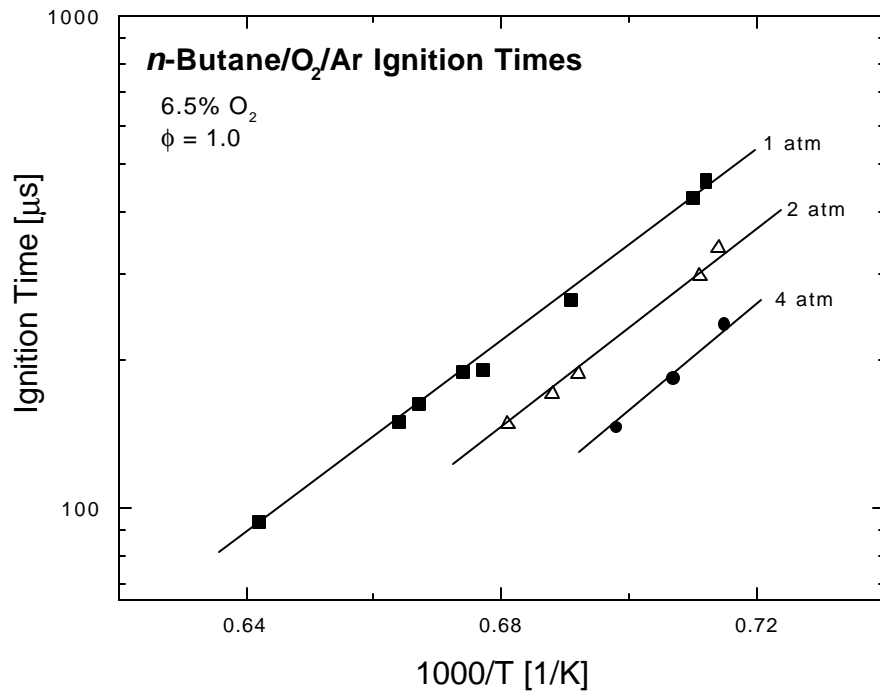
Fig. 4.1 Effect of pressure on ignition delay of *n*-butane.
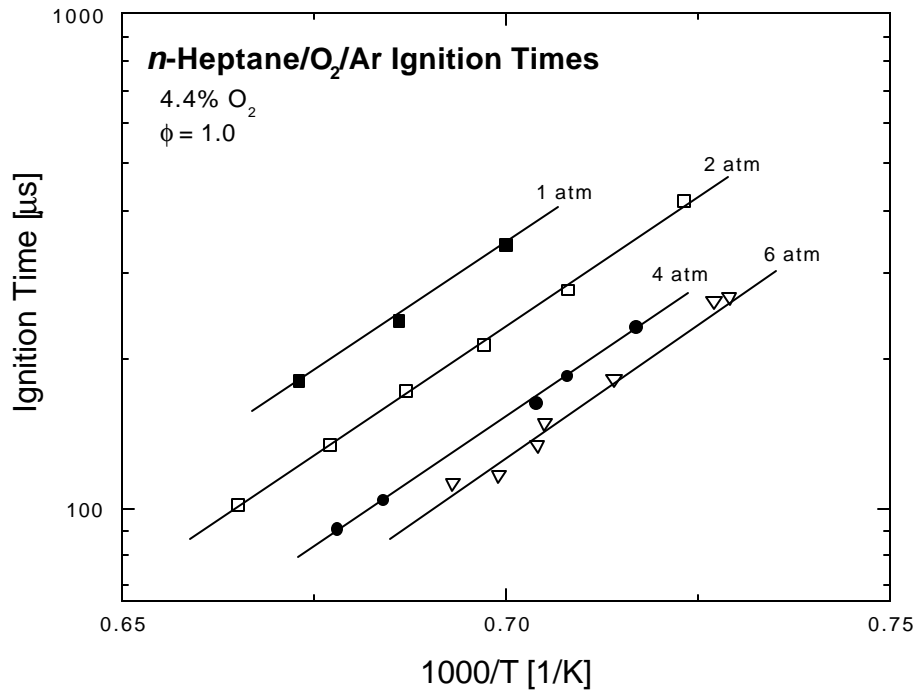
Fig. 4.2 Effect of pressure on ignition delay of *n*-heptane.
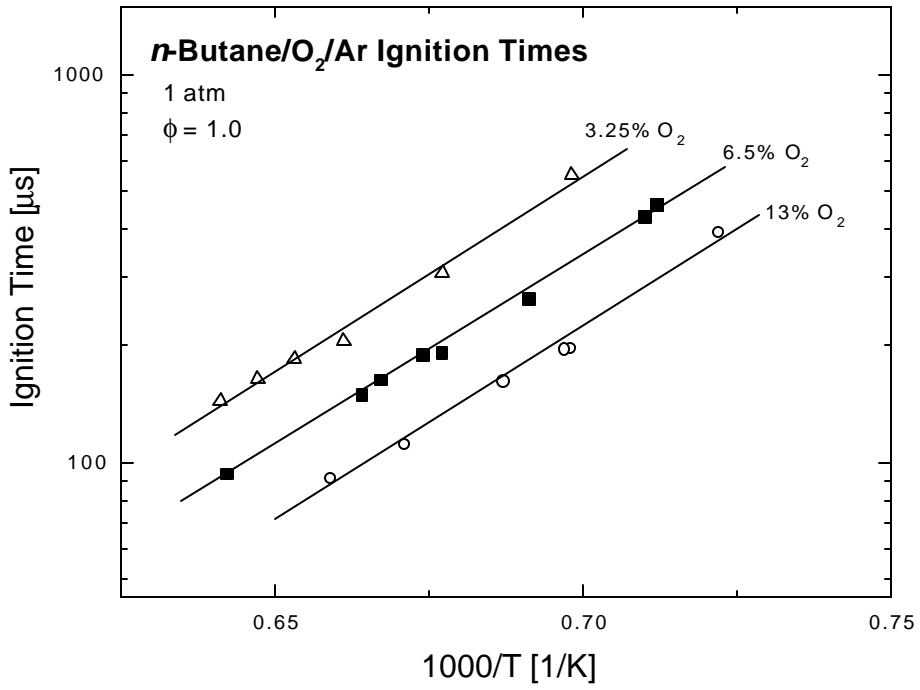
Fig. 4.3 Effect of mixture strength on ignition delay of *n*-butane.
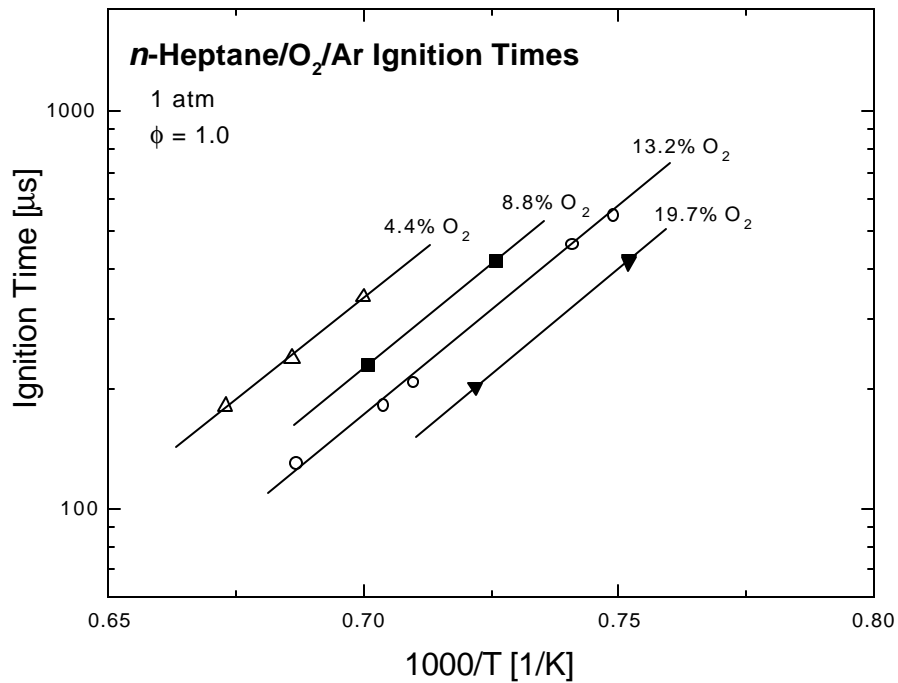
Fig. 4.4 Effect of mixture strength on ignition delay of *n*-heptane.
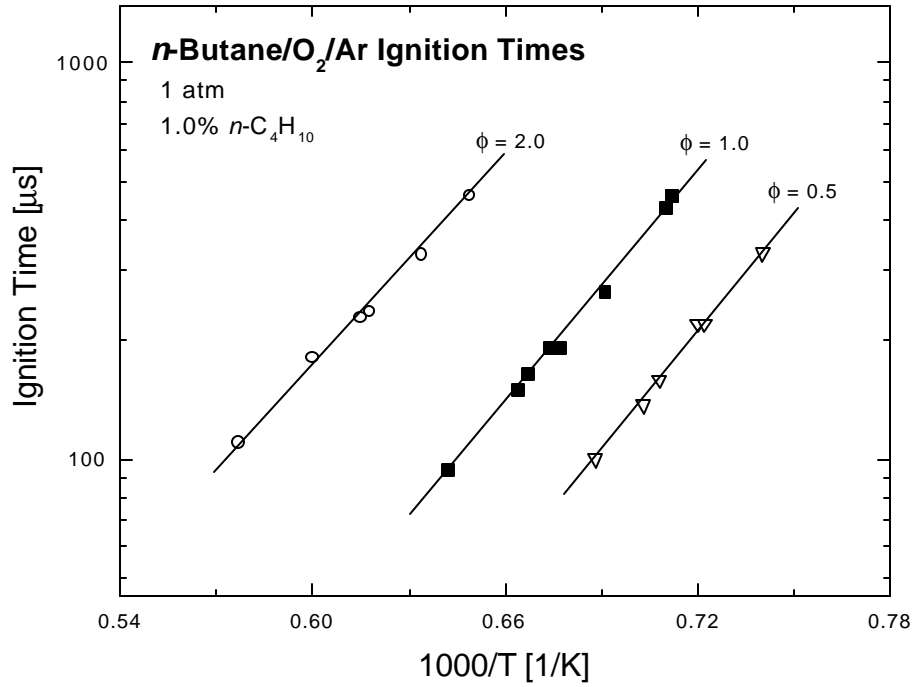
Fig. 4.5 Effect of stoichiometry on ignition delay of *n*-butane.
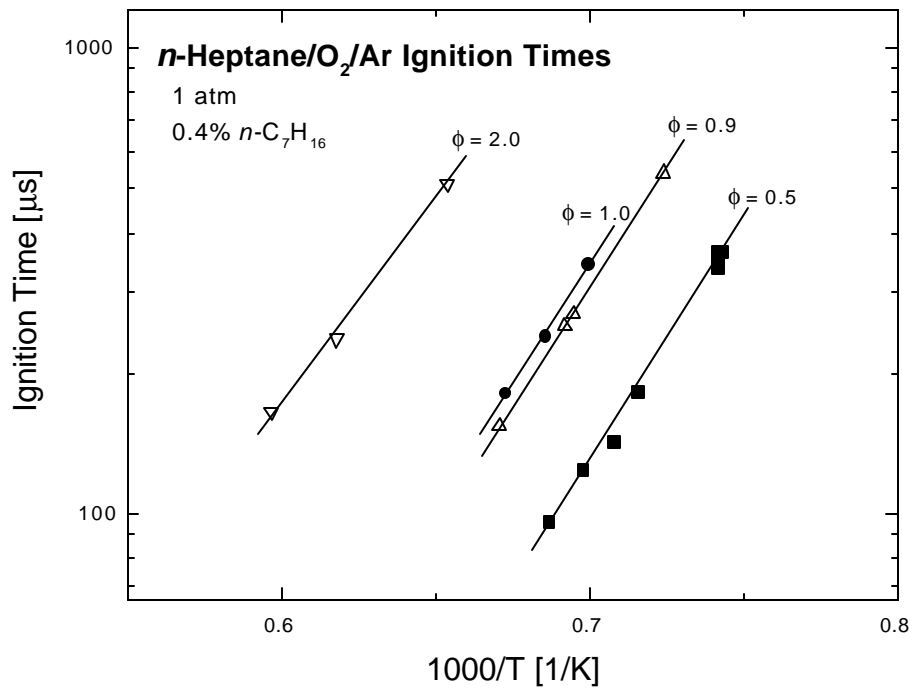
Fig. 4.6 Effect of stoichiometry ignition delay of *n*-heptane.

The effect of equivalence ratio on the ignition delay of *n*-butane and *n*-heptane is shown in Fig. 4.5 and 4.6, respectively. The results are presented at a fixed fuel mole fraction, however, the trend of increasing ignition time with increasing equivalence ratio shown above is similarly observed when the data are presented at either a fixed oxygen or argon mole fraction. Unlike the effect of pressure and mixture strength, the ignition time sensitivity to the equivalence ratio is shown to increase as the mixture becomes more fuel rich. That is, increasing the equivalence ratio by a factor of 2 has a larger effect on the ignition time than decreasing the equivalence ratio by this same factor. Therefore, the ignition time sensitivity to the equivalence ratio is not accurately described by the same logarithmic relationship as suggested by the pressure and mixture strength sensitivities (i.e., Eq. 4.1a and 4.1b).

4.1.2 *n*-Butane and *n*-Heptane Ignition Time Correlations

As discussed in Chapter 2, ignition time correlations provide a useful means of assessing the sensitivity of the ignition delay to the relevant parameters and comparing results to past works. Therefore, a regression analysis of the current ignition time data has been performed to develop ignition time correlations for *n*-butane and *n*-heptane. To assess the relative advantages of different correlation forms (see Section 2.2), the ignition time measurements of *n*-butane and *n*-heptane have been correlated using the following two forms,

$$\boldsymbol{t} = Z_1 \, [fuel]^{\,a} \, [O_2]^{\,b} \, e^{\,E/RT} \qquad\qquad \text{[Eq. 4.2a]}$$

$$\boldsymbol{t} = Z_2 \, P^{\,n} \, X_{O_2}^{\,x} \, \boldsymbol{f}^{\,k} \, e^{\,E/RT} \qquad\qquad \text{[Eq. 4.2b]}$$

The correlation form presented in Eq. 4.2a, which has been employed most frequently in past studies, expresses the ignition time as a function of the fuel and oxygen concentrations and the post-shock temperature. The correlation form shown in Eq. 4.2b, which is suggested by the current study, expresses the ignition time in terms of the total pressure (*P*), the mixture

equivalence (f) ratio and oxygen mole fraction (X_{O_2}), and the reflected shock temperature. A regression analysis of the current ignition time measurements for n-butane and n-heptane yielded the following correlations,

n-Butane: $t = 7.63 \times 10^{-8} \; [n\text{-}C_4H_{10}]^{0.99} \; [O_2]^{-1.61} \; e^{42,850/RT}$ [Eq. 4.3a]

($\phi = 0.5\text{-}2.0$) $t = 3.57 \times 10^{-5} \; P^{-0.64} \; X_{O_2}^{-0.62} \; f^{1.00} \; e^{41,000/RT}$ [Eq. 4.3b]

n-Heptane: $t = 4.54 \times 10^{-8} \; [n\text{-}C_7H_{16}]^{0.95} \; [O_2]^{-1.58} \; e^{45,000/RT}$ [Eq. 4.4a]

($\phi = 0.5\text{-}2.0$) $t = 6.67 \times 10^{-6} \; P^{-0.61} \; X_{O_2}^{-0.68} \; f^{0.96} \; e^{44,600/RT}$ [Eq. 4.4b]

where the ignition time is in microseconds, concentrations are in mol/cm^3, pressure is in atmospheres, X_{O_2} is the oxygen mole fraction, and the ignition time activation energy (E) is in units of cal/mol. As suggested by the data presented in Figs. 4.1 to 4.6, there are marked similarities between the ignition time sensitivities of n-butane and n-heptane. Both fuels exhibit a fuel and oxygen concentration sensitivity of nominally 1.0 and -1.6, respectively, a pressure and mixture strength (X_{O_2}) sensitivity of approximately -0.65, and an equivalence ratio sensitivity near 1.0.

In addition to the similarities between the two fuels, it is also apparent that the ignition time sensitivities of each fuel are consistent between the two correlation forms. Both correlation forms are shown to yield essentially the same ignition time activation energy, even though these two expressions account for the temperature sensitivity in slightly different ways. The correlation form presented in Eq. 4.2a includes a temperature dependent term via the fuel and oxygen concentration terms in addition to the exponential term, while correlation form of Eq. 4.2b accounts for the temperature sensitivity in only the exponential term.

Also, both correlation forms result in essentially the same value for the ignition time pressure sensitivity. Although the correlation form of Eq. 4.2a does not explicitly state the

pressure sensitivity, its value may be inferred from the sum of the concentration sensitivities $(a+b)$. The *n*-butane pressure sensitivities given by the correlation forms of Eq. 4.2a and Eq. 4.2b are shown to be -0.62 and -0.64, respectively, and -0.63 and -0.61, respectively, for *n*-heptane.

To assess the accuracy of each correlation form in representing the experimental data, the ignition time measurements of each fuel were normalized by their respective correlation parameters and expressed as a function of reciprocal temperature. The resulting R^2-value of a best-fit line through the normalized data may then be used to quantify the accuracy of each correlation. The normalized *n*-butane ignition time data for both correlation forms presented here are shown in Figs. 4.7 and 4.8. Although not shown, the normalized *n*-heptane data exhibit the same general trends shown for *n*-butane.

As shown in Figs. 4.7 and 4.8, both correlation forms result in essentially the same R^2-value, which suggests that the accuracy of both correlation forms is very similar. Furthermore, both correlation forms are shown to have difficulty in correlating both the lean and rich ignition time data. This observation is a direct result of the trends observed in Figs. 4.5 and 4.6 above, for which it was shown that the ignition time sensitivity to the equivalence ratio does not follow a simple logarithmic relationship. Therefore, the correlation forms presented here are most appropriate when correlating ignition time data that is within a relatively narrow range of equivalence ratios.

Although the correlation form of Eq. 4.2a does not explicitly express the ignition time as a function of the equivalence ratio, it is possible to determine the functional relationship between the ignition time and the equivalence ratio suggested by this correlation form. This may be accomplished by substituting the quantity *[XᵢP/RT]* for both the fuel and oxygen concentration terms, where X_i is the mole fraction of either the oxygen or fuel, *R* is simply the universal gas constant, and *P* and *T* are the pressure and temperature of the test mixture, respectively. From this substitution, it is possible to rearrange the correlation of Eq. 4.2a into the following form,
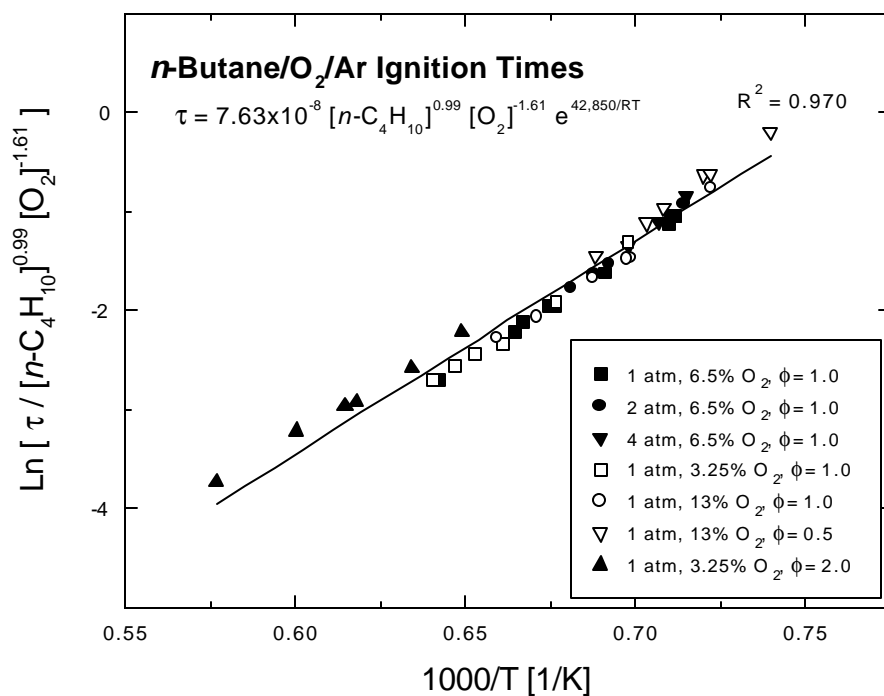
Fig. 4.7 Correlated *n*-butane ignition time measurements using correlation form of Eq. 4.2a.
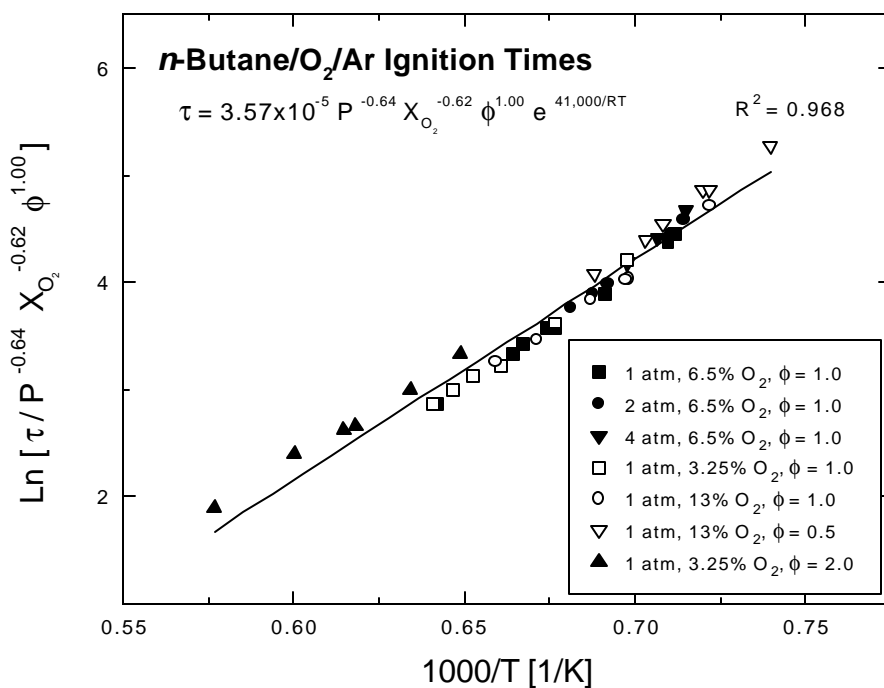
Fig. 4.8 Correlated *n*-butane ignition time measurements using correlation form of Eq. 4.2b.

$$\boldsymbol{t} \sim (RT)^{-(a+b)} \, P^{\,a+b} \, X_{O_2}^{\,a+b} \, \boldsymbol{f}^{\,a} \, e^{\,E/RT} \qquad\qquad \text{[Eq. 4.5]}$$

where the ignition time pressure, mixture strength, and equivalence ratio sensitivities are now explicitly stated. From this expression, it is evident that both correlation forms effectively assume the same logarithmic relationship for the ignition time equivalence ratio sensitivity. Therefore, it is understandable why both correlation forms have difficulty in accurately correlating both the lean and rich ignition time measurements.

To more precisely correlate the ignition time data, a regression analysis was performed using only the stoichiometric data of each fuel. Only the correlation form of Eq. 4.2b was utilized in this analysis since the fuel and oxygen concentrations cannot be independently varied for a fixed equivalence ratio, and therefore their individual sensitivities could not be calculated. A regression analysis of the stoichiometric ignition time data yielded the following expressions,

n-Butane ($\phi = 1.0$): $\quad \boldsymbol{t} = 5.09 \times 10^{-6} \, P^{-0.55} \, X_{O_2}^{-0.66} \, e^{\,46,000/RT} \qquad$ [Eq. 4.6]

n-Heptane ($\phi = 1.0$): $\quad \boldsymbol{t} = 1.86 \times 10^{-6} \, P^{-0.54} \, X_{O_2}^{-0.67} \, e^{\,48,100/RT} \qquad$ [Eq. 4.7]

where the ignition time is in microseconds, pressure is in atmospheres, X_{O_2} is the oxygen mole fraction, and the ignition time activation energy (E) is in cal/mol.

Using the expression presented in Eq. 4.6, the stoichiometric *n*-butane ignition time data have been normalized using the same method described above. The normalized stoichiometric ignition time data for *n*-butane is shown in Fig. 4.9. The resulting R^2-value is shown to improve from 0.968 to 0.995 when only the stoichiometric data is considered. A similar improvement was obtained for the *n*-heptane ignition time measurements, in which the R^2-value increased from 0.978 to 0.996 when only the stoichiometric data was correlated.
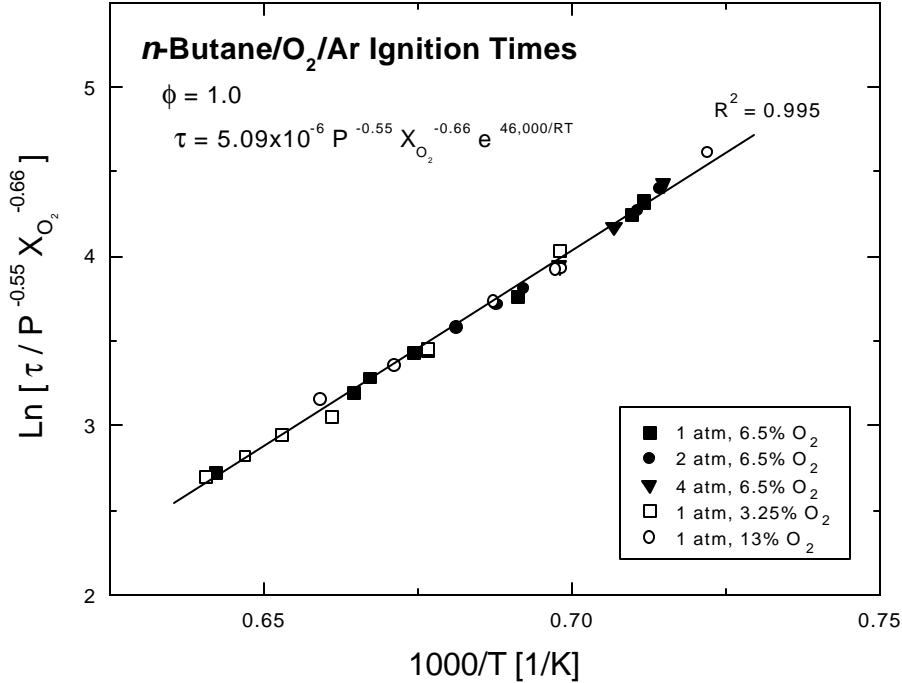
Fig. 4.9 Correlated stoichiometric *n*-butane ignition time measurements.

Although the *n*-butane and *n*-heptane correlations presented in Eq. 4.6 and 4.7 have been developed for only stoichiometric mixtures, an analysis of the current work and past studies (see Chapter 5) suggest that the ignition time temperature, pressure and mixture strength sensitivities (E, n, x) presented for the stoichiometric data similarly apply under both lean and rich conditions. Therefore, ignition time correlations for non-stoichiometric mixtures may be derived by from the correlations of Eq. 4.6 and 4.7 by simply modifying the scaling constant Z in each expression to account for the absolute change in ignition time due to the change in equivalence ratio.

For example, based on the results of the current study, the ignition time correlations of both *n*-butane and *n*-heptane may be modified to the $\phi = 0.5$ condition by decreasing the scaling constant in the correlations of Eq. 4.6 and 4.7 by a factor of 2.6, and to the $\phi = 2.0$ condition by increasing the scaling constant by a factor of 5.0. A summary of these

modifications is presented in Table 4.1. The correlations that result from these adjustments to the scaling constants of Eq. 4.6 and 4.7 are recommended over the correlations presented in Eq. 4.3 and 4.4 since, as discussed previously, ignition time correlations are most accurate when presented for a single equivalence ratio.

Table 4.1 Scaling constants for *n*-butane and *n*-heptane ignition time correlations.

n-butane		*n*-heptane	
ϕ	Scaling constant $Z (\times 10^6)$	ϕ	Scaling constant $Z (\times 10^6)$
0.5	1.96	0.5	0.72
1.0	5.09	1.0	1.86
2.0	25.5	2.0	9.30

4.2 COMPARISON OF IGNITION DELAYS AMONG *n*-ALKANES

In order to quantitatively compare the ignition times of *n*-butane and *n*-heptane, all the stoichiometric data for both fuels were scaled to the condition of 1 atm and 20% O_2 by the following relation,

$$\boldsymbol{t}_{1 \, atm, \, 20\% \, O_2} = \boldsymbol{t}_{initial} \, (1 \, / \, P_i)^{n_i} (0.20 \, / \, X_{O_2, \, i})^{x_i} \qquad \text{[Eq. 4.8]}$$

where $\boldsymbol{t}_{initial}$ is the value of the original ignition time measurement, and n_i and x_i are the ignition time sensitivities determined for the stoichiometric *n*-butane and *n*-heptane data. While the chosen condition at which the data are compared is arbitrary, a comparison at any other mixture strength or pressure will produce essentially the same relative trend between the two fuels since the pressure and mixture strength sensitivities of *n*-butane and *n*-heptane have been shown to be almost identical.

To similarly compare a lower and higher order *n*-alkane to the *n*-butane and *n*-heptane measurements, a series of propane and *n*-decane ignition time data were also obtained. The

relatively high vapor pressure of propane at ambient conditions (approx. 130 psia) enabled stoichiometric mixtures at 20% O_2 to be directly studied in the LPST, obviating the need to scale the propane ignition time data. However, due to the very low room temperature vapor pressure of *n*-decane (approx. 1 torr), the maximum achievable mixture strength at stoichiometric conditions was limited to approximately 3% O_2, and therefore it was necessary to scale the *n*-decane data to the 20% O_2 condition. Since the *n*-decane mixture strength sensitivity could not be measured over a higher range of mixtures strengths, the *n*-decane ignition time data were scaled to the 20% O_2 condition using the average mixture strength sensitivities calculated from the stoichiometric *n*-butane and *n*-heptane data. Based on the similarity of the *n*-butane (x = -0.66) and *n*-heptane (x = -0.67) mixture strength sensitivities, this method of scaling the *n*-decane ignition time data is believed to be appropriate.

When the stoichiometric ignition time data of all four *n*-alkanes: propane, *n*-butane, *n*-heptane, and *n*-decane, are compared at the 1 atm and 20% O_2 condition, the ignition time is seen to increase with decreasing molecular size of the fuel in a systematic way (see Fig. 4.10). A similar result was also shown in a previous study by Burcat et al. [34], in which the ignition times of propane, *n*-butane and *n*-pentane were compared at roughly the same oxygen mole fraction. One possible explanation for this trend in ignition time with respect to *n*-alkane molecular size is as follows.

At a given equivalence ratio, the oxygen requirement of a fuel increases with the number of carbon and hydrogen atoms contained in the fuel. For example, the stoichiometric oxygen to fuel ratio for the *n*-alkanes increases from 5 for propane to 15.5 *n*-decane. Furthermore, it has been suggested that prior to ignition, there is a competition between the fuel and molecular oxygen for H-atoms [35], as shown by the following two reactions,

$$H + O_2 \rightarrow O + OH \qquad\qquad [R\ 4.1]$$

$$H + RH \rightarrow R + H_2 \qquad\qquad [R\ 4.2]$$
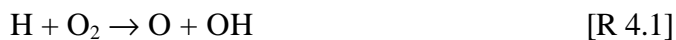
where "RH" is used to denote the fuel, and "R" is the resulting fuel radical after an H-atom has been abstracted. Reaction R 4.1 is a highly effective chain-branching reaction that accelerates the formation of free radicals, while reaction R 4.2 essentially results in the termination of H-atoms and the formation of a less reactive fuel radical. Therefore, as the amount of oxygen relative to the fuel increases, as occurs for an increase in size of an n-alkane, the ignition delay time of a mixture may decrease due to the increased production of H-atoms by reaction R 4.1 relative to reaction R 4.2. This reasoning may also explain the decrease in ignition delay with decreasing stoichiometry shown for both n-butane and n-heptane (see Figs. 4.5 and 4.6).
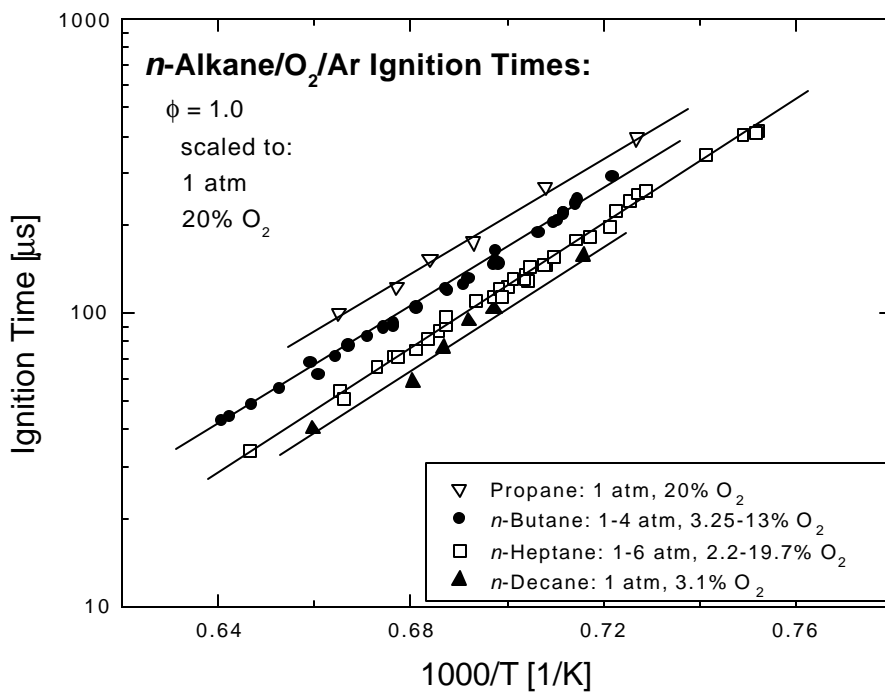
Fig. 4.10 Comparison of stoichiometric n-alkane ignition time measurements.

4.2.2 n-Alkane Ignition Time Correlation

Based on the similarities between the ignition time sensitivities for n-butane and n-heptane, and the systematic decrease in ignition time with increasing n-alkane size, a regression analysis was performed on the stoichiometric measurements for all four n-alkanes to derive a single ignition time correlation for these fuels. This required the use of an additional parameter

to account for the effect of fuel size on the ignition time. The parameter selected was the number of carbon atoms (C) in the molecule. A regression analysis of all the stoichiometric ignition time data for all four n-alkanes yielded the following expression,

$$n\text{-Alkanes } (\phi = 1.0): \quad \boldsymbol{t} = 9.40 \times 10^{-6} \, P^{-0.55} \, X_{O_2}^{-0.63} \, C^{-0.50} \, e^{46,550/RT} \qquad \text{[Eq. 4.9]}$$

where the ignition time is in microseconds, pressure is in atmospheres, X_{O_2} is the oxygen mole fraction, and the ignition time activation energy (E) is in units of cal/mol. All of the ignition time data utilized to formulate this correlation are shown in Fig. 4.11, for which the best-fit line of the data has an R^2-value of 0.992.
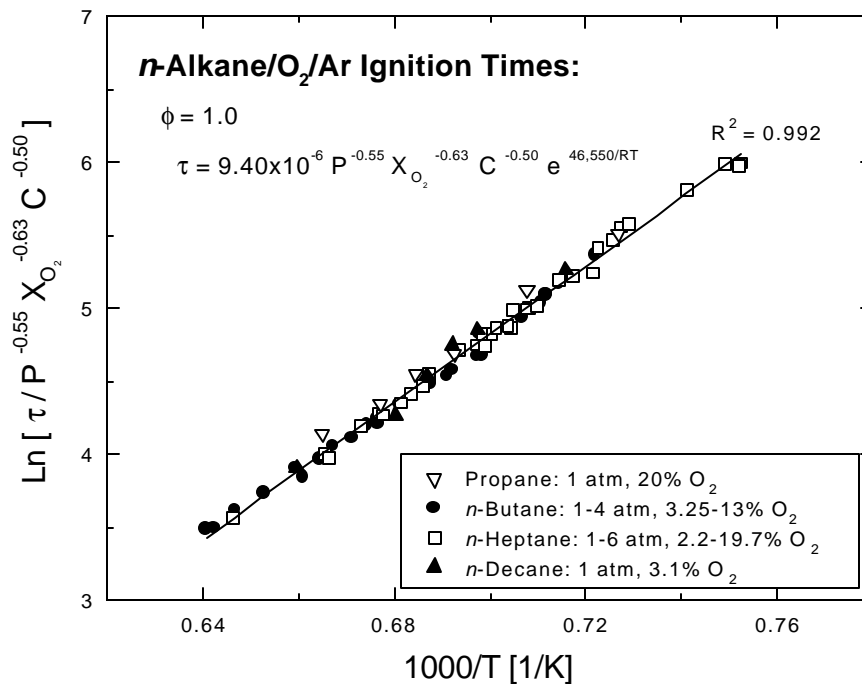
Fig. 4.11 Correlated stoichiometric n-alkane ignition time measurements.

At the temperatures of the current study, the larger n-alkanes (i.e., propane and above) are predicted to rapidly decompose into smaller hydrocarbons fragments (i.e., C_1 and C_2 species) from the rupture of their C-C bonds, and by H-atom abstraction (see Fig. 4.12).

However, the subsequent decomposition of these smaller fuel fragments is predicted to be rate-limiting, thereby accounting for similarities in the observed combustion characteristics among the larger *n*-alkanes [36]. A more detailed discussion of chemical pathways by which the *n*-alkanes are predicted to decompose is presented in Chapters 7 and 8.

<div align="center">

_n_-alkane **_n_-alkane**

+M +H, O, OH

alkyl radical, alkene, H alkyl radical

smaller alkyl radicals,
alkenes, H, CH$_3$

CH$_4$, CH$_3$, C$_2$H$_4$, etc.

</div>

Fig. 4.12 High-temperature oxidation scheme for the *n*-alkanes.

4.3 PARAMETRIC STUDY OF ETHYLENE IGNITION

Both the current study (see Chapter 7) and previous works [37] have found ethylene to play an important role in the combustion of *n*-alkanes. Therefore, a parametric study of ethylene ignition was conducted to ascertain if the ignition time behavior of ethylene is similar to that of the *n*-alkanes. The effect of pressure on the ignition time of ethylene is shown in Fig. 4.13. Although the ignition time of ethylene is shown to decrease with increasing pressure, similar to the trend observed for *n*-butane and *n*-heptane, the ignition time temperature dependence of ethylene clearly shows a regular increase with increasing pressure. The ignition time activation energy for ethylene increases from 21,000 cal/mol at 1 atm, to 36,700 cal/mol at

4 atm. This increase in activation energy with increasing pressure for ethylene ignition is also predicted by detailed chemical modeling, which is discussed in Section 6.3.
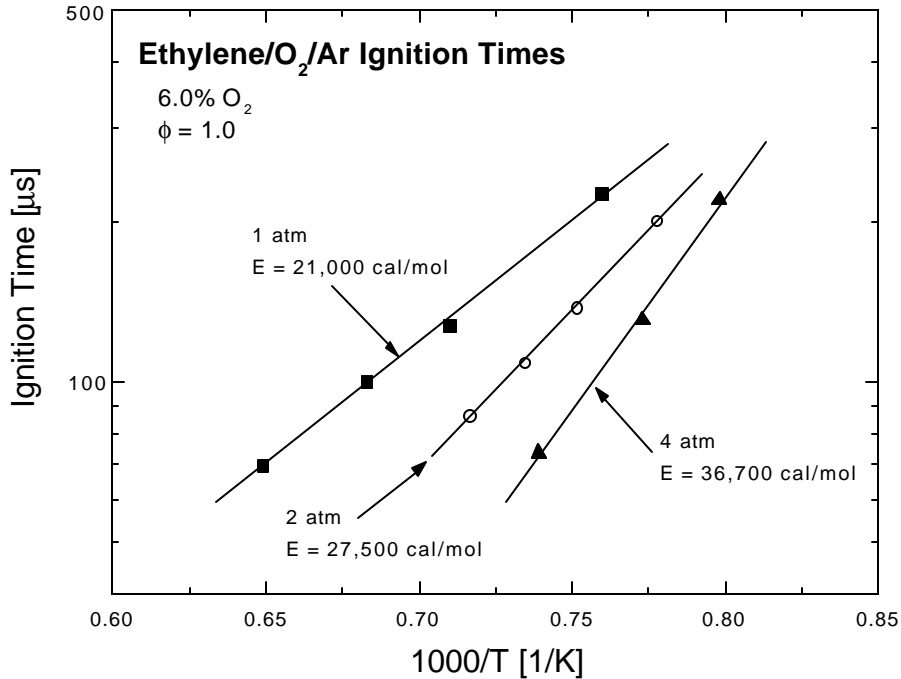
Fig. 4.13 Effect of pressure on the ignition delay of ethylene.

The effect of mixture strength on the ignition delay of ethylene is shown in Fig. 4.14 at a pressure of 1 and 2 atm. Similar to the *n*-alkanes, the ignition delay of ethylene is shown to decrease with increasing mixture strength. Furthermore, the ignition time temperature sensitivity of ethylene does not appear to be a function of the mixture strength, and thus it is possible to determine the mixture strength sensitivity of ethylene at each specific pressure. Over the range of 3.0%-12% O_2, the mixture strength sensitivity of ethylene was found to increase from -0.95 at 1 atm, to -1.1 at 2 atm. Thus, it appears the ignition time sensitivity of ethylene to both temperature and mixture strength are coupled to the pressure, which is in stark contrast to the autoignition behavior exhibited by both *n*-butane and *n*-heptane. Based on these results, it is evident that the ignition time behavior ethylene is quite dissimilar from that of the *n*-alkanes.
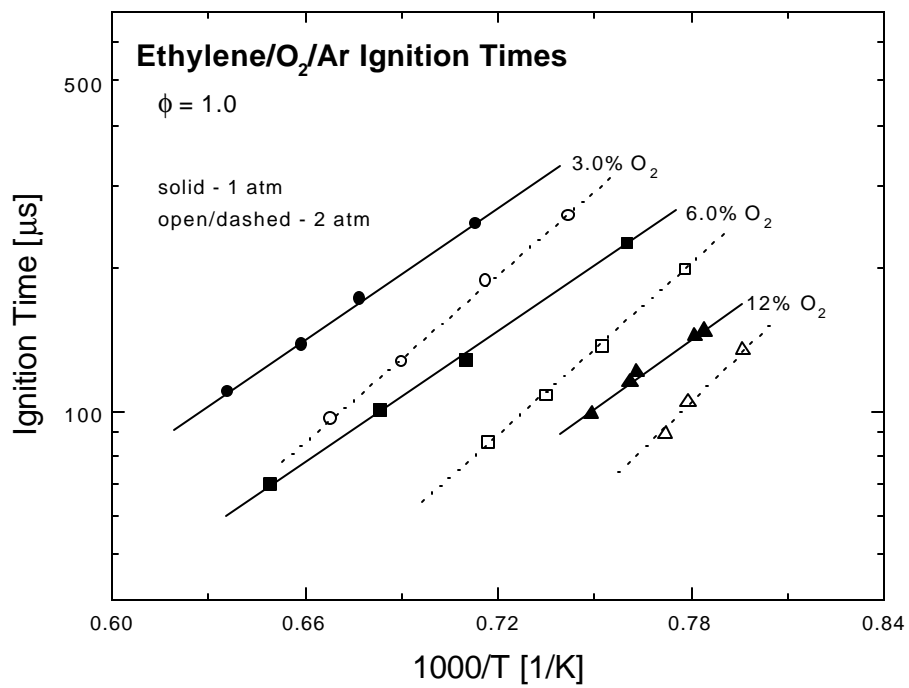
Fig. 4.14 Effect of mixture strength on the ignition delay of ethylene ignition at 1 and 2 atm.

Chapter 5

Comparison to Past Ignition Time Studies

To quantitatively compare the current ignition time measurements to previous studies, and to further validate the correlations presented herein over a wider range of conditions, the ignition time sensitivities determined in this study were utilized to scale the ignition time measurements of the current study and previous works to a prescribed condition. Comparisons are presented for the ignition time measurement of propane, *n*-butane, *n*-heptane, and *n*-decane. Due to the difficulty in accurately scaling ignition time data with respect to equivalence ratio (see Section 4.1.2), only ignition time measurements that were obtained at the same equivalence ratio are compared. In addition, the current ethylene ignition time data is compared to previous studies. However, due to the complex ignition time behavior exhibited by ethylene, only studies conducted at similar conditions are compared.

5.1 METHOD OF COMPARISON

The ignition time data of the current study and past works have been scaled from the initial condition at which they were obtained (i), to a prescribed average condition (c) according to the following relation,

$$\boldsymbol{t}_c = \boldsymbol{t}_i \, (P_c / P_i)^n \, (X_{O_2,c} / X_{O_2,i})^x \qquad \text{[Eq. 5.1]}$$

where n and x are the empirical ignition time sensitivities measured in this study. The above equation does not include a correction for the stoichiometry of the mixtures since only data obtained at the same equivalence ratio are compared. Although the conditions at which ignition time data are compared have been chosen arbitrarily, scaling the data to any other condition

57

(i.e., pressure or oxygen mole fraction) would yield the same qualitative trends. That is, once all the ignition time measurements have been scaled to a common condition (c_1), scaling this data to any other condition (c_2) would simply require multiplying all measurements by a scaling constant S.

$$S = (P_{c_2} / P_{c_1})^n (X_{O_2, c_2} / X_{O_2, c_1})^x \qquad \text{[Eq. 5.2]}$$

Therefore, a comparison of the ignition time data at any other condition would simply shift the absolute value of the ignition times, and not their relative values.

5.2 PREVIOUS *N*-ALKANE STUDIES

5.2.1 Propane

The propane ignition time data of the current study have been compared to the shock tube measurements previously obtained by Brown and Thomas [33], Burcat et al. [34,38], Gray and Westbrook [39], and Qin et al. [40]. In the study by Burcat et al., ignition times were measured in the reflected shock region, and the onset of ignition was defined as the time of the initial rise in either a pressure and/or heat-flux trace, which were measured by a pressure transducer and thin platinum filament, respectively, located in the shock tube endwall. In the study by Gray and Westbrook, ignition time measurements were obtained in the incident shock region, and the onset of ignition was defined as the time of maximum CH emission, which was recorded by a sidewall emission diagnostic. In the study by Brown and Thomas, measurements were attained in the reflected shock region, and the onset of ignition was determined from the initial rapid rise in CH emission, which was recorded by a photomultiplier located at the shock tube endwall. In the study by Qin et al., ignition times were measured in the reflected shock region, and the onset of ignition was defined as the maximum rate of pressure rise as measured at the shock tube endwall.

Comparisons of the stoichiometric propane ignition time data for this study and three previous studies are presented in Fig. 5.1. Due to the wide range of conditions presented (1-14 atm, 1.0-20.8% O_2), the data are shown to vary by more than an order of magnitude, making it difficult to compare these studies. To enable a more direct comparison, all the data presented in Fig. 5.1 were scaled to 5 atm and 10% O_2 using the empirical n-alkane ignition time sensitivities calculated here (i.e., n = -0.55, x = -0.63). The scaled data are shown in Fig. 5.2. In the study by Brown and Thomas, the ignition delay was based on the initial rise in CH emission, whereas the maximum rate of increase in CH emission was employed here, which may explain, in part, the shorter delays measured by Brown and Thomas relative to this study. However, the ignition time data of this study and all other studies accurately collapse onto a single line when scaled by the empirical sensitivities measured here. This agreement further validates the empirical ignition time sensitivities, and suggests the feasibility of using this scaling method to compare ignition time measurements that are obtained at different conditions.

In the previous study by Burcat et al. [38], the following correlation was developed for the ignition delay of propane,

$$\boldsymbol{t} = 4.4 \times 10^{-8} \ [C_3H_8]^{0.57} \ [O_2]^{-1.22} \ e^{42,200/RT} \qquad \text{[Eq. 5.3]}$$

where the ignition time is in microseconds, concentrations are in mol/cm^3, and the activation energy (E) is in cal/mol. From this expression, it is evident that the ignition time activation energy measured by Burcat et al. (42,200 cal/mol) is in good agreement with the value measured here (45,100 cal/mol). Also, although the Burcat et al. correlation does not explicitly state the ignition time pressure and mixture strength sensitivity, both of these values may be obtained by algebraically reducing this correlation form to that presented in Eq. 4.5. When the correlation of Burcat et al. is rearranged in this fashion, the resulting pressure and mixture strength sensitivities are n = -0.65 and x = -0.65, which are very close to the values found in the current study for the n-alkane data (i.e., n = -0.55, x = -0.63).

Propane/O$_2$/Ar Ignition Times

ϕ = 1.0

1000
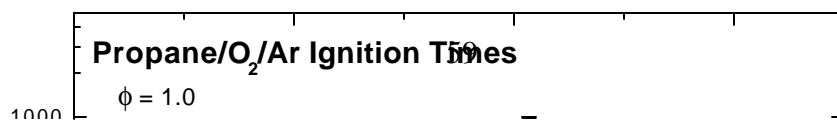
Fig. 5.1 Comparison of propane ignition time studies.
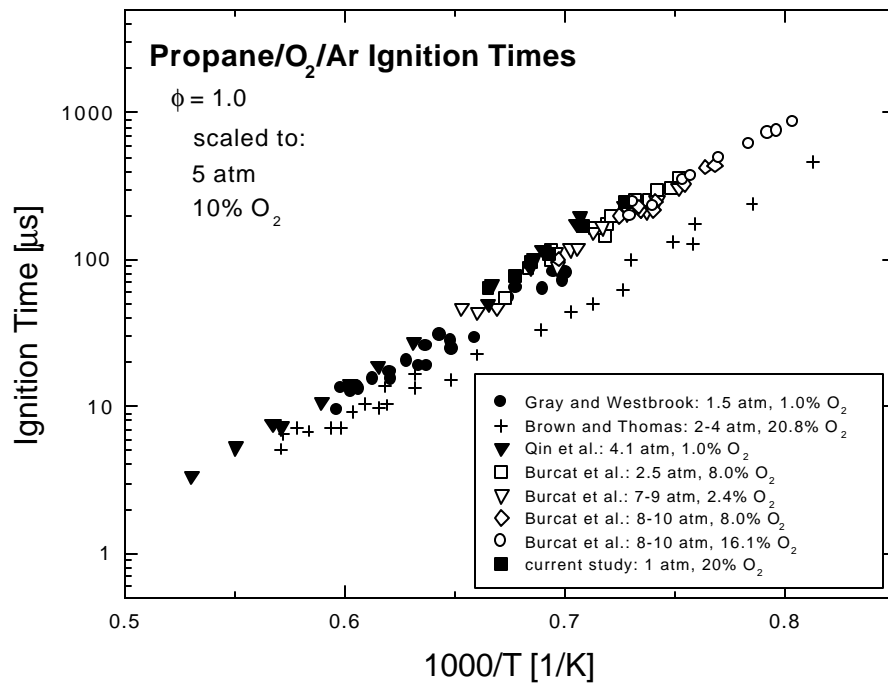
Fig. 5.2 Comparison of propane ignition time studies (scaled to 5 atm, 10% O$_2$).

5.2.2 *n*-Butane

The uncorrected *n*-butane ignition time measurements of this study have been compared to the previous shock tube study by Burcat et al. [34], as shown in Fig. 5.3. In the study by Burcat et al., ignition times of *n*-butane were measured in the reflected shock region, and the onset of ignition was defined as the time of the initial rise in either a pressure and/or heat-flux trace, which were measured by a pressure transducer and thin platinum filament, respectively, located in the shock tube endwall. Due to differences in the range of conditions studied, the current data is roughly a factor of 5-10 longer than the measurements by Burcat et al., making it difficult to directly compare the ignition time measurements of the two studies on a quantitative basis. In addition, an ignition time correlation for *n*-butane was not given in Burcat et al. study since only one test mixture was utilized in that study. Therefore, the ignition time sensitivities of *n*-butane for that study are not available for comparison to the current work.

To quantitatively compare the *n*-butane ignition time measurements, the data of Burcat et al. and the current study were scaled to the condition of 5 atm, 15% O_2 (Fig. 5.4) using the ignition time sensitivities for the stoichiometric *n*-butane data presented in Eq. 4.6. The scaled data of the current study and that previously obtained by Burcat et al. are shown to exhibit nominally the same ignition time temperature sensitivity, however, the absolute ignition time values reported by Burcat et al. are approximately 20% shorter than those measured in this study. This variance may be due, in part, to the different ignition time definitions employed in each study. That is, in the study by Burcat et al., the onset of ignition was defined as the initial rise in a pressure and/or heat-flux trace, whereas in the current study, this definition is based on the maximum rate of increase in the CH emission signal. Had the study by Burcat et al. employed an ignition time definition based on the maximum rate of increase in either the pressure or and/or heat-flux, instead of the initial rise, the measured ignition times would be somewhat longer, and thus in better agreement with the measurements obtained in this study.

n-Butane/O$_2$/Ar Ignition Times

$\phi = 1.0$

1000
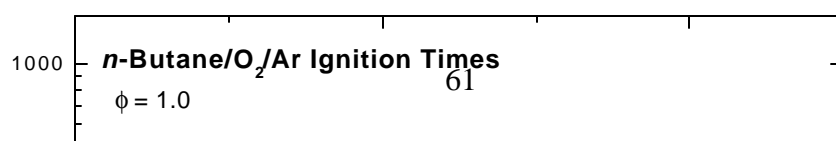
Fig. 5.3 Comparison of *n*-butane ignition time studies.
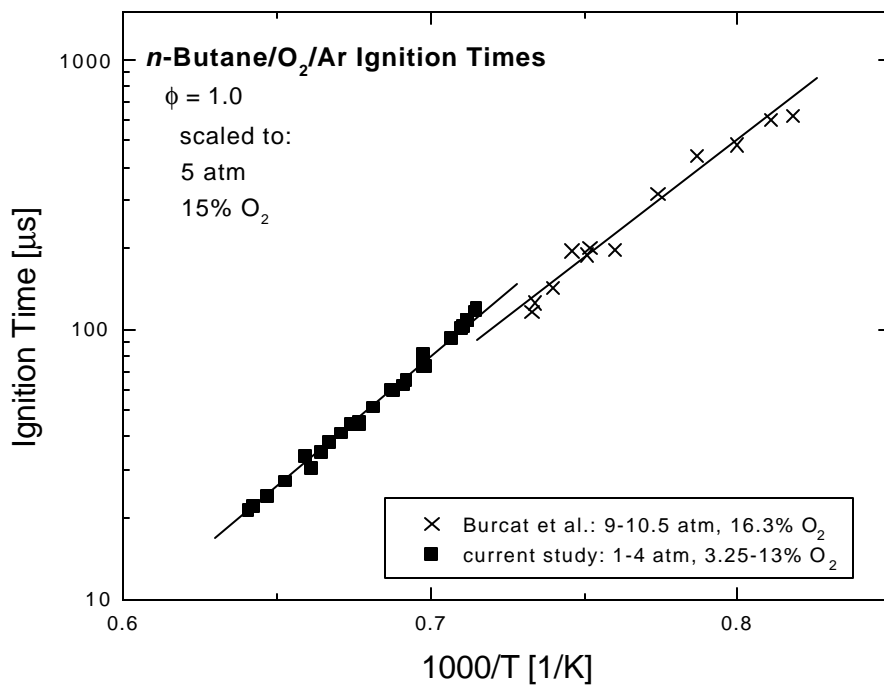
Fig. 5.4 Comparison of *n*-butane ignition time studies (scaled to 5 atm, 15% O$_2$).

5.2.3 *n*-Heptane

The *n*-heptane ignition time data of the current study are compared to the previous shock tube studies of Burcat et al. [20], Colket and Spadaccini [21], and Vermeer et al. [22]. Ignition time measurements for all three previous studies were obtained in the reflected shock region. In the study by Vermeer et al., the ignition time was measured solely from a pressure trace, and was confirmed at short ignition times (< 260 μs) by photographic records of the ignition process. The precise location of the pressure measurement was not specified. In the Colket and Spadaccini study, the onset of ignition was defined as the initial rise of an OH emission signal, which was measured 1.7 cm from the shock tube endwall. In the study by Burcat et al., the ignition time was based on pressure traces obtained by a pressure transducer located in the shock tube endplate. The stoichiometric data for all three previous studies are presented in Fig. 5.5, for which the conditions of the various studies are shown to differ significantly (i.e., 1-11 atm, 2.1-33.1% O_2). Due to the large number of data sets presented, the data of the current study are not included in this figure.

All the stoichiometric *n*-heptane ignition time measurements presented in Fig. 5.5 have been scaled to the condition of 5 atm, 10% O_2 (see Fig. 5.6) using the ignition time sensitivities of the stoichiometric *n*-heptane correlation presented in Eq. 4.7. For clarity, the ignition time measurements of this study are presented in terms of the correlation expression. In comparing the scaled ignition time data presented in Fig. 5.6, it is apparent that there is good agreement between the measurements of Vermeer et al. and those measured here over the entire temperature range studied.   Also, the data of Colket and Spadaccini exhibit a similar temperature sensitivity to that found in the current study and by Vermeer et al., although the absolute measurements of Colket are approximately 25% shorter.   As mentioned in the previous section, this variance may be due to the different ignition time definition employed. At the high temperature range, the ignition time measurements of Burcat et al. are in excellent agreement with data of Vermeer et al. and the current study, but exhibit a much lower temperature sensitivity than that measured by the other three studies.

***n*-Heptane/O$_2$/Ar Ignition Times**

$\phi = 1.0$

1000

Fig. 5.5 Comparison of stoichiometric *n*-heptane ignition time studies.

n-Heptane/O₂/Ar Ignition Times

φ = 1.0
scaled to:
5 atm
10% O₂

● Vermeer et al.: 1-4 atm, 27.5% O₂
▲ Colket and Spadaccini: 4-7 atm, 2.1% O₂
+ Burcat et al.: 2.7 atm, 11.0% O₂
□ Burcat et al.: 4.5 atm, 11.0% O₂
✕ Burcat et al.: 8-11 atm, 11.0% O₂
△ Burcat et al.: 3.7 atm, 33.1% O₂
— correlation of current study

Ignition Time [μs]

1000/T [1/K]
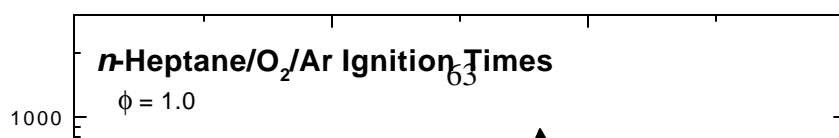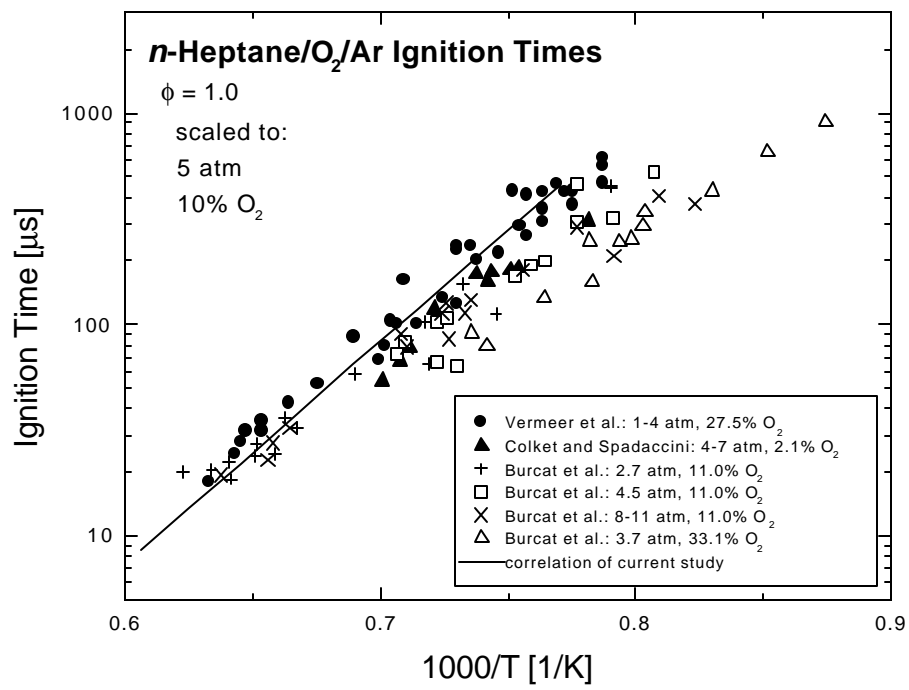
Fig. 5.6 Comparison of stoichiometric *n*-heptane ignition time studies (scaled to 5 atm, 10% O$_2$).

To further test and validate the ignition time sensitivities measured in the current study at conditions other than stoichiometric, both the lean ($\phi = 0.5$) ignition time measurements obtained by Burcat et al. and Colket and Spadaccini, and the rich ($\phi = 2.0$) measurements reported by Burcat et al., are compared to the current study. The uncorrected lean ignition time data, presented in Fig. 5.7, show good agreement among all three studies with respect to the ignition time temperature dependence, although a quantitative comparison is not possible due to the variation in test conditions among the studies. Therefore, each study was scaled to the conditions of 5 atm and 10% O$_2$ (see Fig. 5.8) using the pressure and mixture strength ignition time sensitivities presented in Eq. 4.7. All three scaled data sets are shown to be in good agreement, which further validates the *n*-heptane ignition time pressure and mixture strength sensitivities at conditions other than stoichiometric.

The uncorrected rich ignition time data of the current study are compared to the measurements of Burcat et al. in Fig. 5.9, in which the data sets are shown to vary by more than an order of magnitude due to the wide variation in the range of conditions presented. These measurements were similarly scaled to the conditions of 5 atm and 10% O$_2$ (see Fig. 5.10) using the *n*-heptane ignition time sensitivities presented in Eq. 4.7. Although the current data and the low mixture strength data set of Burcat et al. are shown to be in good agreement when scaled by *n*-heptane ignition time sensitivities, the high mixture strength data set of Burcat et al. falls about a factor of two below the other measurements. These findings suggest that while the *n*-heptane pressure and mixture strength sensitivities presented in Eq. 4.7 may not be applicable to relatively strong mixtures (i.e., high fuel and oxygen concentrations) under rich conditions, they do appear to hold for mixtures of relatively low dilution (i.e., < 7% O$_2$) at rich conditions. In addition, based on the relatively good agreement among the lean and stoichiometric scaled ignition time measurements, it is concluded that the *n*-heptane pressure and mixture strength sensitivities measured here are valid over a wide range of conditions at both lean and stoichiometric conditions.
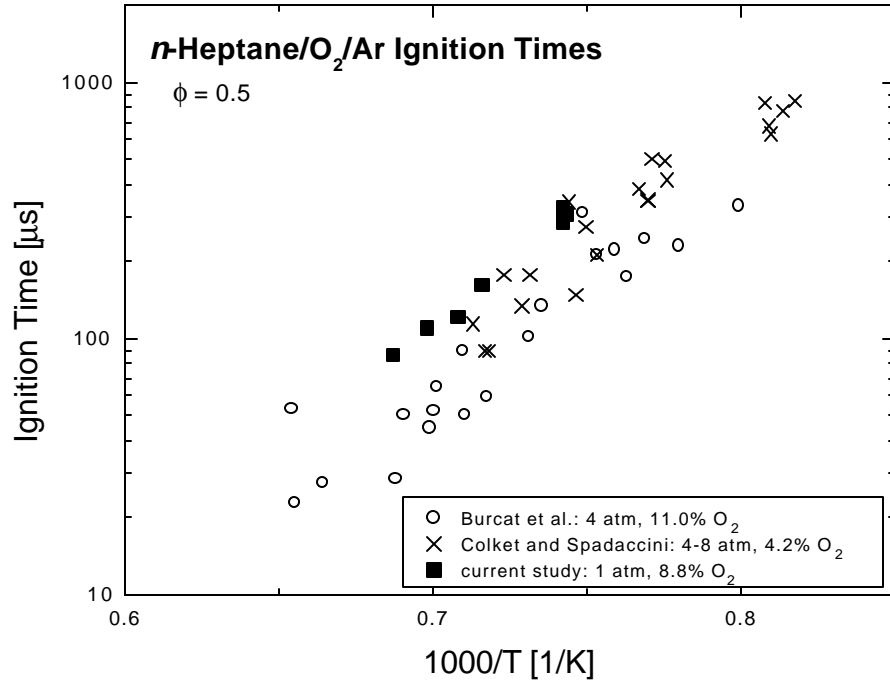
Fig. 5.7 Comparison of lean ($\phi = 0.5$) *n*-heptane ignition time studies.
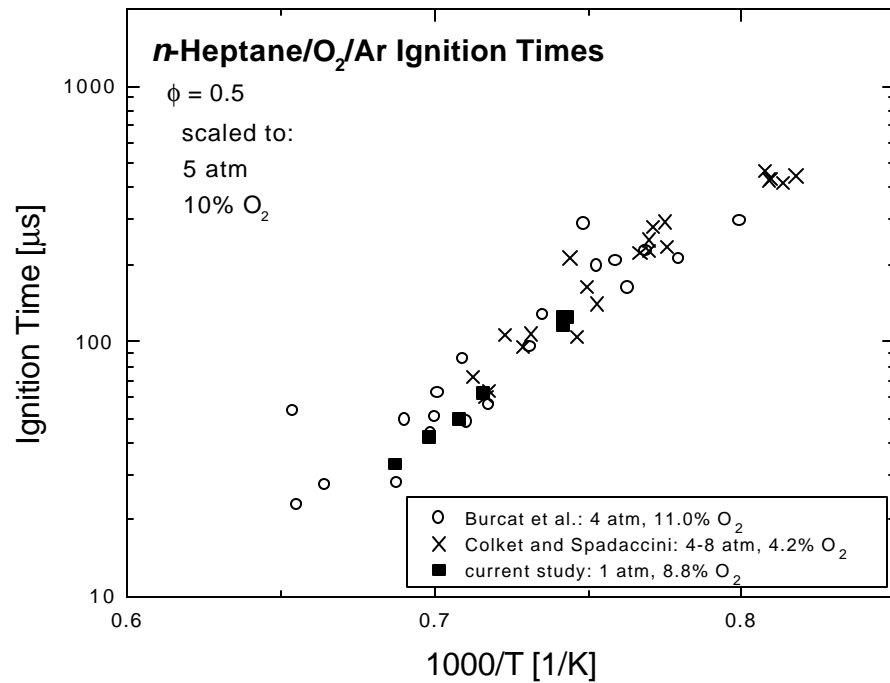
Fig. 5.8 Comparison of lean (ϕ = 0.5) *n*-heptane ignition time studies (scaled to 5 atm, 10% O₂).
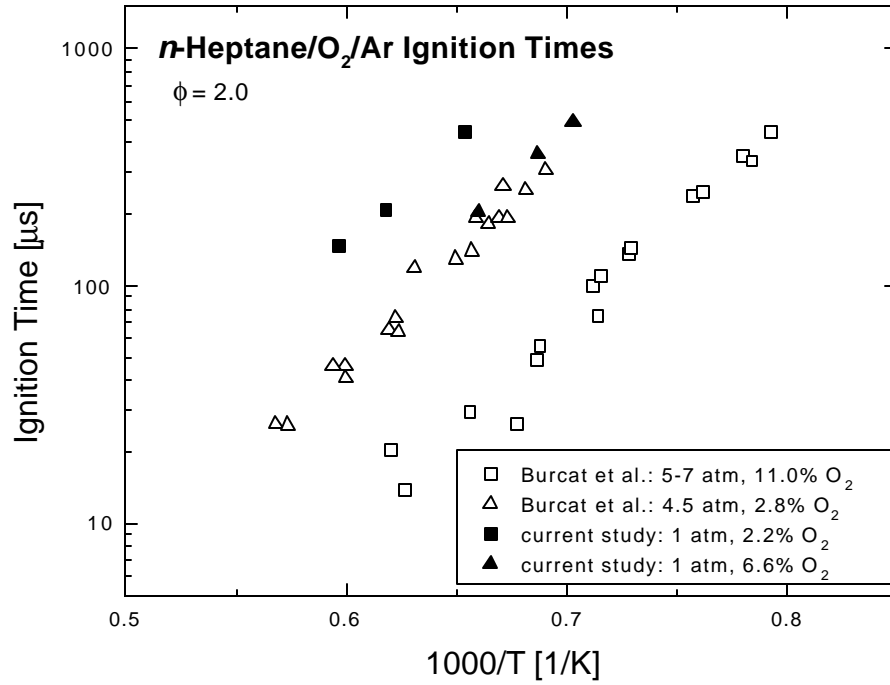
Fig. 5.9 Comparison of rich (ϕ = 2.0) *n*-heptane ignition time studies.

Fig. 5.10 Comparison of rich (f = 2.0) *n*-heptane ignition time studies (scaled to 5 atm, 10% O_2).

In addition to scaling measurements to a common condition, as presented above, the *n*-heptane measurements may also be compared by analyzing the respective ignition time correlations that were derived in each study (see Table 5.1). To facilitate this comparison, the ignition time correlation form utilized to represent the current work is that of Eq. 4.2a, in which the ignition time is expressed in terms of the fuel and oxygen concentrations. Although only the study of Colket and Spadaccini employs this exact correlation form, the other studies shown in Table 5.1 utilize a form that is very similar, thus enabling a number of comparisons to be made among the these studies.

Table 5.1 Previous *n*-heptane/O_2/Ar ignition time correlations.

Correlation	P [atm]	X_f [%]	f	
$\tau = 5.08 \times 10^{-10} \text{ [total mixture]}^{-0.86} \text{ e}^{46,350/RT}$	1-4	2.5	1.0	Vermeer et al.
$\tau = 6.76 \times 10^{-9} \text{ [}n\text{-C}_7\text{H}_{16}]^{0.4} \text{ [O}_2]^{-1.2} \text{ e}^{40,160/RT}$	4-8	0.2	0.5, 1.0	Colket and Spadaccini[*]
$\tau = 3.20 \times 10^{-6} \text{ [}n\text{-C}_7\text{H}_{16}]^{0.2} \text{ [O}_2]^{-1.1} \text{ [Ar]}^{0.6} \text{ e}^{35,300/RT}$	2-12	0.5-3.0	0.5-2.0	Burcat et al.
$\tau = 4.54 \times 10^{-8} \text{ [}n\text{-C}_7\text{H}_{16}]^{0.95} \text{ [O}_2]^{-1.58} \text{ e}^{45,000/RT}$	1-6	0.2-1.8	0.5-2.0	current study

[*]*correlation is based on the ignition time data from a number of previous studies.*

The temperature sensitivity measured by Vermeer et al. is in very good agreement with the value obtained in this study, while that measured by Burcat et al. is much lower. The temperature sensitivity reported by Colket and Spadaccini is based on the ignition time measurements from a number of studies, including the four studies compared in Table 5.1. Thus, it is logical that the value of the ignition time temperature dependence given by Colket and Spadaccini falls between that measured by Burcat et al. and the values given by Vermeer et al. and this study.

In addition to the temperature dependence, the correlations presented in Table 5.1 enable the ignition time pressure sensitivity of each study to be compared, which may be inferred from the sum of the concentration dependencies (see Eq. 4.5). The pressure sensitivities reported by each study are presented in Table 5.2, for which the values are shown to vary from $n = -0.3$ to -0.86. The pressure sensitivity reported in this study falls between the higher value given by Vermeer et al. and the lower value measured by Burcat et al. The value reported by Colket and Spadaccini, which was determined from a collection of all the data from these studies, is shown to be slightly lower than the value given by Vermeer at al.

Table 5.2 Previously measured ignition time pressure sensitivities.

	Pressure sensitivity
Vermeer et al.	-0.86
Colket and Spadaccini	-0.8
Burcat et al.	-0.3
current study	-0.61

5.2.4 *n*-Decane

Due to the difficulty in preparing gaseous test mixtures composed of liquid fuels that have a very low vapor pressure, few *n*-decane ignition time measurements have been reported for shock tube studies. The studies that have been previously conducted usually involve shock-heating *n*-decane in the liquid phase, in either droplet form [41] or as a liquid film [42]. Clearly, the ignition time measurements of such studies are affected by physical processes (see Section 2.1), making it difficult to directly compare these studies to the current work, which was conducted with the fuel in the gaseous phase.

The only previous *n*-decane ignition time study found to be comparable to the current study is that by Pfahl and Adomeit [43], in which a heated shock tube was utilized to study relatively strong *n*-decane/O_2/N_2 gaseous mixtures. Although the diluent utilized in the Pfahl and

Adomeit study (nitrogen) is different from that used here (argon), previous shock tube studies [25,33] have found that there is little difference between the ignition delay times when measurements obtained in argon are compared to those in which the diluent was nitrogen. The ignition time measurements presented for the Pfahl and Adomeit study were obtained in the reflected shock region, and the onset of ignition was defined from the rapid rise in pressure, which was measured at a sidewall location 15 mm from the shock tube endwall. Although sidewall ignition time measurements have been shown to be susceptible to errors at relatively short ignition delays (see Section 3.4.3), most of the measured ignition delay times by Pfahl and Adomeit are sufficiently long that these measurement errors are likely to be negligible.

A comparison of the uncorrected n-decane ignition measurements is presented in Fig. 5.11. The low temperature measurements of Pfahl and Adomeit are shown to fall in the negative temperature coefficient (NTC) region, for which the ignition time is seen to decrease with increasing temperature over the range of about 700-900 K. The NTC region is a characteristic of the low temperature ignition delay behavior of many hydrocarbons fuels [7,8,12,14]. Furthermore, the measurements by Pfahl and Adomeit were obtained at a much higher pressure and mixture strength relative to this study, making it difficult to directly compare these two studies.

A comparison of the Pfahl and Adomeit study to the current work is shown in Fig. 5.12, for which the ignition time measurements of both studies have been scaled to the conditions of 5 atm and 10% O_2 using the ignition time sensitivities given by the n-alkane correlation of Eq. 4.9. Although the temperature ranges of the two studies do not overlap, extrapolation of the Pfahl and Adomeit data to higher temperatures is shown to be in good agreement with the current study. Considering the wide variance in the experimental conditions between the two studies, this agreement between the corrected data sets further validates the scaling method presented here for comparing ignition time measurements. Furthermore, the agreement between these two n-decane studies suggests that the ignition time pressure and mixture strength sensitivities of n-

decane, which were not measured directly in this study, are similar to the values given by the *n*-alkane correlation presented in Eq. 4.9.
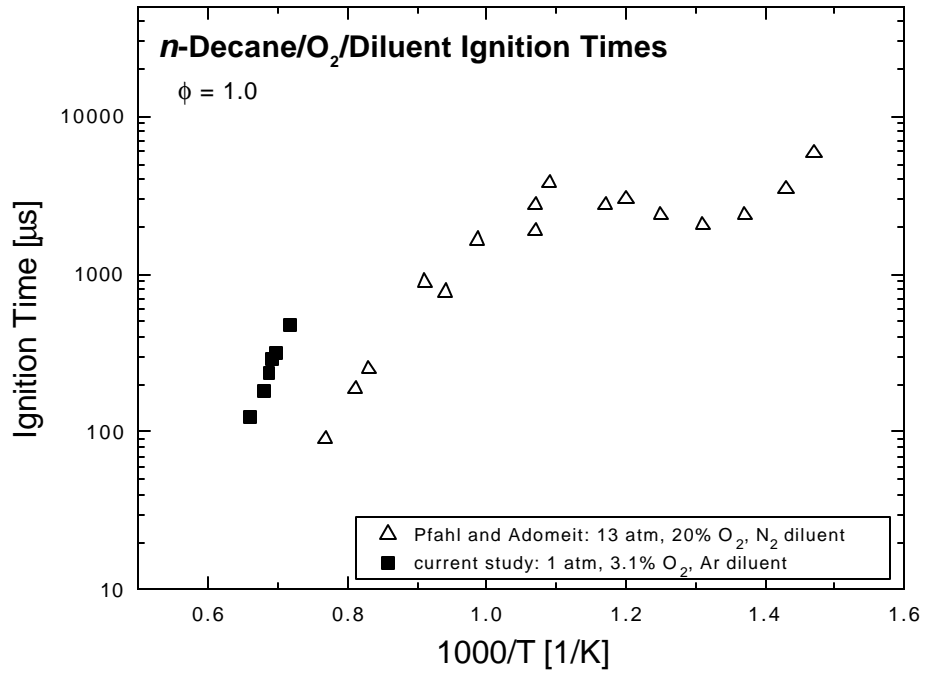
Fig. 5.11 Comparison of *n*-decane ignition time studies.
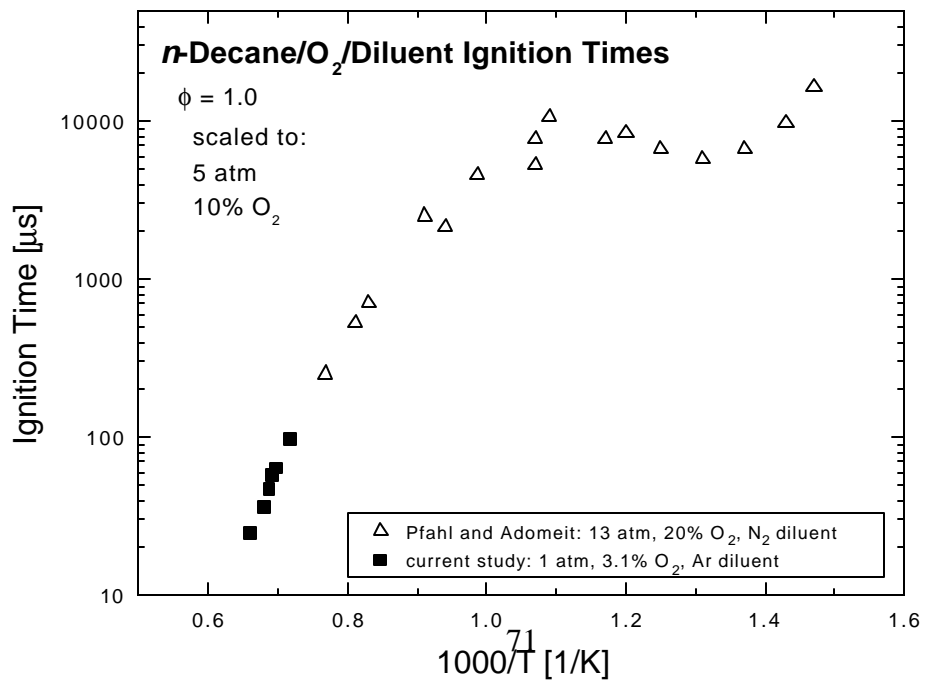
Fig. 5.12 Comparison of *n*-decane ignition time studies (scaled to 5 atm, 10% O$_2$).

5.2.5 *n*-Alkane Series

To further validate the ignition time sensitivities presented in this study, the current *n*-alkane ignition time measurements were compared to the previous study by Burcat et al. [34], in which the ignition delays of propane, *n*-butane, and *n*-pentane were also shown to systematically decrease with increasing fuel size. A comparison of the current work to the Burcat et al. study was achieved by scaling the ignition time data of both studies to the condition of 10 atm and 20% O$_2$ using the ignition time sensitivities given by the *n*-alkane correlation of Eq. 4.9. Also, in order to further verify the *n*-alkane carbon sensitivity measured here (-0.50), each fuel was scaled to a carbon number (*C*) of 4 using the same scaling procedure described previously for the pressure and mixture strength (see Eq. 5.1). While this value for the carbon number is arbitrary, a comparison at any other value produces the same relative trend among the fuels.

As shown in Fig. 5.13, when the Burcat et al. data are scaled by the ignition time sensitivities presented here, the propane, *n*-butane, and *n*-pentane ignition time data sets are accurately collapsed into a single line. This result further supports the carbon number sensitivity of -0.50 measured in this study over a wider range of conditions and for another fuel (*n*-pentane), which was not studied in the current work. However, although all three scaled Burcat et al. data sets are shown to accurately collapse into a single line, the ignition time measurements of Burcat et al. are somewhat shorter than those obtained in this study. This same result is shown in comparing the Burcat et al. *n*-butane ignition time measurements to the current study (see Section 5.2.2), for which it is suggested that the shorter ignition delays reported by Burcat et al. may be due to differences in the ignition time definitions employed in each case. That is, the onset of ignition is defined here as the time at which the rate of increase in the CH emission

signal is a maximum, while the study by Burcat et al. employs a definition that is based on the initial rise of either a pressure or heat-flux trace. However, both studies directly measure the ignition time at the shock tube endwall, which prevents the measurement errors discussed previously in Section 2.3.2.

The measurements of Burcat et al. also result in a slightly lower ignition time temperature sensitivity relative to the current work. Therefore, at higher temperatures these two studies are in good agreement, while at lower temperatures the data sets begin to diverge. As shown in the previous comparisons of past works to the current study, differences among studies regarding the ignition time temperature sensitivity is one of the major causes of discrepancies when comparing these measurements.
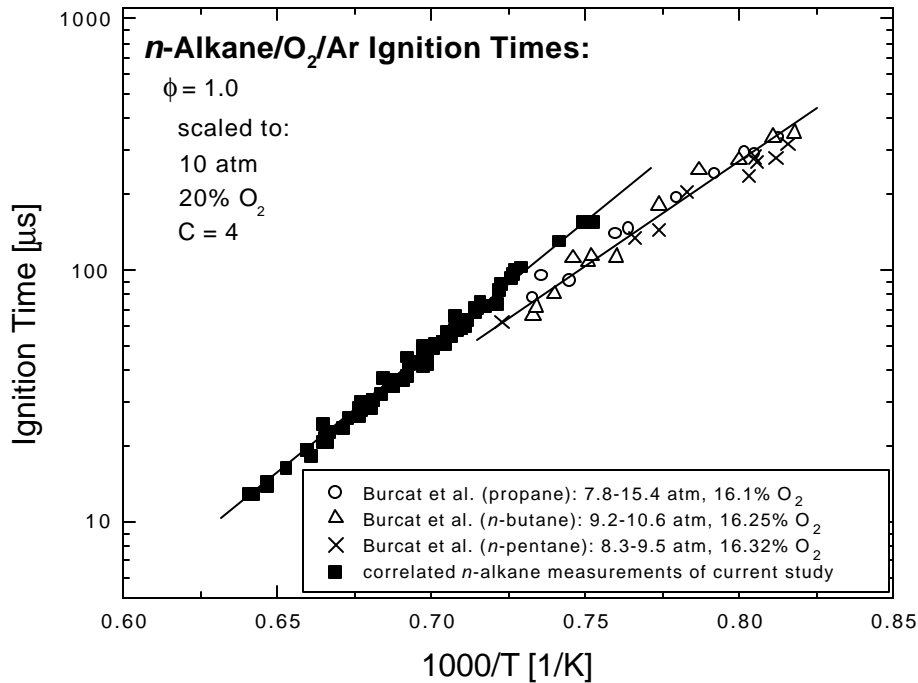
Fig. 5.13 Comparison of *n*-alkane ignition time studies (scaled to 10 atm, 20% O$_2$, C = 4).

5.3 PREVIOUS ETHYLENE STUDIES

The ethylene ignition time measurements of the current study have been compared to the previous studies by Drummond [44], and Hidaka et al. [45]. Both of these past works utilized the reflected shock technique. In the study by Drummond, the onset of ignition was defined as the time of maximum OH emission, while the study by Hidaka et al. based this definition on the initial rise of a CH emission trace. A comparison of these two previous studies to the current work is presented in Fig. 5.14, in which the raw, unscaled data are presented.

For a mixture strength of 6.0% O_2 at nominally 1 atm, the work of Drummond and the current study are quantitatively in good agreement, although the ignition time temperature dependence measured by Drummond appears to be higher than that found in the current study. However, as shown previously in Section 4.3, the ignition time temperature dependence for ethylene increases at higher pressures, and thus may account for the slightly higher activation energy measure by Drummond (1-1.8 atm) relative to the current study (1 atm). At conditions of 3.0% O_2, the work of Hidaka et al. and the current study are in good agreement, both quantitatively and with respect to the measured ignition time temperature sensitivity.
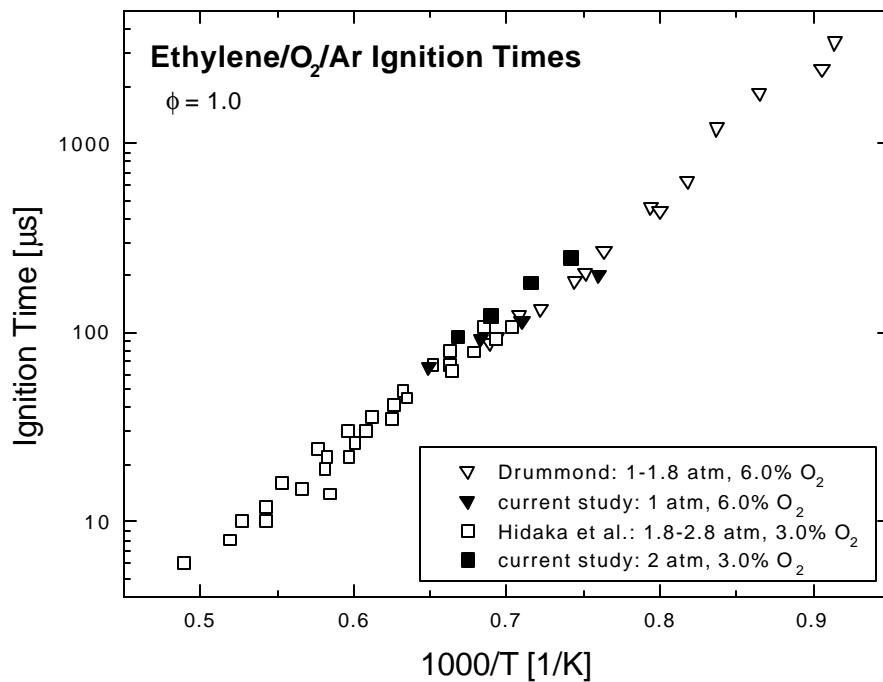
Fig. 5.14 Comparison of ethylene ignition time studies.

Chapter 6

Detailed Modeling of Ignition Times

This chapter presents a comparison of the current ignition time measurements for propane, n-butane, n-heptane, n-decane and ethylene to the predictions of various detailed chemical models. The propane, n-decane, and ethylene measurements, for which the pressure and mixture strength ignition time sensitivities were not directly measured, are compared only to the absolute values and the ignition time temperature sensitivities predicted by the models. However, the ignition time measurements of n-butane and n-heptane for the current study are compared to both the ignition time sensitivities and the absolute values predicted by each model. These predicted sensitivities were calculated over a range of conditions, comparable to the current study, using the method described in following section.

6.1 DETERMINATION OF PREDICTED IGNITION TIMES

Detailed chemical models do not explicitly compute ignition delay times, and therefore these values must be inferred from the output of the model. One method of determining the predicted ignition time is to base this definition on the time-history of a particular species that is known to rapidly form at the time of ignition, similar to the method employed in many experimental studies. Since the empirical ignition times reported in this study are determined from the emission of CH, one potential definition for the predicted ignition delay is the time interval between the start of the reaction (i.e., t = 0), and the time at which the CH concentration is predicted to reach its maximum value. However, the light emitted by CH is produced by electronically excited CH (denoted CH*), not ground-state CH, and thus the predicted CH* concentration is a more appropriate indicator of the ignition time. Since detailed

models do not typically include electronically excited species, the predicted CH* concentration must be inferred from its formation reaction [46],

$$C_2H + O \rightarrow CH^* + CO \qquad\qquad [R\ 6.1]$$

where the product of the predicted C_2H and O-atom concentrations may be used to infer the time-history of CH*.

A third potential definition for the predicted ignition time is based on the time-history of OH. In this case, it is more convenient to define the onset of ignition as the time at which the OH formation rate reaches its maximum value since, for the conditions studied here, the predicted OH trace does not exhibit a well-defined "peak" at the time of ignition, but rather shows a rapid rate formation, followed by a relatively slow decay.
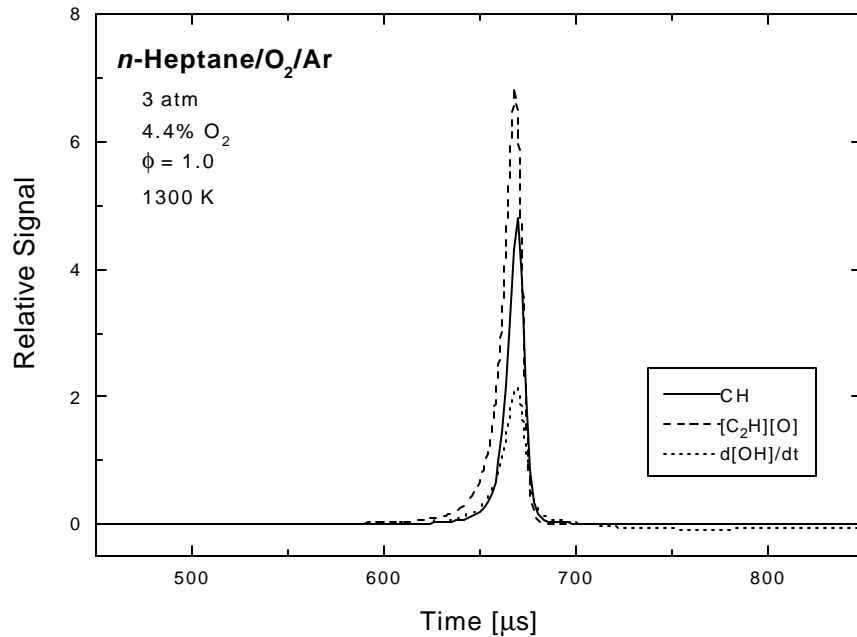
Fig. 6.1 Comparison of potential ignition time definitions for detailed modeling.

As shown by the representative traces in Fig. 6.1, all three potential definitions for the predicted ignition time yield essentially the same value. This agreement was verified for a number of models, and over a wide range of conditions. Therefore, to facilitate the analysis, the predicted ignition time values were defined as the time at which the predicted CH concentration reaches its maximum value.

In addition to the absolute ignition time values, the n-butane and n-heptane models utilized in this study were also compared to the empirical results by determining the ignition time sensitivities predicted by each model. The ignition time temperature sensitivity predicted by each model was determined from the slope of a best-fit line of the logarithm of the ignition time versus reciprocal temperature, holding all other parameters (i.e., pressure, mixture composition) constant. The predicted ignition time pressure and mixture strength sensitivities (s) were determined from a best-fit line of a log-log plot of the ignition time versus the parameter of interest (Q), holding all other parameters constant. Using this method, the ignition time sensitivities may be calculated from the slope of this best-fit line, according to the following expression.

$$log\ \boldsymbol{t} \sim s\ log\ Q \qquad \text{[Eq. 6.1a]}$$
$$\boldsymbol{t} \sim Q^{s} \qquad \text{[Eq. 6.1b]}$$

The ignition time equivalence ratio sensitivity predicted by each model presented in this study did not follow a simple logarithmic scaling as shown in Eq. 6.1, and thus was not calculated.

6.2 n-ALKANE MECHANISMS

6.2.1 Propane

The propane ignition time measurements of the current study were compared to the detailed chemical models of Marinov et al. [47] and Qin et. al [40], which are described in

detail in Section 8.1. A comparison of the predicted and measured ignition times for propane are presented in Fig. 6.2. Although the Marinov et al. model is shown to accurately predict the ignition time temperature sensitivity, it overpredicts the measured ignition time by about a factor of two. In contrast, the Qin et al. model underpredicts ignition time temperature sensitivity by about 10%, and underpredicts the measured ignition time by about 30%. A sensitivity analysis conducted on the models revealed that the predicted ignition time is sensitive to the initial rate of propane decomposition. Thus, the propane decomposition reactions utilized by these two models are analyzed in greater detail in Section 8.1. In addition, the decomposition of propane has been further examined by a series of experiments described in Chapter 7.
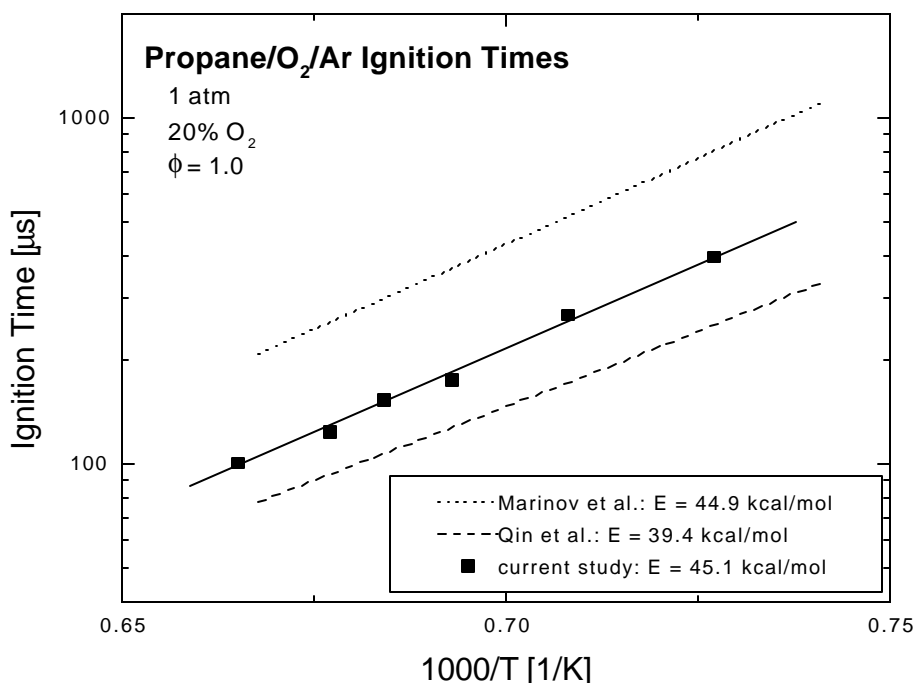
Fig. 6.2 Predicted ignition time temperature sensitivity for propane.

6.2.2 *n*-Butane

The *n*-butane ignition time measurements were compared to the mechanism developed by Marinov et al. [47], which is the same model utilized in the previous section on propane. A quantitative comparison of the predicted and measured ignition times, and the ignition time

temperature sensitivity, is shown in Fig. 6.3. At higher temperature, there is good agreement between model and experiment in terms of the absolute ignition time. However, the model is shown to slightly underpredict the ignition time temperature sensitivity measured empirically, and thus the model begins to underpredict the experimental values at the temperature decreases.
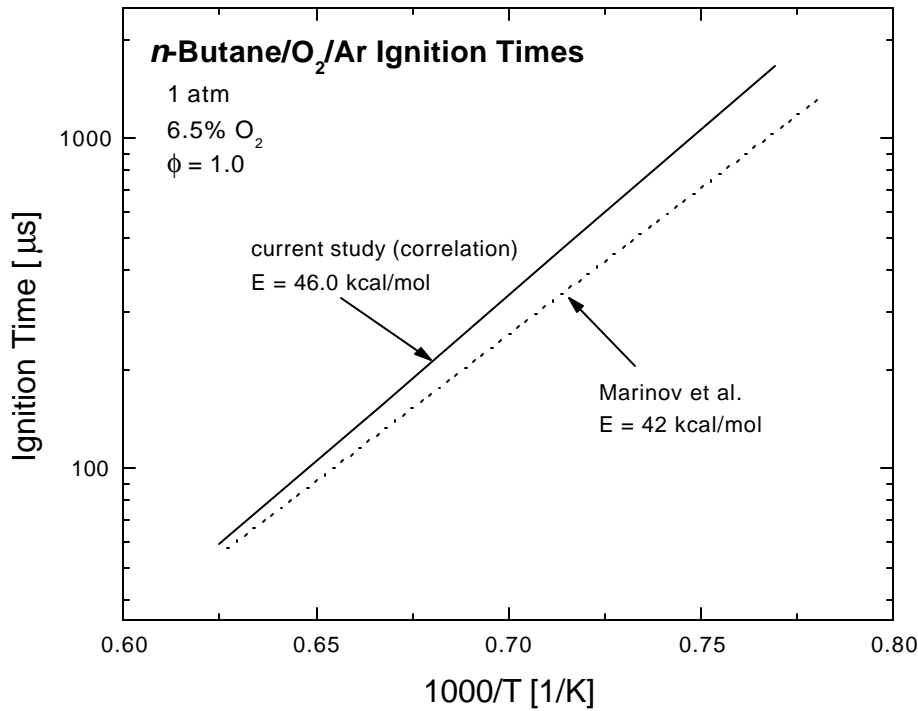
Fig. 6.3 Predicted ignition time temperature sensitivity for *n*-butane.

Using the method described in Section 6.1, the predicted ignition time sensitivities of *n*-butane to pressure and mixture strength were determined at stoichiometric conditions (see Table 6.1). These values were found to vary by less than ±5% over the range of experimental conditions studied. The ignition time equivalence ratio sensitivity predicted by the Marinov et al. model exhibits the same general trend found experimentally (i.e., increasing sensitivity with increasing stoichiometry), and thus the ignition time equivalence ratio sensitivity could not be determined.

Table 6.1 Ignition time sensitivities for stoichiometric *n*-butane/O₂/Ar mixtures.

Activation energy [kcal/mol]	Pressure sensitivity	Mixture strength sensitivity	
42	-0.50	-0.67	Marinov et al.
46.0	-0.55	-0.66	current study

In comparing the ignition time sensitivities for *n*-butane, it is evident that the values predicted by Marinov et al. are in good agreement with those measured empirically. The model predicts essentially the same mixture strength sensitivity found here, and underpredicts the temperature and pressure sensitivities by approximately 10%. However, the ignition delay of *n*-butane is much more sensitive to temperature than any other parameter, and thus slight differences in the predicted activation energy may lead to significant errors in the ignition time at some conditions. Therefore, the ability of a model to correctly predict ignition times is largely dependent on the agreement between the predicted and measured ignition time temperature dependence.

6.2.3 *n*-Heptane

The *n*-heptane ignition time measurements of the current study were compared to three detailed chemical models - Held et al. [48], Lindstedt and Maurice [49], and Curran et al. [50]. All three models are described in detail in Section 8.3. The ignition times predicted by all three models are presented in Fig. 6.4 over a range of temperatures for a fixed pressure and mixture composition. The ignition time values calculated from the *n*-heptane correlation presented in Eq. 4.7 are also included to quantitatively compare the predicted and experimental values.

The results shown in Fig. 6.4 reveal that there are large discrepancies among the three models with respect to both the absolute ignition time values, and the ignition time temperature sensitivity. Only the model of Curran et al. accurately predicts the *n*-heptane ignition time temperature sensitivity measured in this study. Therefore, although the Curran et al. model slightly underpredicts the absolute values measured in this study, reasonable agreement is achieved over a relatively wide range of temperatures. The model of Lindstedt and Maurice is shown to predict a much lower ignition time temperature sensitivity than that measured

empirically, and thus overpredicts the empirical ignition time values at high temperature, and underpredicts these values at lower temperatures.
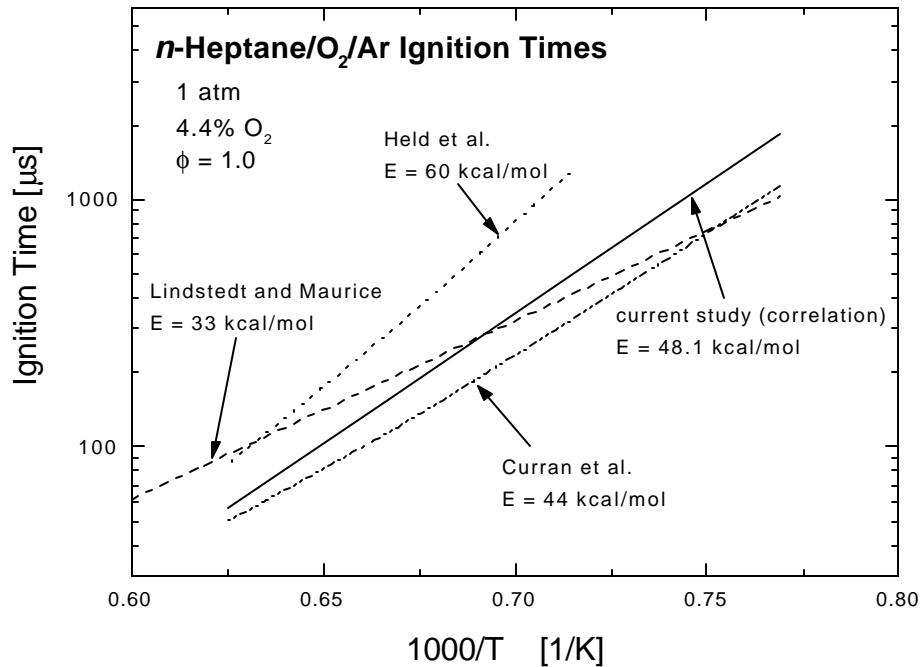
Fig. 6.4 Predicted ignition time temperature sensitivity for *n*-heptane.

The model of Held et al. predicts a much higher temperature sensitivity than that found experimentally, and thus severely overpredicts the measured ignition time at low temperatures, while achieving somewhat better agreement at higher temperatures. However, the ignition time temperature sensitivity predicted by the Held et al. model was found to significantly decrease at higher mixtures strengths, reaching a value of 32 kcal/mol at a mixture strength of 20% O_2, which is well below the value measured experimentally. Therefore, at high mixtures strengths the Held et al. model, similar to the Lindstedt and Maurice model, overpredicts the experimental ignition time values at high temperature and underpredicts the ignition time at lower temperatures.

To further compare the three *n*-heptane models, the ignition time pressure sensitivities predicted by each model were calculated using the method described in Section 6.1 (see Fig. 6.5). Although each model predicts a slightly different ignition time pressure sensitivity, they all predict this value to be constant over a wide range of pressures. That is, when the ignition time is presented as a function of pressure on a log-log plot, the resulting trendlines are linear for all three models. Hence, the detailed models further support the empirical trend found in this study, for which the ignition time pressure sensitivity of *n*-heptane was found to follow a simple logarithmic relationship.
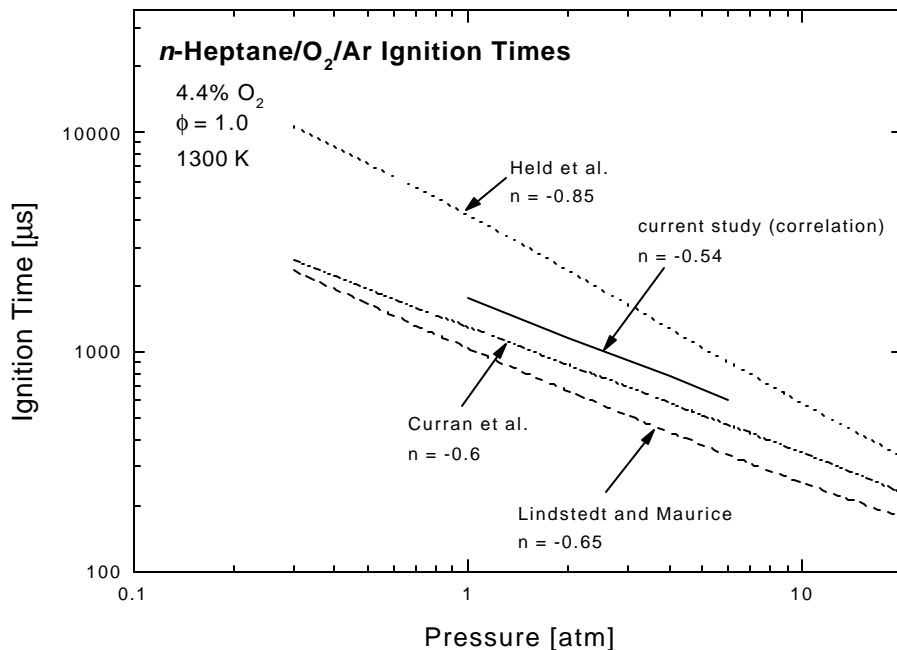
Fig. 6.5 Predicted ignition time pressure sensitivity for *n*-heptane.

In comparing the stoichiometric ignition time pressure sensitivities presented in Fig. 6.5, it is evident that both the model of Curran et al. and Lindstedt and Maurice accurately predict the experimental value. These predicted sensitivities were also found to vary by less than ±5% over the range of conditions studied. However, the model of Held et al. not only overpredicts the empirical pressure sensitivity at the conditions presented in Fig. 6.5, but also predicts that

the pressure dependence decreases with increasing temperature, reaching a value of -0.5 at 1500 K.

The ignition time mixture strength sensitivities predicted by each model were also determined (see Fig. 6.6). Both the models of Curran et al. and Lindstedt and Maurice are shown to predict a constant mixture strength sensitivity over a wide range of mixture strengths, which further validates the simple logarithmic relationship between the ignition time and mixture strength as suggest by the experimental data. Furthermore, both these models closely predict the mixture strength sensitivity measured in this work. However, the model of Held et al. is shown to predict an increasing sensitivity with increasing mixture strength, and thus the ignition time mixture strength sensitivity could not be determined for this model.
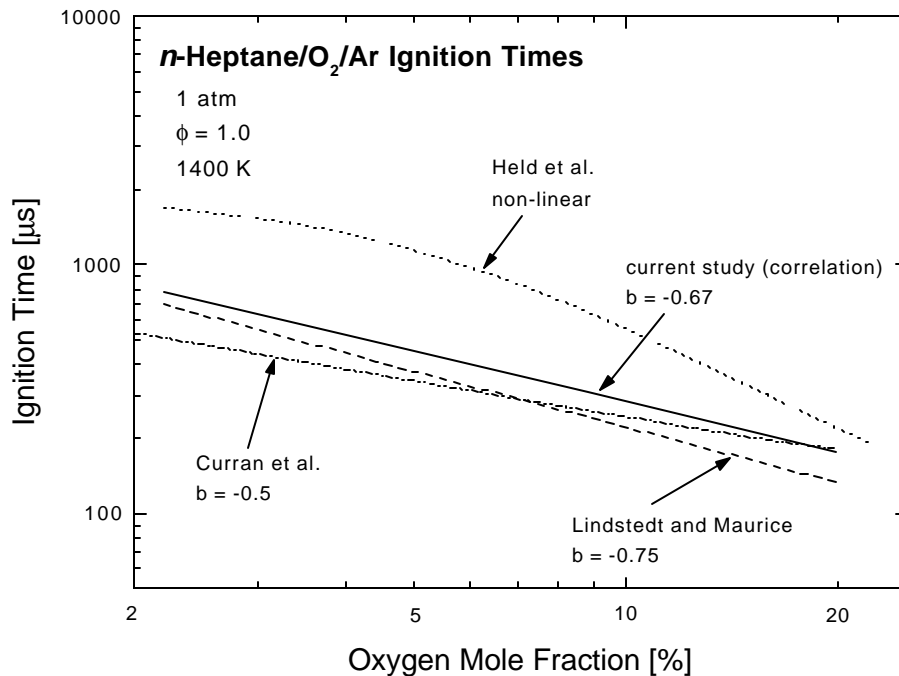
Fig. 6.6 Predicted ignition time mixture strength sensitivity for *n*-heptane.

The measured and predicted stoichiometric ignition time sensitivities for *n*-heptane are summarized in Table 6.2. Although the pressure and mixture strength sensitivities predicted by

the models of Curran et al. and Lindstedt and Maurice are in good agreement with the experimental values, only the model of Curran et al. accurately predicts the ignition time temperature sensitivity measured in this study. In addition, the Held et al. model was found to predict a large variation in the ignition time sensitivities over the range of conditions studied here, while the sensitivities predicted by the Curran et al. and Lindstedt and Maurice models were found to vary by only a few percent.

Table 6.2 Ignition time sensitivities for stoichiometric *n*-heptane/O₂/Ar mixtures.

Activation energy [kcal/mol]	Pressure sensitivity	Mixture strength sensitivity	
32 to 60	-0.5 to -0.85	non-linear	Held et al.
33	-0.65	-0.75	Lindstedt and Maurice
44	-0.6	-0.5	Curran et al.
48.1	-0.54	-0.67	current study

To further compare the detailed models to the current work, the effect of the equivalence ratio on the ignition time was analyzed in a similar manner as that shown for pressure and mixture strength. The predicted equivalence ratio sensitivities are presented in Fig. 6.7, for which it is shown that all three models predict the same trend that was observed experimentally. That is, that the ignition delay of *n*-heptane is relatively insensitive to the equivalence ratio under fuel-lean conditions, and becomes much more sensitive as the stoichiometry of the test mixture increases. This same general trend is also predicted by the detailed model of Marinov et al. [47] for both propane and *n*-butane, and has been reported in a previous ignition time study [51].

85
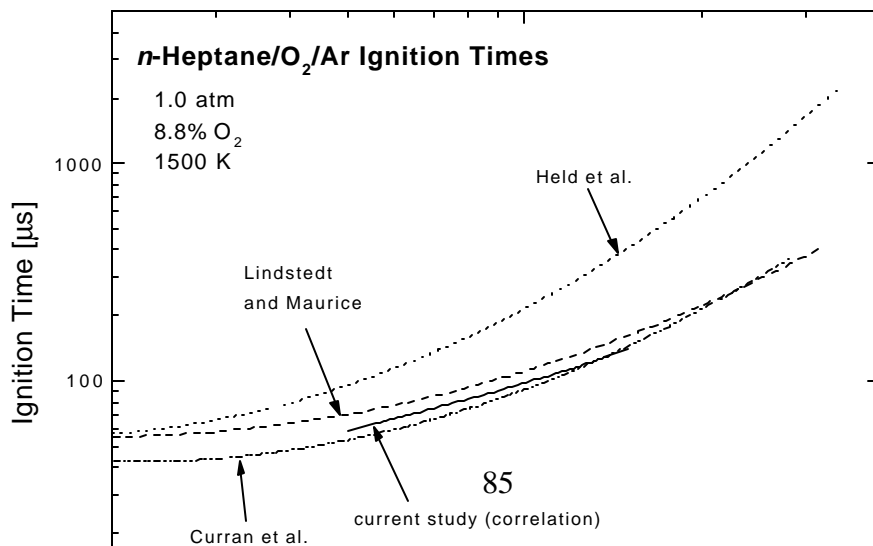
Fig. 6.7 Predicted ignition time equivalence ratio sensitivity for *n*-heptane.

6.2.4 *n*-Decane

The experimental *n*-decane ignition time measurements were compared to the *n*-decane model of Lindstedt and Maurice [52], which is based on the same mechanism that was previously utilized to model *n*-heptane [49], with the addition of 27 species and 166 reactions to account for the initial decomposition reactions of *n*-decane. Hence, it is expected that the general trends predicted by this *n*-decane model will be similar to those previously determined for the Lindstedt and Maurice *n*-heptane mechanism. As shown in Fig. 6.8, the Lindstedt and Maurice *n*-decane model significantly underpredicts the ignition time temperature sensitivity measured in this study, which is similar to the result presented for *n*-heptane. Furthermore, the *n*-decane temperature sensitivity predicted by this model is almost identical to that for *n*-heptane. This suggests that the ignition time temperature sensitivity predicted by the Lindstedt and Maurice model is largely controlled by the chemical sub-mechanisms contained within this model, and not the initial fuel decomposition reactions.
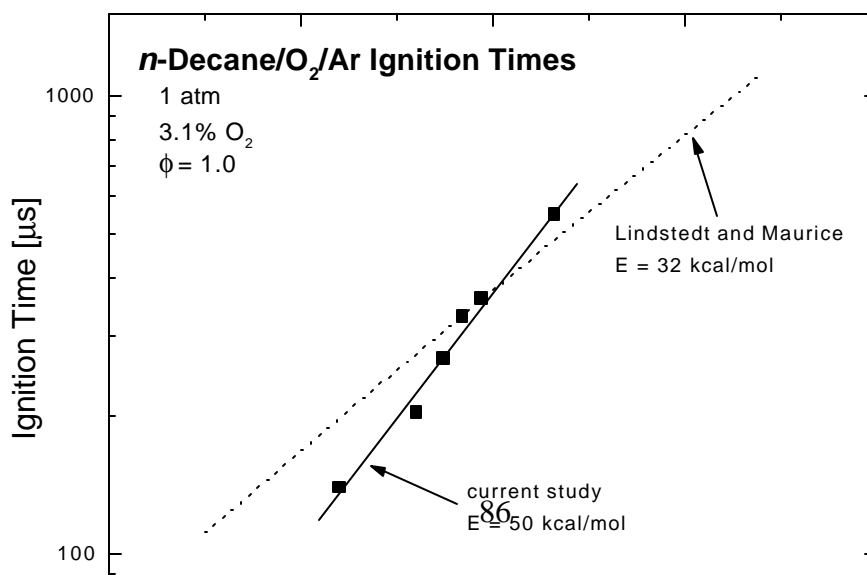
6.3 ETHYLENE MECHANISM

The ethylene ignition time measurements of the current study are compared to the GRI mechanism [53], which was originally developed to model the oxidation of natural gas. The GRI model is compared to the ethylene ignition delays measured here over a range of pressures (see Fig. 6.9). The model is shown to predict a similar increase in the ignition time temperature sensitivity at higher pressures, but underpredicts the empirical ignition time values by roughly 10-30% over the range of conditions presented, with the best agreement achieved for the 1 atm condition.

Ethylene/O$_2$/Ar Ignition Times

6.0% O$_2$
$\phi = 1.0$

soild lines - current study
dashed lines - GRI

Ignition Time [µs]

500

100

87

1 atm

The ignition delay of ethylene was found to be relatively sensitive to its initial decomposition rate, which is largely controlled by reaction R 6.2.

$$C_2H_4 + M \rightarrow C_2H_3 + H + M \qquad\qquad [R\ 6.2]$$

Therefore, the increase in the ignition time temperature sensitivity with increasing pressure may be explained by analyzing the rate expression for this reaction. For the conditions of this study, reaction R 6.2 is pressure dependent, falling between the low- and high-pressure reaction rate limits. Furthermore, the high-pressure limit rate for reaction R 6.2 is more temperature sensitive than the corresponding low-pressure limit rate, and therefore as the pressure is increased, the rate of ethylene decomposition becomes more temperature sensitive, which in turn results in an increase in the ignition time temperature sensitivity. This effect was not observed when modeling the ignition delay of the *n*-alkanes since, over the range of conditions studied, the decomposition of these fuels occurs much closer to the high-pressure limit.

Ethylene/O$_2$/Ar Ignition Times

1 atm

$\phi = 1.0$

3.0% O$_2$

6.0% O$_2$

12% O$_2$

88

Ignition Time [µs]

1000

100
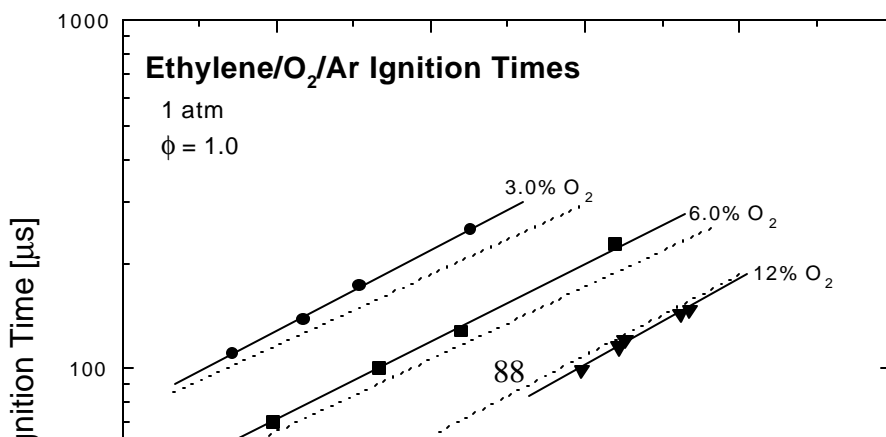
Fig. 6.10 Predicted ethylene ignition times at 3, 6, and 12% O$_2$.

The ethylene ignition times predicted by the GRI model are compared to the results of this study in Fig. 6.10 at mixture strengths of 3, 6, and 12% O$_2$. Over the range of mixtures strengths studied at 1 atm, the model and experiment show good agreement in terms of the ignition time temperature sensitivity and the absolute ignition time values, with the best agreement achieved at this highest mixture strength (12% O$_2$). Furthermore, the model predicts that the ignition time temperature dependence of ethylene is essentially constant over a wide range of mixtures strengths, which is the same trend found experimentally. Therefore, the GRI model is found to closely predict the ignition time temperature and mixture strength sensitivities of ethylene, as well as the absolute ignition time values, at atmospheric pressure and stoichiometric conditions. This is in contrast to the results observed in comparing the predicted laminar flames speeds of this mechanism to experimental measurements. That is, the GRI model is found to overpredict the laminar flame speeds of ethylene by approximately 30% for fuel-air mixtures at 1 atm and 300 K [53]. The current results suggest that improvement of the GRI mechanism may be attained by more precisely determining the unimolecular rate of reaction R 6.2 in the intermediate pressure region between the low- and high- pressure limits.

Chapter 7

Thermal Decomposition Measurements

This chapter presents the experimental results for the thermal decomposition of propane, *n*-butane, *n*-heptane, and *n*-decane over the temperature range of 1500-2100 K. The decomposition of highly dilute mixtures of fuel and argon was monitored by a lamp absorption diagnostic (see Section 3.3.2), which was utilized to resolve the time-history of ethylene during the fuel decomposition process. The resulting ethylene traces were then compared to the predictions of detailed chemical models, and the ethylene yield measured for each fuel is analyzed based on chemical pathways by which each fuel is predicted to decompose. In addition, the detailed modeling is utilized to compare the predicted time-histories of ethylene for both an oxidizing and non-oxidizing reaction scheme to further assess the role of ethylene in practical combustion reactions.

7.1 CORRECTIONS TO ABSORPTION MEASUREMENTS

The absorption traces obtained in this study were corrected to account for the formation of interfering species that also absorb at the wavelength of the lamp diagnostic (174 nm). The important interfering species are predicted to be acetylene and propene (interference due to 1,3-butadiene was predicted to be negligible for all fuels and conditions studied). The raw absorption traces were corrected via the following relation,

$$I/I_{0, corrected} = I/I_{0, raw} \cdot P e^{\sum_{i=1}^{n} a_i L r X_i(t)} \qquad \text{[Eq. 7.1]}$$

where the mole fractions $X_i(t)$ of the interfering species (i.e., acetylene and propene) are based on the predictions of the detailed models, and the values of the absorption coefficients, $\boldsymbol{a}$, are based on the absorption measurements presented in Section 3.3.2. After the corrected absorption trace is calculated from Eq. 7.1, the ethylene mole fraction is then readily obtained from the Beer-Lambert relationship (Eq. 3.1).

7.2 THERMAL DECOMPOSITION OF n-ALKANES

7.2.1 Propane

The measured ethylene traces for the decomposition of propane were compared to the models of Marinov et al. [47] and Qin et al. [40]. A representative ethylene trace for the decomposition of propane is shown in Fig. 7.1, for which both the corrected and uncorrected traces are presented to show the magnitude of this difference. In comparing the modeled and experimental ethylene traces, it is apparent that there are a number of marked differences. First, both models predict a very similar ethylene trace, with the Qin et al. model predicting a slightly faster rate of ethylene formation and higher ethylene concentration. Also, relative to the experimental ethylene trace, the rate of ethylene formation predicted by both models is found to be much slower than that shown by the empirical data trace, and both models predict less ethylene than the measured value.

The predicted and measured ethylene traces may be further compared by plotting the maximum ethylene mole fractions measured for the pyrolysis of propane over a range temperatures (see Fig. 7.2). Error bars have been added to the experimental data as an estimate of the uncertainty due to the presence of interfering species. Both the models underpredict the maximum ethylene mole fraction measured here over a wide temperature range. However, the Marinov et al. model and the experimental data show that this value is essentially constant with respect to temperature, while the model of Qin et al. predicts a slight decrease in the ethylene yield with increasing temperature. In addition, the results in Fig. 7.2

show that the empirical ethylene yield measured for propane is approximately 1, where the ethylene yield is defined as the ratio of the maximum ethylene mole fraction to the initial fuel mole fraction.

Fig. 7.1 Temporal variation of ethylene for the thermal decomposition of propane.
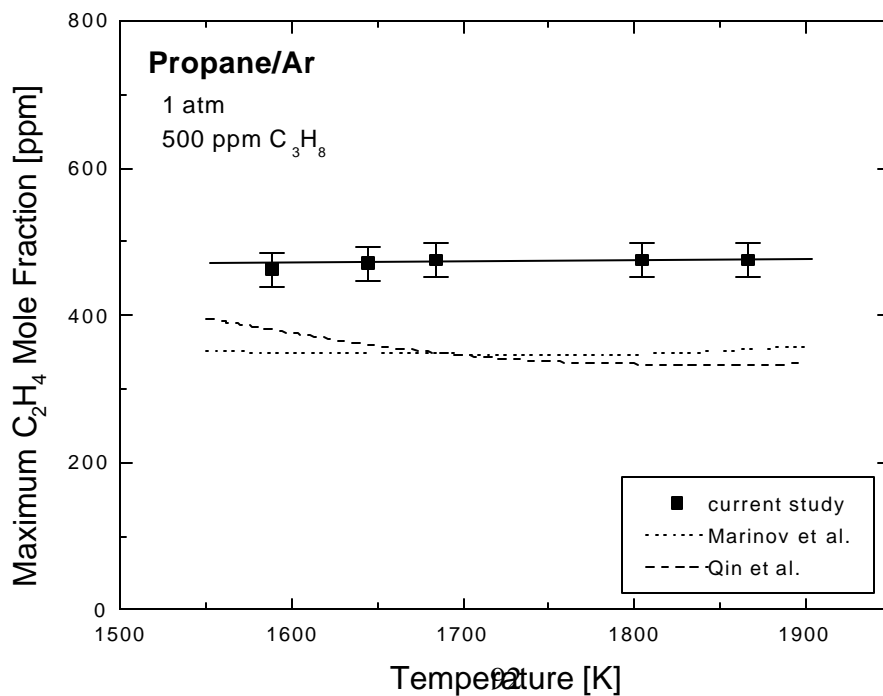
Fig. 7.2 Maximum ethylene concentration produced from the thermal decomposition of propane.

To provide further insight into the ethylene results, the decomposition of propane is analyzed in terms of the detailed chemical reactions that are predicted to control the thermal decomposition process.   The decomposition of propane is summarized by the scheme presented in Fig. 7.3, for which it is shown that two of the thermal decomposition pathways lead to the formation of ethylene. However, the third channel is shown to lead to the formation of propene, which is converted into mainly acetylene via a series of intermediate steps. Thus the empirical results, for which the ethylene yield of propane was measured to be approximately one, suggest that the decomposition channel that leads to the formation of i-propyl is relatively slow compared to the other two decomposition pathways. This result is also suggested by the previous work of Lifshitz and Frenklach [54], in which the pyrolysis of propane was shown to produce significantly higher levels of ethylene, relative to propene, at high temperature (> 1500 K).

$$C_3H_8$$

+M	+H	+H
$C_2H_5 + CH_3$	n-$C_3H_7 + H_2$	i-$C_3H_7 + H_2$
+M	+M	+M
$C_2H_4 + H$	$C_2H_4 + CH_3$	$C_3H_6 + H$
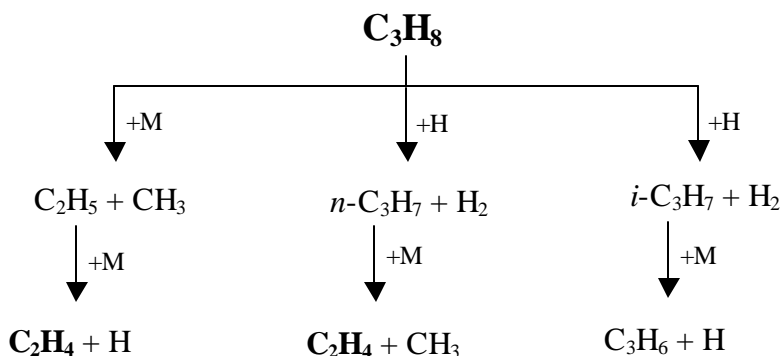
Fig. 7.3 Reaction pathways for the thermal decomposition of propane.

7.2.2 *n*-Butane

The experimental ethylene traces obtained for the decomposition of n-butane were compared to the model of Marinov et al. [47].   A representative ethylene trace for the

decomposition of *n*-butane is compared to the model in Fig. 7.4, for which the predicted interference of acetylene and propene are shown to be relatively small. The model accurately predicts the rapid rate of ethylene formation, but slightly underpredicts the maximum ethylene concentration by approximately 10%. Furthermore, the model predicts a slightly faster ethylene removal rate than that found experimentally.
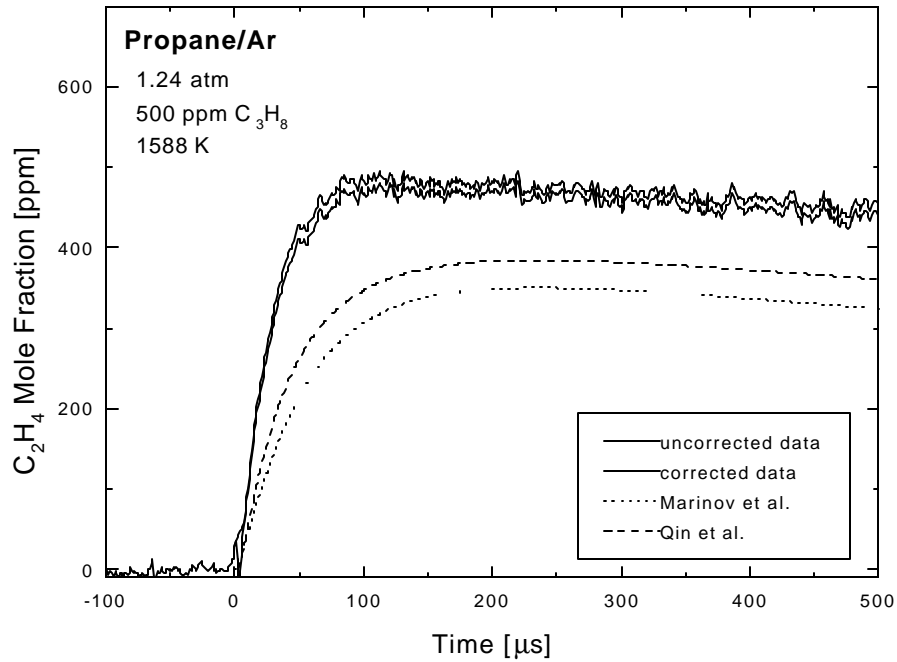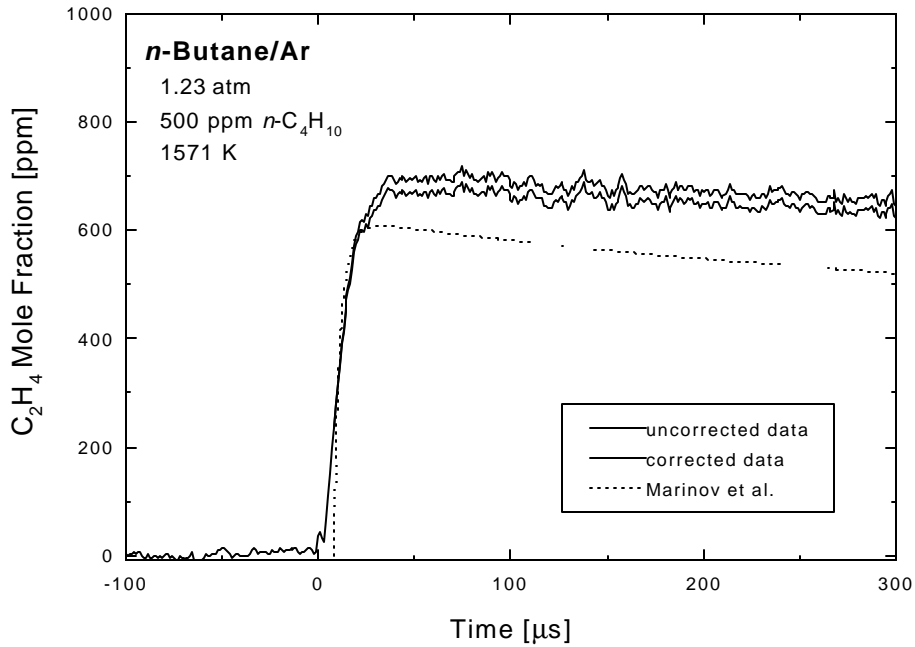

Fig. 7.4 Temporal variation of ethylene for the thermal decomposition of *n*-butane.
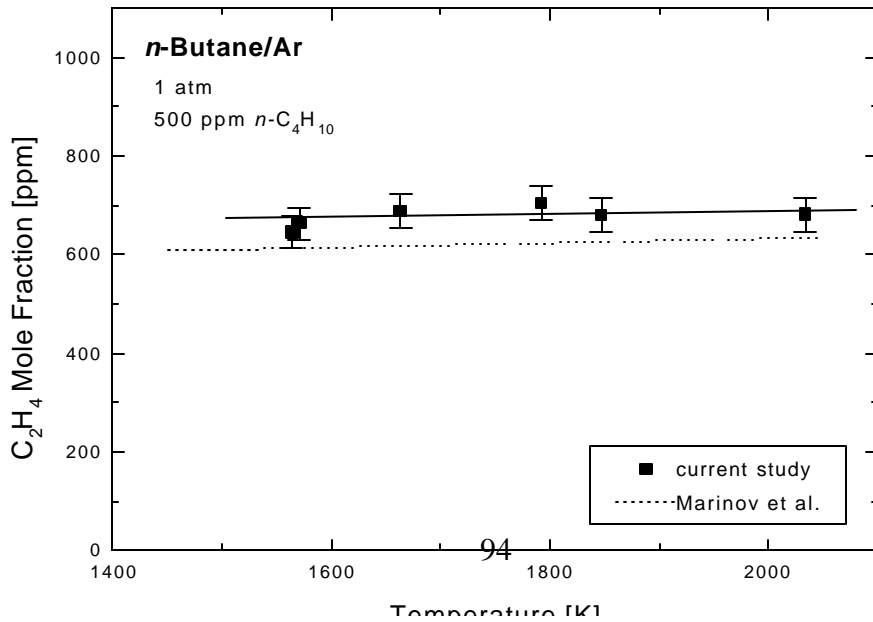
Fig. 7.5 Maximum ethylene concentration produced from the thermal decomposition of *n*-butane.

The maximum ethylene concentration measured for the thermal decomposition of *n*-butane is compared to that predicted by the Marinov et al. model in Fig. 7.5. Again, error bars have been added to the experimental data to account for the uncertainty in the measurement due to interfering species. Both the predicted and measured ethylene yields are shown to be constant over the range of temperatures studied, and there is good agreement in terms of the absolute value of ethylene yield. The ethylene yield of *n*-butane measured empirically is about 1.4, while the value predicted by the Marinov et al. model is nominally 10% lower.

The decomposition scheme for *n*-butane is summarized in Fig. 7.6. In comparing the decomposition channels for *n*-butane and propane (see Fig. 7.3), it is apparent that there is an important difference between these two fuels regarding their decomposition reactions. That is, the decomposition of *n*-butane occurs near the unimolecular high-pressure limit, which is why, by convention, the collision partner designation (M) has been omitted from initial *n*-butane decomposition reactions. In contrast, the initial decomposition of propane occurs in the fall-off region, and thus its effective decomposition rate is dependant on the concentration of the collision partners. As a result, for the conditions of this study, H-atom abstraction reactions are not predicted to be influential in the decomposition of *n*-butane, while they are for propane. Thus, the thermal decomposition of *n*-butane is predicted to occur predominantly by the breaking of either its interior or exterior C-C bonds, leading to only two major pyrolysis channels.

$$n\text{-}C_4H_{10}$$

95

$$n\text{-}C_3H_7 + CH_3 \qquad\qquad C_2H_5 + C_2H_5$$
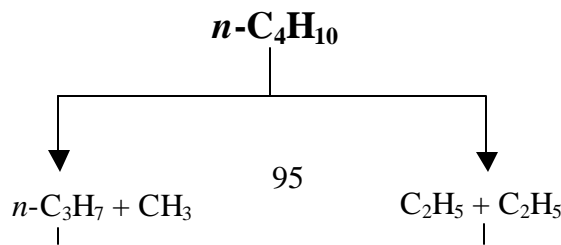
Fig. 7.6 Reaction pathways for the thermal decomposition *n*-butane.

7.2.3 *n*-Heptane

The formation of ethylene measured during the pyrolysis of *n*-heptane is compared to the detailed chemical models of Held et al. [48], Lindstedt and Maurice [49], and Curran et al. [50] in Fig. 7.7. The corrected data trace is based on the predicted acetylene and propene time-histories given by the Lindstedt and Maurice model, however the corrected absorption traces predicted by the other two models were not found to be significantly different from that shown in Fig. 7.7. All three models were found to predict a rapid formation of ethylene, similar to trend observed experimentally. However, all three models show significant differences in terms of the absolute ethylene yield and the rate of ethylene removal. Both the Held et al. and Lindstedt and Maurice models closely predict the maximum measured ethylene concentration, however the Held et al. model predicts a much faster rate of ethylene removal than that measured here, while the model of Lindstedt and Maurice shows a much slower removal rate. Also, the Curran et al. model is shown to significantly underpredict the ethylene yield measured here, and predicts an ethylene removal rate that is comparable to the Held et al. model, but which is must faster than that suggested empirically.

n-Heptane/Ar
1.38 atm
250 ppm *n*-C_7H_{16}
1667 K

uncorrected data
corrected data
Lindstedt and Maurice
Held et al.
Curran et al.

96
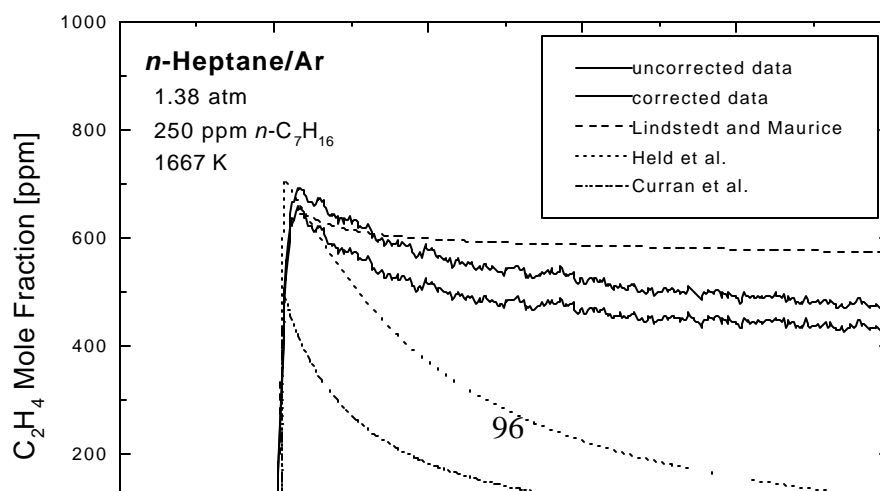
Fig. 7.7 Temporal variation of ethylene for the thermal decomposition of *n*-heptane.

A comparison of the measured and predicted maximum ethylene concentrations for the pyrolysis of *n*-heptane is presented in Fig. 7.8. Over the range of temperatures studied, the experimental results show that the ethylene yield is essentially constant, with a value of approximately 2.5. In addition, the Curran et al. and Held et al. models also predict that the ethylene yield of *n*-heptane is essentially constant above 1600 K, but both models predict a slight decrease in the ethylene yield at lower temperatures. Also, the Curran et al. model predicts an ethylene yield that is about 20-25% lower than the measured value, while that predicted by the Held et al. model is slightly higher than the empirical value. In contrast, the Lindstedt and Maurice model is shown to predict an increase in the ethylene yield with increasing temperature. Therefore, while the Lindstedt and Maurice model is in good agreement with the experimental values at lower temperatures, the model overpredicts the measured maximum ethylene concentration at higher temperatures by about 15%.
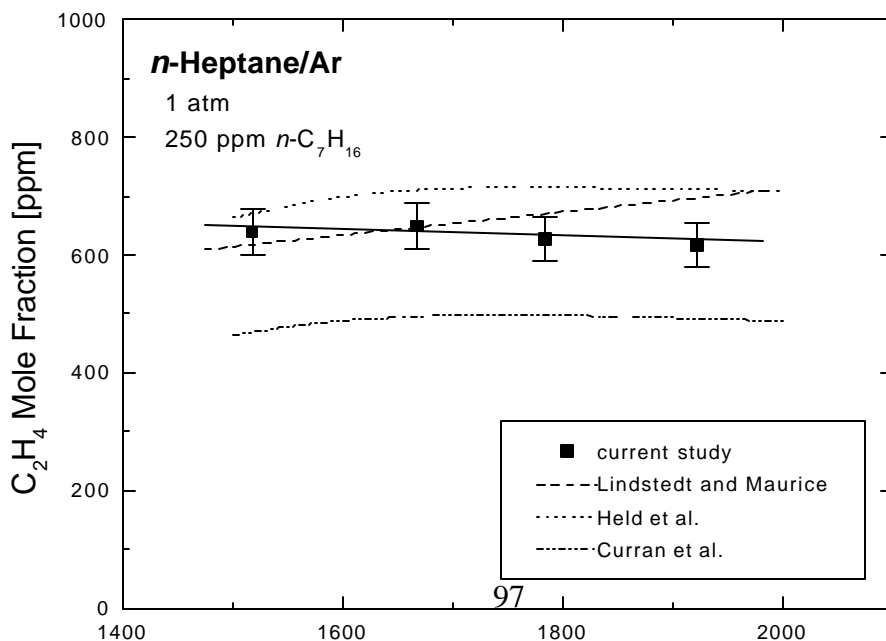
Fig. 7.8 Maximum ethylene concentration produced from the thermal decomposition of *n*-heptane.

In order to explain the *n*-heptane ethylene yields measured in this study, the decomposition pathways of this fuel were analyzed using the three detailed models presented here. However, the methods employed to develop these *n*-heptane mechanisms were found to be significantly different for each model, thereby making it difficult to come to a definitive conclusion about which decomposition pathways are predicted to be dominant during the pyrolysis of *n*-heptane. A more detailed discussion of the *n*-heptane decomposition pathways predicted by these three models is presented in Section 8.3.

7.2.4 *n*-Decane

The ethylene trace measured for the decomposition of *n*-decane was compared to the *n*-decane mechanism suggested by Lindstedt and Maurice [52]. As shown in Fig. 7.9, the model predicts a higher ethylene concentration than the experimental value, but shows a similar ethylene removal rate to that measured experimentally. As anticipated, the Lindstedt and Maurice model predicts very similar temporal variation of ethylene for *n*-decane and *n*-heptane. In addition, in comparing the results of this model for both of these fuels, it is evident that the absolute value of the predicted ethylene concentrations are largely affected by the decomposition of the parent fuel, while the rate of ethylene decomposition is essentially controlled by the underlying base mechanism for the smaller hydrocarbon species.

The maximum ethylene concentration measured for the thermal decomposition of *n*-decane is compared to the Lindstedt and Maurice model in Fig. 7.10. The model is shown to significantly overpredict the measured values over the entire temperature range studied. In

addition, similar to the trend observed for the Lindstedt and Maurice *n*-heptane model, the maximum ethylene concentration formed during the pyrolysis of *n*-decane is predicted to increase with increasing temperature. However, this trend was not found experimentally, for which the measured ethylene traces were found to be essentially constant over the temperature range of nominally 1500-2100 K.
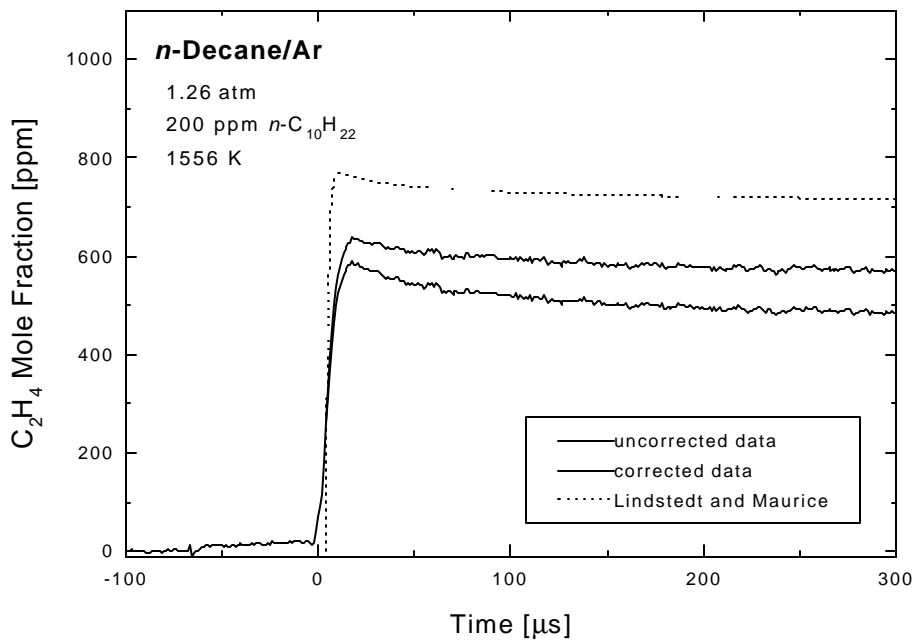
Fig. 7.9 Temporal variation of ethylene for the thermal decomposition of *n*-decane.
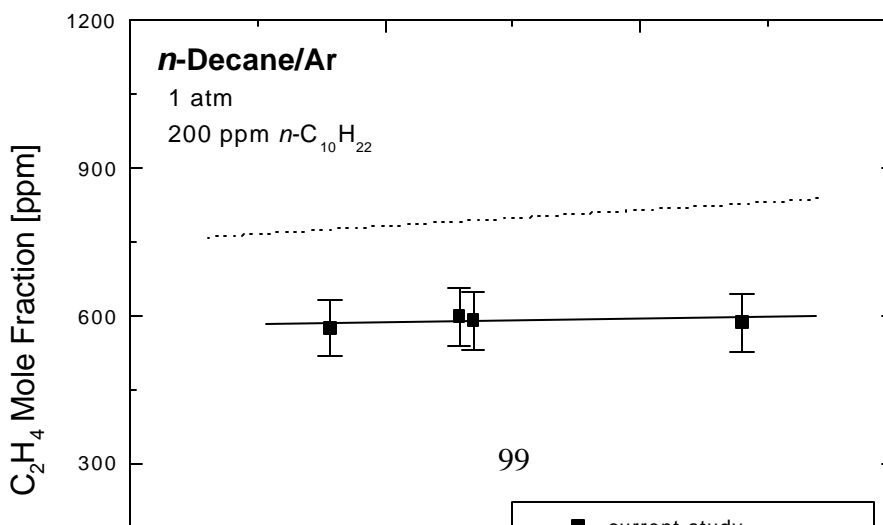
99

7.2.5 Ethylene Yields of *n*-Alkanes

A summary of the ethylene yields measured for the four *n*-alkanes studied here is presented in Fig. 7.11. The ethylene yield of each fuel is shown to systematically increase with increasing molecular size of the *n*-alkane, with values of approximately 1, 1.4, 2.5 and 3 for propane, *n*-butane, *n*-heptane, and *n*-decane, respectively. Also, as discussed previously, the ethylene yield of each fuel is found to be essentially constant over the temperature range studied.

Furthermore, as shown in Fig. 7.12, when the ethylene yields of each fuel are normalized to account for the number of carbon atoms in the *n*-alkane, the ethylene yields are shown to collapse to the same nominal value. That is, at the conditions of the current study, approximately two-thirds of the carbon contained within each *n*-alkane is converted to ethylene during pyrolysis of the fuel. Based on the predictions of the detailed models, the remaining carbon atoms are largely in the form of methyl, with higher predicted levels of propene and other olefins as the size of the *n*-alkane increases.
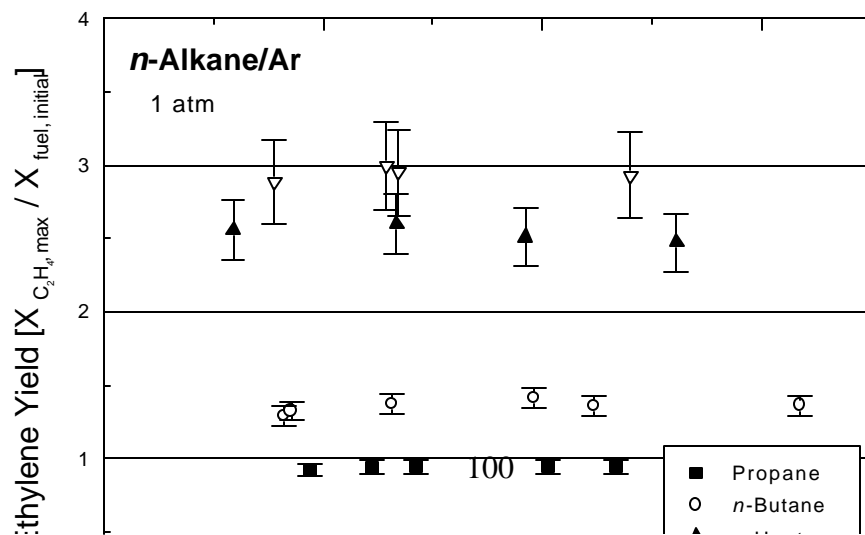
Fig. 7.11 Comparison of ethylene yields for the thermal decomposition of the *n*-alkanes.
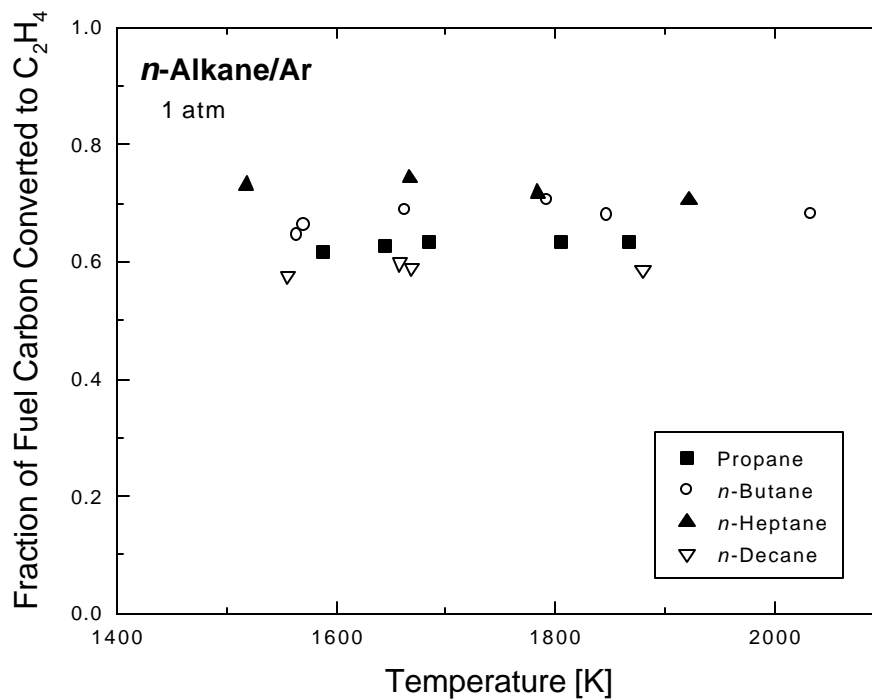
Fig. 7.12 Fraction of *n*-alkane carbon atoms converted to ethylene.

7.3 PREDICTED ETHYLENE TRACE FOR AN OXIDIZING REACTION

All of the previous experimental and computational results of this chapter have been presented for fuel-argon mixtures, and thus oxidation reactions have not considered. However, the autoignition process obviously involves a large number of reactions that include oxygenated

species, and thus the detailed models have been employed to analyze a series of oxidizing reaction schemes as well. The purpose of this analysis is to determine the relevance of pyrolysis measurements to practical fuel-oxidizer mixtures.

The lamp absorption diagnostic utilized in this study was not suitable for measuring the time-history of ethylene for fuel-oxygen test mixtures due to the strong absorption of molecular oxygen and other oxygenated species at this wavelength.   Therefore, the detailed models presented in this study were utilized to compare oxidizing and non-oxidizing reaction sequences under similar conditions. A representative comparison is shown in Fig. 7.13 for *n*-butane using the Marinov et al. model. Although the ethylene is predicted to rapidly decompose for the oxygenated mixture, the initial ethylene yield is essentially the same for both the oxidation ($\phi = 1.0$) and pyrolysis ($\phi = 0.0$) reaction schemes.

In addition, the predicted time of ignition is specified in Fig. 7.13, which, as discussed in Section 6.1, is based on the time at which the CH concentration is a maximum. It is evident that the decomposition of the ethylene is predicted to occur throughout the induction period, which suggests that the oxidation of ethylene is one of the more important reaction sequences during the ignition process. These same general trends were similarly verified for the other *n*-alkanes using the models discussed in this chapter. Hence, based on the predictions of the detailed modeling, it is concluded that the ethylene yields measured here for the *n*-alkanes are also applicable to fuel-oxygen mixtures as well.

n-Butane/Ar

1.23 atm

500 ppm *n*-C_4H_{10}

1571 K

$\phi = 0.0$

$\phi = 1.0$

C_2H_4 Mole Fraction [ppm]

800

600

400

200

102

ignition
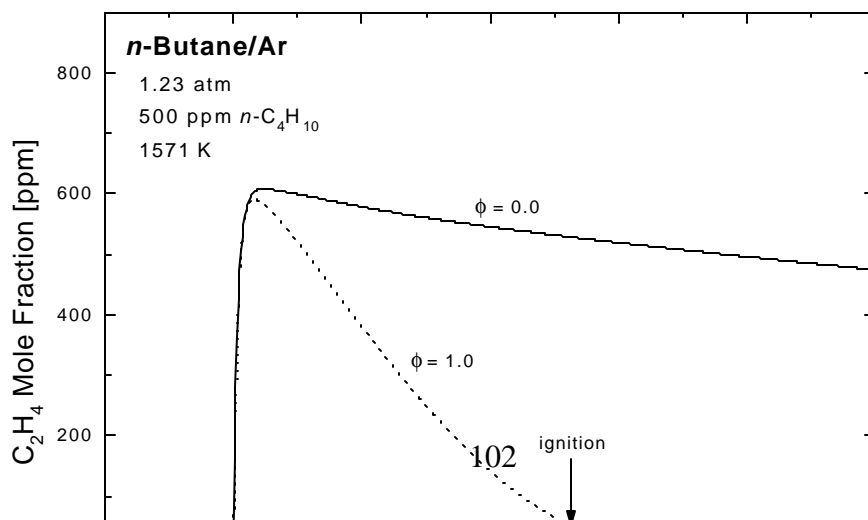
Fig. 7.13 Predicted temporal variation of ethylene for an oxidizing and non-oxidizing reaction.

Chapter 8

Analysis of *n*-Alkane Mechanisms

This chapter contains a more detailed discussion of the *n*-alkane mechanisms utilized in this study. The method by which each model was developed is discussed, and a detailed analysis of each mechanism was performed to determine the key reactions relevant to the pyrolysis measurements presented in this study. From this analysis, and the empirical measurements presented here, the initial propane and *n*-butane decomposition rates were adjusted to determine the effect of these reactions on the predicted ethylene time-histories and ignition delays. In addition, a more detailed analysis of the three *n*-heptane models employed in this study is presented to provide further insight into the reasons for the differences observed among these mechanisms. As shown previously, the *n*-decane mechanism utilized here is essentially identical to that given by Lindstedt and Maurice [49], with the addition of a small *n*-decane sub-mechanism. Therefore, the analysis of the Lindstedt *n*-heptane mechanism, presented below, is also relevant to the *n*-decane mechanism.

8.1 PROPANE

8.1.1 Analysis of Mechanisms

The propane/*n*-butane mechanism given by Marinov et al. [47] was developed to model the formation of aromatics in fuel-rich, atmospheric flames. It was validated using species measurements from an atmospheric flat flame burner, in which ethane, ethylene and methane flames were studied under fuel-rich conditions. The model contains 136 species and 825 reactions. The mechanism by Qin et al. [40] was developed specifically for propane, and contains 70 species and 463 reactions. The Qin et al. model was optimized using ignition delay

measurements of methane, allene, propyne, and propane, and laminar flames speeds of these same four fuels, in addition to the flame speeds of ethylene, ethane and propylene.

A sensitivity analysis was performed on each propane model to determine which rate expressions have the largest effect on the time-history of ethylene. The results of this analysis are shown in Fig. 8.1 for the Marinov et al. model, however the Qin et al. model predicts very similar sensitivities. Specifically, the initial formation of ethylene is predicted by both models to be most sensitive to the following four reactions.

$$C_3H_8 + M \rightarrow C_2H_5 + CH_3 + M \qquad\qquad \text{[R 8.1]}$$

$$C_3H_8 + H \rightarrow n\text{-}C_3H_7 + H_2 \qquad\qquad \text{[R 8.2]}$$

$$C_3H_8 + H \rightarrow i\text{-}C_3H_7 + H_2 \qquad\qquad \text{[R 8.3]}$$

$$C_2H_4 + H \rightarrow C_2H_3 + H_2 \qquad\qquad \text{[R 8.4]}$$
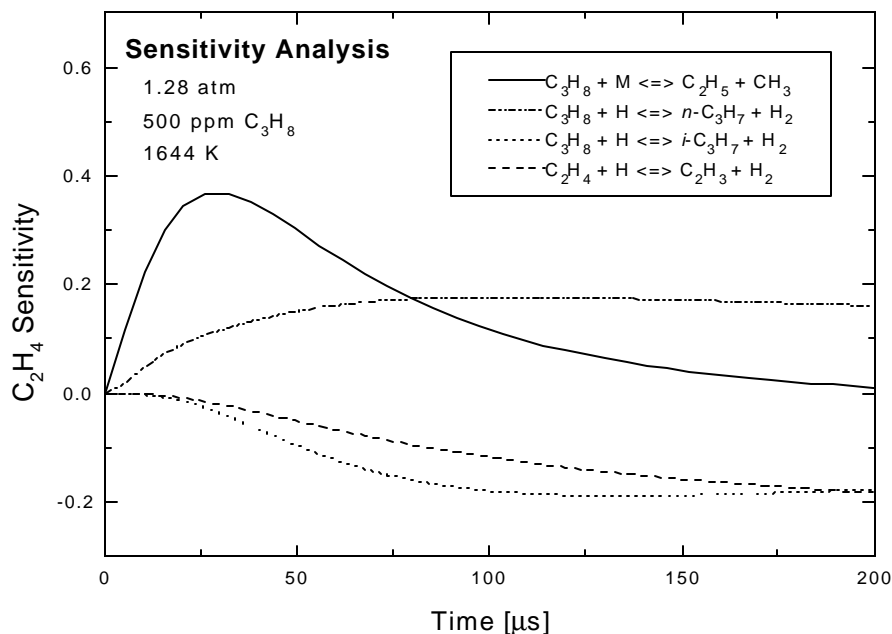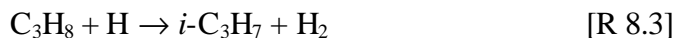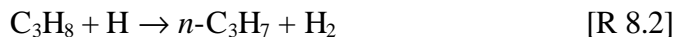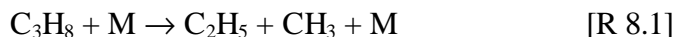
Fig. 8.1 Ethylene sensitivity analysis for the thermal decomposition of propane.

Although not shown in Fig. 8.1 for clarity, at longer times (i.e., > 200 μs) the Marinov et al. model predicts that the following three reactions also become important,

$$C_2H_4 + M \rightarrow C_2H_2 + H_2 + M \qquad \text{[R 8.5]}$$

$$C_2H_4 + CH_3 \rightarrow C_2H_3 + CH_4 \qquad \text{[R 8.6]}$$

$$C_2H_6 + H \rightarrow C_2H_5 + H_2 \qquad \text{[R 8.7]}$$
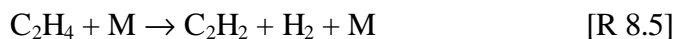
while the Qin et al. model predicts reaction R 8.8 to become influential on the predicted ethylene time-history at longer times.

$$C_3H_6 + H \rightarrow C_2H_4 + CH_3 \qquad \text{[R 8.8]}$$
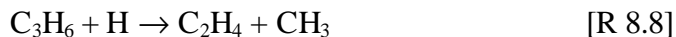
Therefore, to simplify the analysis of the propane mechanisms and the comparison of model and experiment, the focus here will be on ethylene trace at early times, for which there are fewer key reactions to consider. The following paragraphs contain a more detailed description of the propane decomposition rates utilized in each model.

Reaction R 8.1 is the initiation reaction for the pyrolysis of propane. Under the conditions of this study, this unimolecular decomposition rate is pressure dependent, and thus both the low- and high-pressure limit rate expressions are considered. Although numerous studies have attempted to measure both of these reaction rates, there is significant disagreement among studies [55]. The low-pressure rate expression utilized in the Marinov et al. model is from a previous shock tube study by Al-Alami and Kiefer [56], in which the pyrolysis of propane was monitored using the laser-schlieren technique in the incident shock region from 1400-2300 K. Al-Alami and Kiefer present both a low (1400-1800 K) and high (1800-2300 K) temperature rate expression, however the Marinov et al. model employs a single rate expression which is a combination of these two empirical equations. Over the range of conditions studied here, this combined expression was found to yield values within ±10% of those calculated from the two Al-Alami and Kiefer expressions. Although Al-Alami and Kiefer

also report an expression for the high-pressure limit of reaction R 8.1, the rate employed in the Marinov et al. model is that suggested in the literature review by Tsang [57], which, for the conditions of this study, is about a factor of two lower than that reported by Al-Alami and Kiefer. The low- and high-pressure rate expressions utilized in the Qin et al. mechanism are modified versions of those suggested by Tsang [57], in which the rate expressions are increased by a factor of 1.96. Thus, for the conditions studied here, the modified high-pressure rate utilized by Qin et al. yields a value that is similar to that suggested by Al-Alami and Kiefer. The uncertainty of the high- and low-pressure rate expressions for reaction R 8.1 is estimated to be approximately three [57].

There are also discrepancies among studies regarding the rate expressions for the propane H-atom abstraction reactions, R 8.2 and R 8.3. The rate expressions given in the Marinov et al. model for both of these H-atom abstraction reactions are taken from the recommendations of Tsang [57], which are based on only a few low temperature (< 800 K) experimental studies. The model of Qin et al. also employs the H-atom abstraction reaction rates given by Tsang, but modifies reaction R 8.3 by increasing this rate by a factor of two. At the conditions of the current study, the *n*-propyl to *i*-propyl branching ratio is nominally 1.4 for the Marinov et al. model and 0.7 for the Qin et al. model. However, a study by Hidaka et al. [55] suggests this branching ratio is nominally three over the temperature range of 1100-1450 K. This result is based on the relative amounts of ethylene and propene measured for the pyrolysis of propane using the reflected shock technique, in which substantially more ethylene was measured relative to propene. Furthermore, this branching ratio is predicted to increase at higher temperatures due to the higher activation energy of the reaction R 8.2 relative to reaction R 8.3 [57,58].

8.1.2 Modifications to Mechanisms

To more closely match the initial rate of ethylene formation and the ethylene yields measured for the pyrolysis of propane, the rate expressions of the Marinov et al. and Qin et al. models were adjusted as follows. Both the high- and low-pressure rate expressions for reaction

R 8.1 were increased by a factor of three for the Marinov et al. model, and a factor of 1.53 for the Qin et al. model, to produce essentially the same rate expression for each mechanism (the Qin et al. model already includes an increase of a factor of 1.96 for this reaction). Also, the branching ratio of reaction R 8.2 to reaction R 8.3 was set to approximately four. This ratio was determined by extrapolating the value suggested by Hidaka et al. (i.e., three) to the higher temperature range of the current study, based on the relative activation energies of reaction R 8.2 and R 8.3 given by Tsang [57]. This adjustment to the H-atom abstraction branching ratio for each model was achieved as follows.

For the conditions of the current study, the branching ratio of reaction R 8.2 to R 8.3 predicted by the Marinov et al. model was found to be about 1.4. Thus, the rate of reaction R 8.2 was raised by a factor of three, holding reaction R 8.3 constant, in order to increase the branching ratio to the desired value (i.e., four). The branching ratio similarly could have been raised by lowering reaction R 8.3, however in order to increase the predicted rate of ethylene formation, and thus more closely match the experimental ethylene trace, it was necessary to raise reaction R 8.2 without lowering reaction R 8.3. Lowering reaction R 8.3 resulted in a slower rate of ethylene formation, and thus caused a larger discrepancy between model and experiment. The Qin et al. model was adjusted to produce the same rate expressions for reactions R 8.2 and R 8.3 as those employed in the modified Marinov et al. model. Hence, the rate expression of reaction R 8.2 given by Qin et al. was also increased by a factor of three. In addition, reaction R 8.3 was decreased by a factor of two, thereby lowering this rate to the original value suggested by Tsang [57], and that utilized in the Marinov et al. mechanism.

A summary of the adjustments to the Marinov et al. and Qin et al. mechanisms are presented in Table 8.1. In addition, the effect of these adjustments on the predicted ethylene time-histories is presented in Fig. 8.2, for which it is shown that the modified reaction mechanisms are in much better agreement with the experimental ethylene trace. Both modified models accurately predict the measured ethylene formation rate and closely match the measured ethylene yield. The maximum ethylene yield predicted by the modified Marinov et al. model is

within 10% of the experimental value, and the modified Qin et al. model underpredicts the measured ethylene yield by only a few percent. However, both modified reaction mechanisms predict a slightly faster rate of ethylene removal than that measured here. As discussed previously, at longer times the ethylene removal rate becomes sensitive to a number of reactions, making it difficult to draw any definitive conclusions about which rate expression(s) should be modified.

Table 8.1 Modifications to propane mechanisms.

Reaction	Modification to A-factor	
	Marinov et al.	Qin et al.
$C_3H_8 + M \rightarrow C_2H_5 + CH_3 + M$	k_∞ +3x k_0 +3x	k_∞ +1.53x k_0 +1.53x
$C_3H_8 + H \rightarrow n\text{-}C_3H_7 + H_2$	+3x	+3x
$C_3H_8 + H \rightarrow i\text{-}C_3H_7 + H_2$	unchanged	-2x
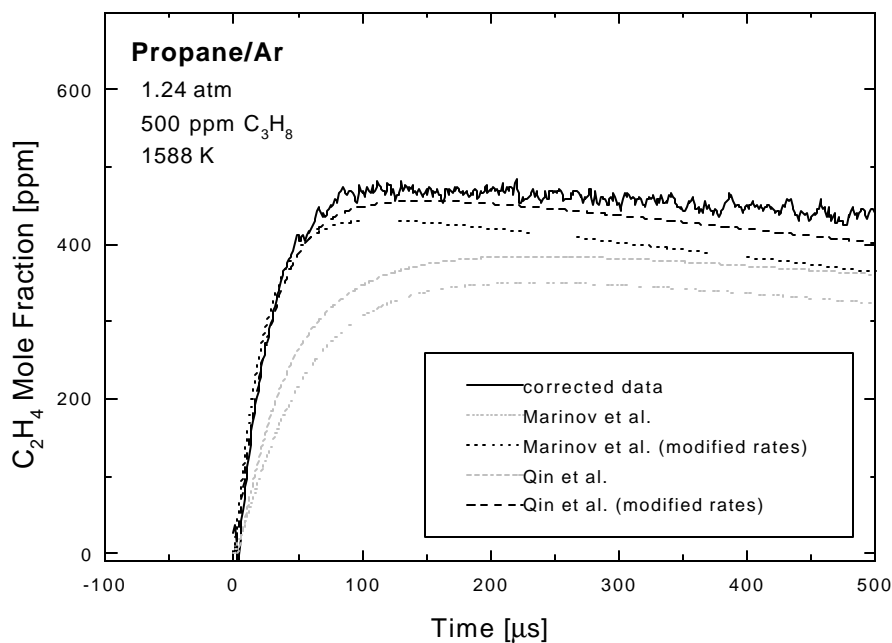
Fig. 8.2 Effect of modifications to the propane mechanisms on the predicted ethylene traces.

To further determine the effect of the modifications presented here to the propane mechanisms, both modified reaction mechanisms were compared to the propane ignition time measurements of the current study (see Fig. 8.3). The modifications to the Marinov et al. model are shown to result in about an 8% increase in the predicted ignition time. Thus, the effect of increasing reaction R 8.1, which shortens ignition delay, is more than offset by the increase in reaction R 8.2, which lengthens the ignition delay due to the increased rate of H-atom consumption by the fuel, thus hindering the $H + O_2$ branching reaction. Hence, the modifications to the Marinov et al. model have very little effect on the predicted ignition times. The modifications to the Qin et al. mechanism are shown to decrease the predicted ignition delay of propane by about 20%. Therefore, the modifications to the Qin et al. model do not result in an improved prediction of the propane ignition delay. Additional improvements to the models would likely require modifications to a number of key oxidizing reactions, and therefore time-history measurements of additional species are needed to guide further refinements to the detailed models.
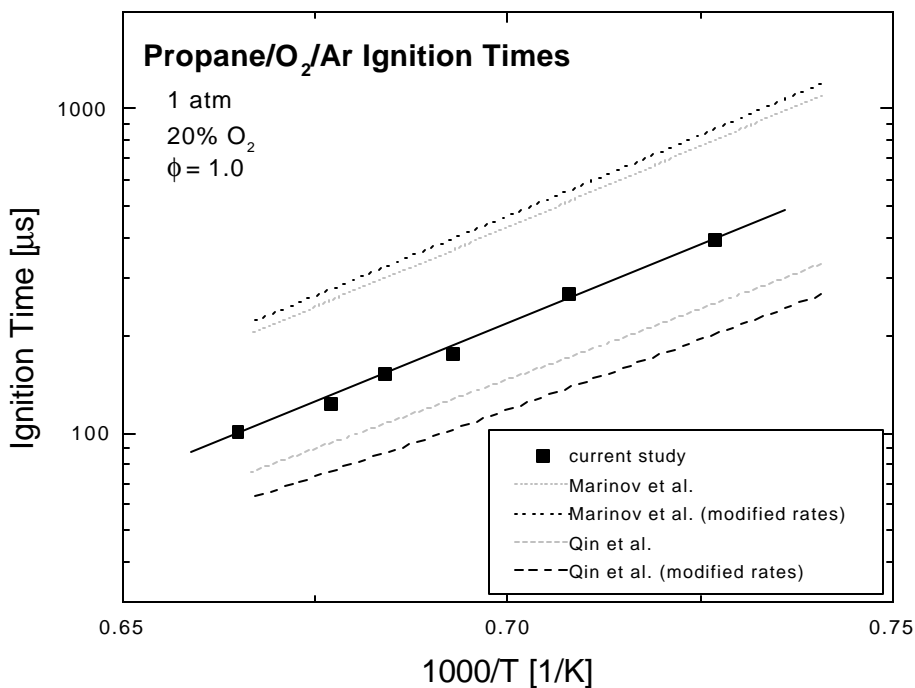
Fig. 8.3 Effect of modifications to the propane mechanisms on the predicted ignition times.

8.2 *n*-BUTANE

8.2.1 Analysis of Mechanism

A sensitivity analysis was performed on the Marinov et al. *n*-butane mechanism to determine which reactions are most influential on the predicted formation and removal of ethylene. The removal rate of ethylene was found to be sensitive to a number of reactions, and therefore, similar to propane, the focus here will be on the ethylene trace at early times. The formation of ethylene is predicted to occur predominantly via the following two reactions.

$$n\text{-}C_4H_{10} \rightarrow n\text{-}C_3H_7 + CH_3 \qquad \text{[R 8.9]}$$

$$n\text{-}C_4H_{10} \rightarrow C_2H_5 + C_2H_5 \qquad \text{[R 8.10]}$$
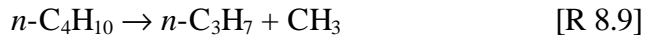
The rate expressions for reactions R 8.9 and R 8.10 utilized in the Marinov et al. model are those suggested by Pitz et al. [59], in which a C_4 mechanism was developed based on species measurements from the exhaust of a piton-cylinder engine.

8.2.2 Modifications to Mechanism

As shown in Fig. 7.6, reaction R 8.10 will lead to twice the amount of ethylene relative to reaction R 8.9. Therefore, to raise the predicted ethylene yield to the measured value, the branching ratio of reaction R 8.9 to R 8.10 was decreased by lowering the rate of reaction R 8.9 by a factor of two and raising that of reaction R 8.10 by a factor of two. Furthermore, to remain consistent with the previous analysis for propane, all modifications to the Marinov et al. propane mechanism presented above were similarly applied here. However, these adjustments to the propane mechanism were found to have no effect on the predicted ethylene trace for the pyrolysis of *n*-butane.

The predicted ethylene time-history for the modified *n*-butane reaction mechanism is shown in Fig. 8.4. The modifications are shown to have a negligible effect on the rate of ethylene formation, and thus good agreement with the empirical ethylene trace is maintained. In

addition, the modified reaction mechanism is shown to more closely predict the maximum ethylene concentration measured in this study. However, the modified mechanism predicts a much faster rate of ethylene removal than measured experimentally, which is a trend that was similarly found for the modified propane mechanism (see Fig. 8.2). This increase in the ethylene removal rate is due to a more rapid production of H-atoms by the reaction $C_2H_5 \rightarrow C_2H_4 + H$, which follows from the increased rate of reaction R 8.10. That is, the higher H-atom concentration subsequently leads to a faster ethylene removal rate via reaction R 8.4. Simply reducing the rate of reaction R 8.9 however, holding reaction R 8.10 constant, resulted in only a very slight increase in the ethylene yield. Thus, adjusting the relative rates of reactions R 8.9 and R 8.10 did not enable an improved prediction of both the ethylene yield and the ethylene removal rate simultaneously. As discussed previously, the ethylene removal rate is predicted to be sensitive to a number of reactions, making it difficult to determine which reaction(s) should be adjusted to improve the agreement between model and experiment. In addition, adjustments to reactions R 8.9 and R 8.10 were found to have a negligible effect on the ignition delay of *n*-butane.
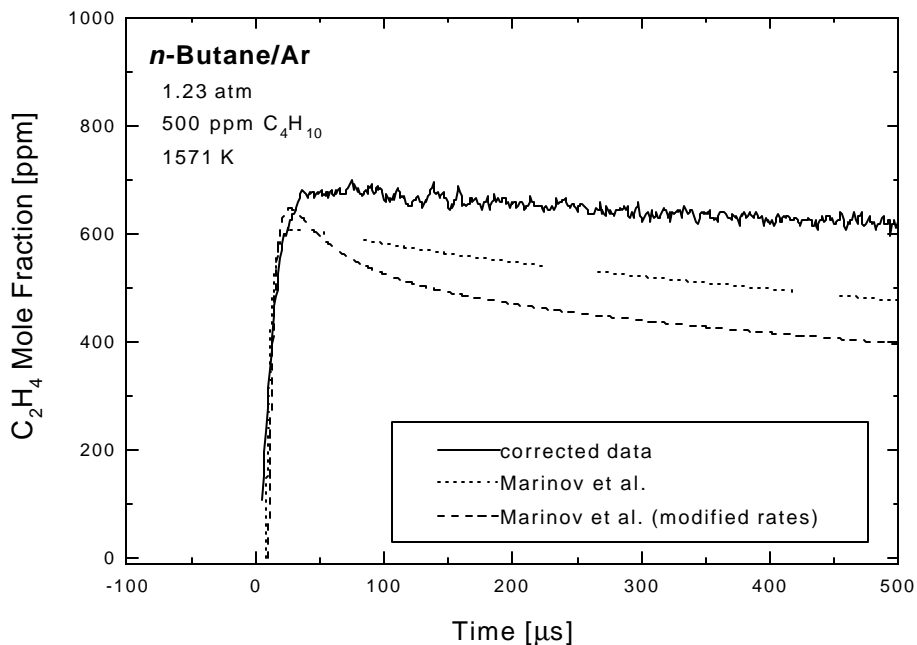
Fig. 8.4 Effect of modifications to the *n*-butane mechanism on the predicted ethylene trace.

112

8.3 *n*-HEPTANE

The three *n*-heptane models presented here exhibited marked differences for both the predicted ignition time values and ethylene time-histories. Therefore, a detailed analysis of these mechanisms is presented to provide further insight into the reasons for these differences. First, a brief discussion of each mechanism is presented.

8.3.1 Analysis of Mechanisms

The model of Held et al. [48] is a simplified high-temperature reaction mechanism developed specifically for *n*-heptane decomposition and oxidation. It contains 41 species and 266 reactions. The model has been compared to species measurements from a continuous flow reactor and jet-stirred reactor, shock tube ignition time measurements, and premixed, laminar flame speeds. The C_1-C_3 sub-mechanisms are largely taken from the reviews of Tsang et al. [60,61]. The method utilized to develop the *n*-heptane sub-mechanism, and that of the larger hydrocarbons species, is as follows.

The decomposition of *n*-heptane was assumed to occur primarily via H-atom abstraction. The Held et al. model includes abstraction reactions for six radical species.

$$n\text{-}C_7H_{16} + X \rightarrow C_7H_{15} + XH \qquad X = H, O, OH, HO_2, CH_3, C_3H_5 \qquad [R\ 8.11]$$
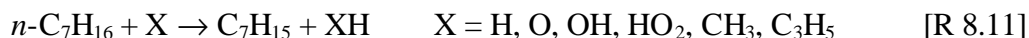
Individual rate constants are assigned to each specific H-atom site, with values estimated from the primary and secondary abstractions reactions of propane recommended by Tsang [57]. Furthermore, the A-factors of the abstraction reactions were adjusted to account for the number of H-atoms at each site. The resulting *n*-heptyl radicals are assumed to rapidly decompose into an olefin and a smaller alkyl radical, where each *n*-heptyl isomer is predicted to decompose into a different olefin-alkyl radical pair. Alkyl radicals larger than ethyl are assumed to similarly decompose into another olefin-alkyl pair. Since no other reactions channels are considered for the alkyl radicals, the Held et al. model employs a series of global reactions to

minimize the number of reactions considered. An example global reaction for H-atom abstraction is as follows.

$$n\text{-}C_7H_{16} + H \rightarrow H_2 + 1\text{-}C_5H_{10} + C_2H_5 \qquad [\text{R } 8.12]$$

This same methodology is also applied to the initial thermal decomposition of n-heptane, which initiates the reaction sequence. The mechanism includes a set of global pyrolysis reactions, in which the fuel is assumed to initially decompose into n-heptyl radicals and H-atoms. The following is an example initiation reaction.

$$n\text{-}C_7H_{16} \rightarrow H + 1\text{-}C_4H_8 + C_2H_4 + CH_3 \qquad [\text{R } 8.13]$$

The model of Lindstedt and Maurice [49] is a relatively comprehensive mechanism containing 109 species and 659 reactions, of which 21 species and 201 reactions are specific to the n-heptane sub-mechanism. This sub-mechanism was added to the aromatic and C_1-C_4 mechanism developed previously by Lindstedt and co-workers for premixed and diffusion flames [62,63]. The model has been validated using species measurements from counter-flow diffusion flames and jet-stirred reactors, and to premixed, laminar flame speeds.

The validation procedure employed by Lindstedt and Maurice revealed that it was necessary to include both H-atom abstraction and unimolecular decomposition reactions for n-heptane in order to accurately predict intermediate species profiles. Therefore, the Lindstedt and Maurice model does not employ the global reaction method utilized by Held et al., but rather includes elementary reactions for both the thermal decomposition and free radical attack of n-heptane. Furthermore, a contribution analysis of this model reveals that, under the conditions of the current study, the decomposition of n-heptane occurs almost entirely via fission of its C-C bonds. Therefore, the decomposition of n-heptyl has almost no effect on the predicted reaction sequence of the Lindstedt and Maurice model. This is in contrast to the Held

model, for which the decomposition of *n*-heptane was assumed to occur predominantly via the decomposition of *n*-heptyl radicals.

The model of Curran et al. [50] has been built up from smaller to larger hydrocarbons using a compilation of reaction sub-mechanisms. The model includes reaction schemes for both high- and low-temperature modeling, and contains over 500 species and more than 2400 reactions. Consumption of the fuel is accounted for by both unimolecular decomposition and H-atom abstraction. Rate constant expressions for unimolecular decomposition were estimated from the reverse reaction rates. Site-specific H-atom abstraction rate expressions were assumed to be equal to those of smaller hydrocarbons (e.g., propane). The mechanism was validated using species measurements from a continuous flow reactor and a jet-stirred reactor, and ignition time measurements obtained from shock tubes and rapid compression machines.

8.3.2 Comparison of Mechanisms

One the most striking differences among the three *n*-heptane models is the variation in the predicted ethylene removal rate. Both the Curran et al. and Held et al. models were found to predict a very fast removal rate for ethylene (although very different ethylene yields), while the model of Lindstedt and Maurice predicts a much slower rate. A sensitivity analysis of all three models showed the removal rate of ethylene for the pyrolysis of *n*-heptane is largely controlled by the following reaction.

$$C_2H_4 + H \rightarrow C_2H_3 + H_2 \qquad\qquad [R\ 8.4]$$

However, the rate expression for this reaction is identical in both the Lindstedt and Maurice and Held et al. models. Furthermore, for the current conditions, the rate expression of reaction R 8.4 utilized in the Curran et al. model yields a value that is only about a factor of 1.5 higher than that of the other two models. Therefore, the slow rate of ethylene removal predicted by the Lindstedt and Maurice model, relative to the other two models, is attributable to differences in the predicted H-atom concentrations, which are shown in Fig. 8.5.
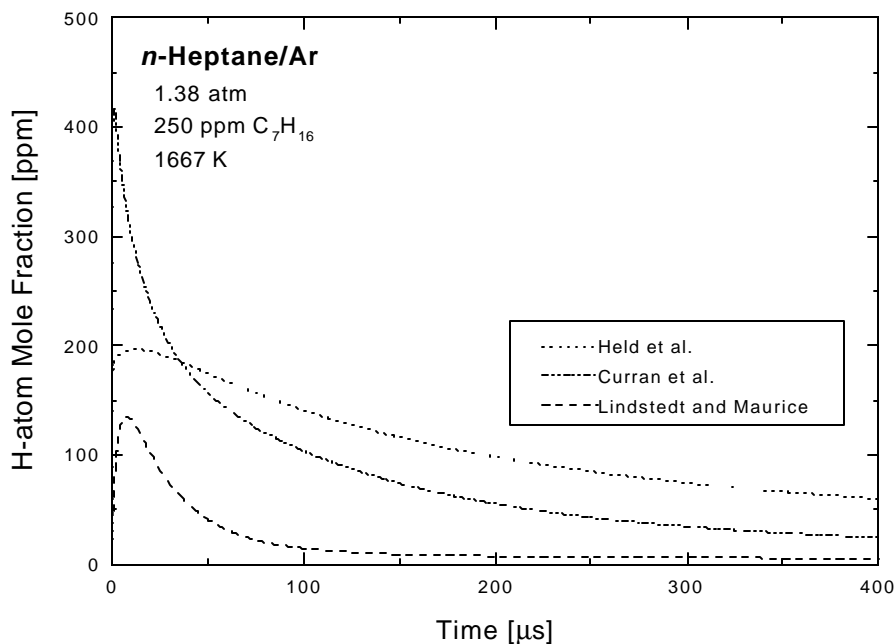
Fig. 8.5 Comparison of the predicted temporal variation of H-atom.

The results presented in Fig. 8.5 reveal that there are a number of differences among the three *n*-heptane models regarding the predicted H-atom time-history. For example, all three models are shown to predict very different values for the maximum H-atom mole fraction. These maximum values are approximately 140 ppm, 200 ppm, and 420 ppm for the Lindstedt and Maurice, Held et al., and Curran et al. models, respectively. Furthermore, the Lindstedt and Maurice and Curran et al. models both predict a relatively rapid decrease in the H-atom concentration, while the Held et al. model predicts a much slower H-atom removal rate. Therefore, although all three mechanisms utilize a rate expression for reaction R 8.4 that results in nominally the same value, the predicted ethylene traces are found to vary significantly due to the wide variations in the predicted H-atom concentration.

From the H-atom traces shown in Fig. 8.5, the variation of the ethylene time-histories among the three models is easily explained. The slow ethylene removal rate predicted by the Lindstedt and Maurice model is a direct result of the low H-atom concentration relative to the other two models. Furthermore, although both the Lindstedt and Maurice and Curran et al. models predict a similarly fast H-atom removal rate, the Curran et al. model predicts a much higher initial value for the H-atom concentration. Therefore, the high H-atom concentration predicted by the Curran et al. model results in a much faster ethylene removal rate. The Held et al. model, in contrast, predicts a much slower H-atom removal rate. Therefore, although the maximum H-atom concentration predicted by the Held et al. model is much lower than that of the Curran et al. model, both models predicts a similar ethylene removal rate due to the differences in the predicted H-atom removal rate.

Further analysis of the *n*-heptane mechanisms revealed that the lower H-atom removal rate predicted by the Held et al. model is due to the following reaction.

$$C_2H_3 + M \rightarrow C_2H_2 + H + M \qquad\qquad [R\ 8.14]$$

That is, reaction R 8.14 was shown to be an effective source of H-atoms for the Held et al. model, thus acting to replenish the H-atom pool as it is consumed by reaction R 8.4. However, the Lindstedt and Maurice and Curran et al. models clearly do not predict reaction R 8.14 to contribute significantly to the formation of H-atoms after the initial radical pool is established, which is evident from the rapid H-atom removal rate predicted by these two models. Very few empirical studies have attempted to measure the reaction rate of R 8.14 at high-temperatures, and thus suggested values are largely based on measurements obtained near room-temperature [60]. As such, the rate expression for reaction R. 8.14 is relatively uncertain at the high temperatures of this study, which may account for the discrepancies observed among the three *n*-heptane mechanisms regarding the effect of this reaction.

In addition to differences in the ethylene removal rate, all three models are also shown to predict different values for the ethylene yield of n-heptane. The Held et al. model is shown to predict a slightly higher ethylene yield than that of Lindstedt and Maurice over a majority of the temperature range studied, while the model of Curran et al. predicts a significantly lower value than the other two models (see Fig. 7.8). To determine the reason for this discrepancy, the ethylene formation and removal reactions of each mechanism were compared.

The previous analysis of propane and n-butane, presented in Sections 8.1 and 8.2, revealed that the predicted ethylene time-histories for both of these fuels are sensitive to the ethylene removal rate, which is largely controlled by reaction R 8.4. However, although the value for this rate expression has been found to be a factor of 1.5 higher for the Curran et al. model relative to the other two mechanisms, lowering this rate by a factor of 1.5 was found to have only a minor effect on the predicted ethylene yield for the Curran et al. model.

An analysis of the decomposition products predicted by each n-heptane model revealed an important discrepancy that may explain the observed differences in their predicted ethylene yields. At early times, during which the ethylene concentration is near its maximum, (i.e., t < 20 µs) the Held et al. mechanism predicts that the n-heptane is almost entirely converted to ethylene and methyl radicals, and that the propene concentration is negligible (< 5 ppm). However, the Lindstedt and Maurice model predicts a propene concentration of approximately 30-50 ppm for the time at which the ethylene reaches its maximum value, and the Curran et al. model predicts a propene concentration well over 100 ppm. Therefore, the variation in the ethylene yields among the three models is largely due to differences in the predicted fuel decomposition channels that lead to ethylene and propene.

8.4 n-DECANE

For completeness, the Lindstedt and Maurice n-decane mechanism [52] was analyzed to determine the main decomposition channels for this fuel. As discussed previously, this

mechanism is essentially identical to the Lindstedt and Maurice *n*-heptane mechanism [49] described in detail in the previous section, with the addition of a set of *n*-decane decomposition reactions, and thus a detailed analysis of the Lindstedt and Maurice *n*-decane mechanism is not given.

A contribution analysis of the Lindstedt and Maurice *n*-decane mechanism revealed the following three decomposition channels dominate in the pyrolysis of *n*-decane at the temperatures of the current study.

$$C_{10}H_{22} \rightarrow n\text{-}C_7H_{15} + n\text{-}C_3H_7 \qquad\qquad [R\ 8.15]$$

$$C_{10}H_{22} \rightarrow n\text{-}C_6H_{13} + n\text{-}C_4H_9 \qquad\qquad [R\ 8.16]$$

$$C_{10}H_{22} \rightarrow n\text{-}C_5H_{11} + n\text{-}C_5H_{11} \qquad\qquad [R\ 8.17]$$
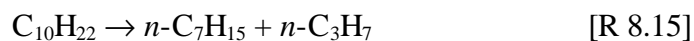
Therefore, similar to the Lindstedt and Maurice *n*-heptane mechanism, the thermal decomposition of *n*-decane is predicted to occur mainly via the breaking of C-C bonds, rather than by H-atom abstraction reactions, at the condition of the current study.

Chapter 9

Conclusions

This study presents the results of ignition time measurements for propane, n-butane, n-heptane, n-decane, and ethylene over a wide range of conditions. Correlations have been presented for the ignition times of n-butane and n-heptane, which reveal the marked similarities in the ignition time sensitivities between these two fuels. In addition, a single expression is presented which accurately correlates the ignition delay times of the stoichiometric n-alkane mixtures studied here. The ignition delay of ethylene was found to be largely unrelated to that of the n-alkanes. This is likely a result of the pressure sensitivity exhibited by the unimolecular decomposition rate of ethylene.

Comparisons of the current ignition time data to previous studies have further validated the empirical correlations over a wider range of conditions, and suggest the feasibility of using ignition time sensitivities to directly compare measurements obtained at different conditions. The ignition time sensitivities measured in the current study are in reasonably good agreement with those found previously, although correlations are not developed for a number of studies due to insufficient experimental data. The current work is also compared to a variety of detailed chemical models, in which both the absolute ignition time values, and the predicted ignition time sensitivities to relevant parameters are analyzed, thereby providing for a more rigorous comparison the models.

Measurements obtained for the pyrolysis of propane, n-butane, n-heptane, and n-decane indicate that ethylene is a major decomposition product of the n-alkanes at high temperature (> 1500 K). Furthermore, the n-alkanes have been shown to produce an ethylene

yield that increases with increasing fuel size, and is essentially constant over the temperature range of 1500-2100 K. Contribution and sensitivity analyses of the detailed chemical models has led to a more detailed understanding of the pathways by which the n-alkanes decompose, and provided insight into the important reaction rates that control the formation of ethylene. In addition, the decomposition pathways by which the n-alkanes are predicted to pyrolyze have been shown to have a significant effect on the ethylene yields predicted by the detailed models.

The results presented offer a number of suggestions for potential future studies. The similarities in the ignition time behavior among the n-alkanes suggest the feasibility of conducting a similar investigation on another class of fuels (e.g., monocyclic aromatics, cycloalkanes). Also, additional n-alkane measurements may help to further validate the ignition time sensitivities over a wider range of conditions and fuel sizes. This work would also provide for a more thorough validation of detailed n-alkane mechanisms.

In addition, quantitative measurements of additional select species (e.g., methyl, H atom) are needed to further the development and refinement of detailed chemical mechanisms. As shown in the current study, quantitative measurements of the temporal variation of ethylene during fuel pyrolysis have enabled a much more detailed analysis of the chemical reaction sequence for the n-alkanes. Therefore, similar measurements of additional fuel decomposition products (e.g., propene, acetylene) are also strongly recommended.

Appendix A

Hydrocarbon Classifications

This section describes two methods that are commonly utilized to classify hydrocarbons. In organic chemistry, hydrocarbons are classified according to their atomic composition and structure, while in petroleum refining, hydrocarbons are classified by the individual fractions or "cuts" that are produced during the distillation process. A review of past works has found numerous examples in which each classification system was employed, and thus it is advantageous to be familiar with the basic classifications of each system.

A.1 ORGANIC CHEMISTRY

This section provides a brief description of some of the more common classes of hydrocarbons relevant to combustion, and therefore is not inclusive of all hydrocarbon classes within organic chemistry.

A.1.1 Alkanes

Alkanes, also referred to as paraffins, contain only single bonds, and have the general formula C_nH_{2n+2}. Alkanes are often referred to as saturated hydrocarbons since each carbon atom is bonded to the maximum number of hydrogen atoms, and thus the molecule is "saturated" with hydrogen. Alkanes composed of more than three carbon atoms are isomeric, and therefore are subdivided into normal and branched compounds. Normal alkanes, or straight-chain alkanes, contain carbon atoms that are linked in one continuous chain, and have the general formula $CH_3(CH_2)_{n-2}CH_3$. The name of each normal alkane is based on the number of carbon atoms in the molecular chain, and is preceded by the prefix *n-* to designate it as a normal compound.
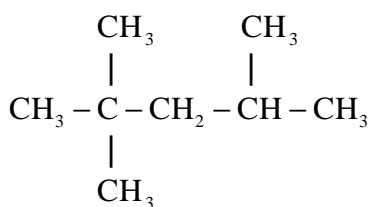
$$CH_3 - CH_2 - CH_2 - CH_3$$

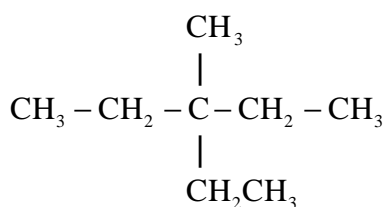$$CH_3 - CH_2 - CH_2 - CH_2 - CH_2 - CH_2 - CH_3$$
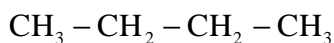
n-butane

n-heptane

Branched alkanes do not contain a single chain of carbon atoms, but instead have one or more side carbon chains. The longest continuous chain of carbon atoms present in the molecule, referred to as the base chain, determines the name of the compound. Each carbon atom in the base chain is sequentially numbered, beginning at the end of the chain that is closest to the first side chain. If two side chains are equidistant from each end, the carbon atoms are numbered such that the sum of the branch locations is minimized. The name of each branched alkane begins with a number(s) that corresponds to the location of each side chain. The number is listed twice if two side chains are attached to the same carbon atom. This number is then immediately followed by the name of the side chains in the molecule (e.g., methyl, ethyl). If the compound contains more than one identical side chain, a prefix (e.g., *di-*, *tri-*, *tetra-*) is added to specify their quantity. There are numerous additional IUPAC rules for naming branched alkanes, however the rules presented here are sufficient to name a majority of the more common branched alkanes.

$$
\begin{array}{c}
\quad\; CH_3 \qquad\; CH_3 \\
\quad\; | \qquad\qquad | \\
CH_3 - C - CH_2 - CH - CH_3 \\
\quad\; | \\
\quad\; CH_3
\end{array}
$$

$$
\begin{array}{c}
\qquad CH_3 \\
\qquad | \\
CH_3 - CH_2 - C - CH_2 - CH_3 \\
\qquad | \\
\qquad CH_2CH_3
\end{array}
$$

2,2,4-trimethylpentane

3-ethyl-3-methylpentane

A.1.2 Alkenes and Alkynes

Alkenes, also known as olefins, are hydrocarbons that contain a C=C double bond. They are also referred to as unsaturated hydrocarbons since breaking of one of the C=C double bonds would permit the addition of two more hydrogen atoms. Two different nomenclatures are often utilized to name alkenes - common names, and the International Union of Pure and Applied Chemistry (IUPAC) system. Common names are applied to relatively simple

compounds. This naming scheme is based on the total number of carbon atoms in the molecule, similar to the *n*-alkanes, and end with the suffix –*ylene*. Branched alkenes are distinguished from normal alkenes by the prefix *iso-*.

$$CH_2 = CH_2 \qquad\qquad CH_3CH = CH_2 \qquad\qquad CH_3 - \underset{\underset{CH_3}{|}}{C} = CH_2$$

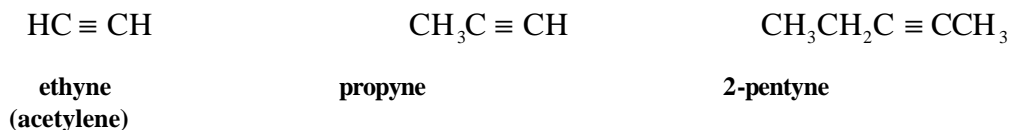**ethylene**   **propylene**   **isobutylene**
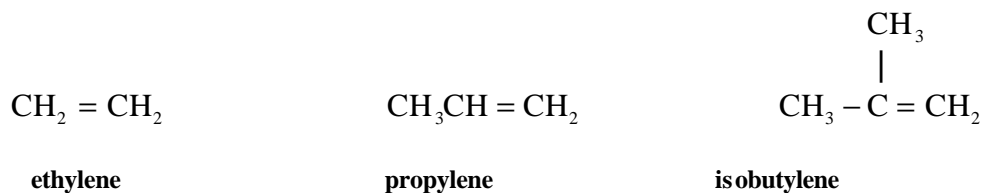
In the IUPAC system, the base chain of the alkene is the longest continuous chain that contains the C=C double bond. The name of the molecule is derived from the number of carbon atoms in the base chain, and ends in the suffix -*ene*. The carbon atoms are numbered sequentially from the chain end that is closest to the C=C double bond, and the name of the alkene is preceded by a number that specifies the position of the double bond.

$$CH_2 = CH_2 \qquad\qquad\qquad CH_3 - CH = CH - CH_2 - CH_3$$

ethene   **2-pentene**

Molecules that contain two C=C double bonds are referred to as dienes, and end in the suffix -*adiene*.

$$CH_2 = CH - CH = CH_2$$

1,3-butadiene

Alkynes, also referred to as acetylenes, contain a C≡C triple bond, and end in the suffix –*yne*. The position of the triple bond is specified in a similar manner as the alkenes.

$$HC \equiv CH \qquad\qquad CH_3C \equiv CH \qquad\qquad CH_3CH_2C \equiv CCH_3$$

ethyne   **propyne**   **2-pentyne**
**(acetylene)**

A.1.3 Aromatics

Aromatics contain one of more benzene rings, and are therefore relatively stable due to the resonance energy associated with this ring structure. Aromatics that contain one benzene ring are referred to as monocyclic, and those that are composed of multiple benzene rings are polycyclic.

Monocyclic aromatics are named according to the type and number of side chains that are connected to the benzene ring. If only one side chain is present, and this chain does not contain a functional carbon atom (e.g., C-OH, C=O) the compound is referred to as a monosubstituted benzene. These hydrocarbons are named by combining the name of the side chain with the root *benzene*, however a number of monosubstituted benzenes have common names that are much more widely recognized (e.g., methylbenzene is more commonly known as toluene).
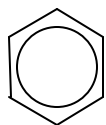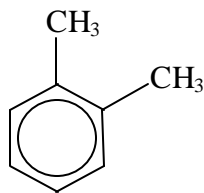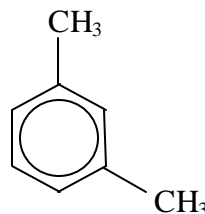

benzene
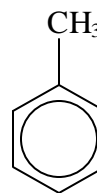
methylbenzene
(toluene)

When two side chains are attached to the benzene ring, and neither chain contains a functional group, the compound is referred to as a disubstituted benzene. The name of a disubstituted benzene is preceded by a number that represents the relative location of each side chain along the benzene ring. If the two or more identical side chains are present, a prefix is used (e.g., *di-*, *tri-*) to specify the number of similar side chains. Many disubstituted benzenes have common names, such as dimethylbenzene, which is more commonly referred to as xylene. Common names employ the prefixes *ortho-*, *meta-*, and *para-* to represent the 1,2, 1,3, and 1,4 side chain positions, respectively.

1,2-dimethylbenzene
(para xylene)

**1,3-dimethylbenzene**
(meta xylene)

1,4-dimethylbenzene
(ortho xylene)

Polycyclic aromatics are subdivided according to the number and relative orientation of their benzene rings. Two of the more common polycyclic aromatics are naphthalenes, which contain two fused benzene rings, and anthracenes, which contain three benzene rings that are fused in a straight chain.
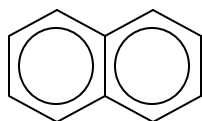
naphthalene
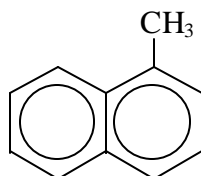
1-methylnaphthalene
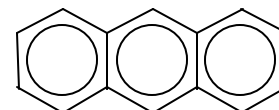
anthracene

A.1.4 Alicyclics

Alicyclics, or cyclics, are hydrocarbons that contain a closed ring of carbon atoms. They are also referred to as naphthenes by the petroleum refining industry. While aromatics may technically be considered cyclic compounds, the term "cyclic" is usually used in reference to closed ring hydrocarbons that do not contain the benzene ring structure. While there are many different types of cyclic compounds, only the most common types will be discussed.

Cycloalkanes contain only single bonds, and are named according to a similar set of rules as those employed for the *n*-alkanes. The name of a cycloalkane is based on the number

of carbon atoms in its ring, and is given the prefix *cyclo-*. The most abundant cycloalkanes are those with five, six, and seven carbon atoms in their ring structure since these compounds are more stable due to the lower strain energy of their rings. Cyclics that contain one or two C=C double bond are referred to as cycloalkenes and cycloalkadienes, respectively.
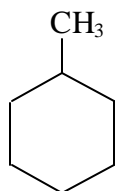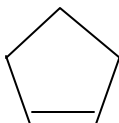
methylcyclohexane   **cyclopentene**   **cyclopentadiene**
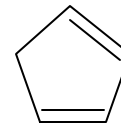
Hydrocarbons that contain two rings are referred to as bicyclic. When the two rings share adjacent carbons atoms, the molecule is a fused-ring hydrocarbon (e.g., decalin), and for two rings that share nonadjacent atoms, the molecule is a bridged-ring hydrocarbon (e.g., norbornane). The name of a bicyclic hydrocarbon is based on the total number of carbon atoms in the molecule, and is given the prefix *bicyclo-*. The carbon atoms that are shared between the two rings are referred to as bridgehead carbon atoms and are used to determine the bridges in the molecule, where a bridge is defined as any connection between the bridgehead carbon atoms. The length of each bridge, beginning with the largest, is specified in brackets after the prefix *bicyclo-*.
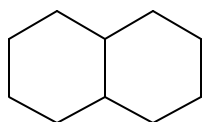
bicyclo[4.4.0]decane   **bicyclo[2.2.1]heptane**
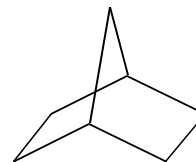
(decalin)   **(norbornane)**

A.2 PETROLEUM REFINING

Crude oil, or petroleum, is composed of thousands of different hydrocarbon species, and is used to make a variety of products. These products are produced during the distillation process, which involves heating the petroleum to a very high temperature, usually around 500-600 °F, thereby causing a large fraction of the petroleum to evaporate. The hydrocarbon vapors then cool and condense as they rise up through a distillation tower, with the lighter, more volatile hydrocarbons condensing near the top of the distillation tower and the heavier hydrocarbons condensing near the bottom. The distillation tower contains a series of vertically spaced distillation trays that are used to collect the condensed vapor, and thus each tray collects a different "cut" or "fraction" of the petroleum. Since the vertical spacing and number of trays utilized in the distillation process is variable, each refinery may have slightly different classes of petroleum fractions depending on the exact temperature range from which the fraction is cut. Therefore, only the more general petroleum fraction classifications will be discussed here.

A.2.1 Gases

The gaseous fraction is composed of the lowest boiling point compounds, and is composed of hydrocarbons that are in the gas-phase at ambient pressure and temperature. A majority of this fraction is comprised of the C_1-C_4 alkanes, and to a smaller extent the C_1-C_4 alkenes. Methane and ethane are commonly used as a refinery fuel or a feedstock for hydrogen production. These two gases are also the predominant hydrocarbons present in natural gas, which contains nominally 85-90% methane and 5-10% ethane. Propane is typically used as a refinery fuel or is sold as liquefied petroleum gas (LPG). The butanes, while also used to make LPG, are largely utilized in the production of gasoline to raise the vapor pressure of the fuel to an appropriate level.

A.2.2 Naphtha

The naphtha fraction has a boiling point typically between 300-400 °F, and is composed of mainly C_5-C_{12} hydrocarbons. It is a relatively wide cut, and thus it is often subdivided into light straight-run naphtha and heavy straight-run naphtha. The lighter naphtha cut is used to make solvents such as turpentine and paint thinner. In the past, this was one of the more predominant products produced from naphtha. However, today the main product produced from naphtha is gasoline, which is often considered its own fraction.

Due to the stringent specifications for gasoline, the straight-run naphtha fraction must be further processed before it can be sold as gasoline. Two of the more important specifications are the Reid vapor pressure (RVP) and the octane number (ON). The RVP is approximately the vapor pressure of the gasoline at 100 °F, and is varied from nominally 7 psia in the summer to 13.5 psia in the winter. The RVP is an indication of the volatility of the gasoline, and is typically controlled by adjusting the amount of *n*-butane added to the fuel. The octane number is a measure of the resilience of a gasoline to self-ignition or engine "knock." It is measured relative to a mixture of *n*-heptane and *iso*-octane, which have an octane number of 0 and 100, respectively, by definition. The octane level of gasoline is raised via a reformulation process, in which low-octane *n*-alkanes are converted into high-octane aromatics, however, restrictions limit the amount of aromatics that may be present in gasoline.

A.2.3 Kerosene

The kerosene fraction is cut from nominally 350-550 °F, and contains mainly C_{12}-C_{16} hydrocarbons. In the past, kerosene was largely utilized for domestic heating and lighting, but today it is often referred to as the jet fuel fraction since its main use is for the production of jet fuels such as Jet A or JP-5. In addition, jet fuels may also be manufactured from a single chemical species, for which they are commonly referred to as high-energy-density fuels.

Distillate jet fuels, such as Jet A, JP-4 and JP-5, are made directly from the distillation process. The chemical properties of these distillate jet fuels are adjusted by tailoring the boiling

range from which the fuel is cut. For example, lowering the initial boiling point of the fraction increases its vapor pressure, smoke point, and hydrogen content, and decreases its density, flashpoint, freezing point and viscosity. While distillates are manufactured to meet certain specifications, such as maximum final boiling point, maximum freezing point, maximum aromatic content, etc., a given jet fuel will have slightly different properties and compositions depending on the manufacturing process and the properties of the original petroleum. Table A.1 lists some of the properties of a few common distillate jet fuels.

Table A.1 Properties of select distillate jet fuels[*].

Fuel	Heating value [BTU/lb]	Specific gravity	H/C ratio	Boiling range [°F]	Utility
Jet-A	18,600	0.80	1.96	400-571	Commercial jet fuel
JP-4	18,700	0.76	2.00	140-517	U.S. Air Force primary jet fuel (1951-1995)
JP-5	18,500	0.81	1.92	360-495	U.S. Navy primary jet fuel
JP-7	18,875	0.79	2.07	370-480	SR-71 jet fuel
JP-8	18,550	0.81	1.91	330-510	U.S. Air Force primary jet fuel (1995-present)

properties listed here are approximate values; actual values may vary depending on the specific refining process

To minimize the volume requirement for fuel storage, considerable research has been conducted in an attempt to produce jet fuels that have a relatively high energy-density. High energy-density jet fuels are chemically specific compounds that may be composed of a single molecular species, or a blend of a few specific hydrocarbon species. For example JP-10 is the pure hydrocarbon tetrahydrodi(cyclopentadiene), whereas JP-9 is a blend of methylcyclohexane (MCH), JP-10, and RJ-5. Compared to distillate jet fuels, high energy-density jet fuels have much higher heating values per unit volume, higher specific gravities, and lower hydrogen-to-carbon ratios. The properties of a few select high energy-density jet fuels are presented in Table A.2.

Table A.2 Properties of select high energy-density jet fuels.

Fuel	Heating value [BTU/lb]	Specific gravity	H/C ratio	Composition	Utility
JP-9	18,100	0.94	1.54	10% MCH, 70% JP-10, 20% RJ-5	Air Force air-launched cruise-missile fuel
JP-10	18,100	0.94	1.61	tetrahydrodi (cyclopentadiene)	Pulse-detonation engine fuel
RJ-4	17,850	0.94	1.67	tetrahydrodi (methylcyclopentadiene)	Navy Tomahawk and Talos missiles
RJ-5	17,860	1.08	1.28	hydrogenated dimers of norbornadiene	Blending agent used to fuel heating value

The energy-density of a fuel is largely based on its chemical structure. For example, due to their compact molecular structure, bridge-ring hydrocarbons have a relatively high energy-density. One of the simplest bridge-ring structures is norbornane, also refered to as bicyclo[2.2.1]heptane. While norbornane itself is not used as a jet fuel, its chemical structure provides the basic building block upon which a number of high energy-density fuels are based.
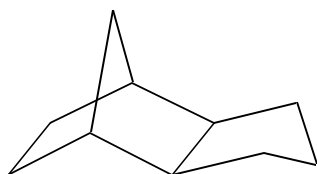
exo-tetrahydrodi(cyclopentadiene)
(JP-10)

A.2.4 Fuel Oil

Fuel oil is a relatively wide cut that boils in the range of 500-800 °F, and is therefore subdivided into a number of different classes. Fuel oils may also be subdivided into classes that

are more indicative of their use, such as diesel fuel and domestic heating fuel. Fuel oils No. 1 and No. 2 are primarily utilized to make light and heavy automotive diesel fuels, respectively. Fuel oil No. 2 is also commonly referred to as domestic heating oil due to its historical use in residential heating. Fuel oil No. 4 is a very heavy diesel fuel that is often used to power railroad engines, and fuel oil No. 6, which is one of the heaviest fuel oils, is used to power ships, for which it is more commonly referred to as bunker oil.

Automotive diesel fuels are made from the lightest cut of the fuel oil fraction, and are composed of primarily alkanes, aromatics, and cycloalkanes. One important specification of diesel fuel is its cetane number, which indicates its propensity to autoignite, and thus is inversely related to its octane number. The cetane number of a diesel fuel is based its autoignition quality relative to a mixture of n-hexadecane and 2,2,4,4,6,8,8-heptamethylnonane, which have a cetane number of 100 and 15, respectively, by definition.

Appendix B

Ignition Time Data

B.1 Propane/O₂/Ar

Temperature [K]	Pressure [atm]	Propane [%]	O$_2$ [%]	f	Ignition Time [ms]
1376	1.19	4.0	20	1.0	357
1461	1.15	4.0	20	1.0	140
1413	1.16	4.0	20	1.0	246
1477	1.12	4.0	20	1.0	115
1444	1.26	4.0	20	1.0	152
1504	1.14	4.0	20	1.0	93

B.2 *n*-Butane/O₂/Ar

Temperature [K]	Pressure [atm]	*n*-Butane [%]	O₂ [%]	f	Ignition Time [ms]
1447	1.14	1.0	6.5	1.0	244
1409	1.17	1.0	6.5	1.0	390
1483	1.32	1.0	6.5	1.0	161
1405	1.19	1.0	6.5	1.0	415
1478	1.20	1.0	6.5	1.0	171
1405	1.18	1.0	6.5	1.0	420
1407	1.99	1.0	6.5	1.0	297
1400	2.03	1.0	6.5	1.0	335
1445	2.02	1.0	6.5	1.0	186
1454	2.00	1.0	6.5	1.0	170
1415	3.80	1.0	6.5	1.0	189
1399	3.81	1.0	6.5	1.0	243
1433	3.75	1.0	6.5	1.0	151
1468	1.97	1.0	6.5	1.0	150
1499	1.14	1.0	6.5	1.0	151
1505	1.12	1.0	6.5	1.0	140
1557	1.13	1.0	6.5	1.0	87
1561	1.17	0.5	3.25	1.0	131
1513	1.18	0.5	3.25	1.0	186
1478	1.20	0.5	3.25	1.0	275
1532	1.33	0.5	3.25	1.0	156
1546	1.37	0.5	3.25	1.0	136
1433	1.27	0.5	3.25	1.0	475
1432	1.17	2.0	13	1.0	179
1490	1.19	2.0	13	1.0	100
1385	1.18	2.0	13	1.0	353
1434	1.15	2.0	13	1.0	180
1455	1.15	2.0	13	1.0	149
1517	1.16	2.0	13	1.0	83
1389	1.12	1.0	13	0.5	204
1422	1.08	1.0	13	0.5	131

Temperature [K]	Pressure [atm]	*n*-Butane [%]	O$_2$ [%]	f	Ignition Time [ms]
1385	1.11	1.0	13	0.5	206
1412	1.11	1.0	13	0.5	149

B.2 *n*-Butane/O$_2$/Ar (continued)

Temperature [K]	Pressure [atm]	*n*-Butane [%]	O$_2$ [%]	f	Ignition Time [ms]
1453	1.07	1.0	13	0.5	96
1352	1.14	1.0	13	0.5	307
1666	1.03	1.0	3.25	2.0	177
1627	1.06	1.0	3.25	2.0	220
1541	1.07	1.0	3.25	2.0	441
1734	1.08	1.0	3.25	2.0	105
1618	1.13	1.0	3.25	2.0	218
1577	1.13	1.0	3.25	2.0	304

B.3 *n*-Heptane/O₂/Ar

Temperature [K]	Pressure [atm]	*n*-Heptane [%]	O₂ [%]	f	Ignition Time [ms]
1446	1.15	0.4	4.8	0.9	234
1381	1.18	0.4	4.8	0.9	488
1491	1.23	0.4	4.8	0.9	137
1438	1.22	0.4	4.8	0.9	238
1492	1.22	0.36	4.4	0.9	141
1501	1.25	0.36	4.4	0.9	125
1476	1.25	0.36	4.4	0.9	163
1486	1.23	0.4	4.4	1.0	159
1458	1.27	0.4	4.4	1.0	208
1428	1.27	0.4	4.4	1.0	296
1455	1.20	0.4	8.8	0.5	86
1413	1.32	0.4	8.8	0.5	121
1347	1.30	0.4	8.8	0.5	286
1676	1.22	0.4	2.2	2.0	147
1529	1.26	0.4	2.2	2.0	442
1619	1.22	0.4	2.2	2.0	210
1396	1.23	0.4	8.8	0.5	161
1347	1.29	0.4	8.8	0.5	308
1345	1.34	0.4	8.8	0.5	305
1432	1.21	0.4	8.8	0.5	110
1347	1.22	0.4	8.8	0.5	323
1455	2.13	0.4	4.4	1.0	165
1384	2.12	0.4	4.4	1.0	403
1434	2.15	0.4	4.4	1.0	205
1478	2.08	0.4	4.4	1.0	131
1503	2.06	0.4	4.4	1.0	100
1412	2.14	0.4	4.4	1.0	265
1476	4.03	0.4	4.4	1.0	90
1420	4.07	0.4	4.4	1.0	163

Temperature [K]	Pressure [atm]	n-Heptane [%]	O₂ [%]	f	Ignition Time [ms]
1394	4.22	0.4	4.4	1.0	227
1463	4.11	0.4	4.4	1.0	103
1413	4.16	0.4	4.4	1.0	183

B.3 *n*-Heptane/O₂/Ar (continued)

Temperature [K]	Pressure [atm]	*n*-Heptane [%]	O₂ [%]	f	Ignition Time [ms]
1378	1.15	0.8	8.8	1.0	385
1426	1.17	0.8	8.8	1.0	208
1335	1.30	1.2	13.2	1.0	466
1455	1.22	1.2	13.2	1.0	115
1421	1.19	1.2	13.2	1.0	163
1349	1.20	1.2	13.2	1.0	411
1409	1.27	1.2	13.2	1.0	179
1465	1.14	1.2	8.8	1.5	189
1461	1.23	1.2	8.8	1.5	189
1409	1.27	1.2	8.8	1.5	321
1411	1.29	1.2	8.8	1.5	311
1386	1.24	1.75	19.7	1.0	177
1329	1.19	1.75	19.7	1.0	382
1330	1.16	1.75	19.7	1.0	382
1501	2.08	0.2	2.2	1.0	150
1468	2.13	0.2	2.2	1.0	216
1432	2.15	0.2	2.2	1.0	345
1547	2.07	0.2	2.2	1.0	100
1375	5.68	0.4	4.4	1.0	271
1431	5.71	0.4	4.4	1.0	120
1400	5.63	0.4	4.4	1.0	190
1421	5.69	0.4	4.4	1.0	138
1372	5.57	0.4	4.4	1.0	279
1442	5.65	0.4	4.4	1.0	117
1419	5.41	0.4	4.4	1.0	158
1423	1.20	1.2	6.6	2.0	486
1516	1.21	1.2	6.6	2.0	205
1456	1.20	1.2	6.6	2.0	361

B.4 *n*-Decane/O$_2$/Ar

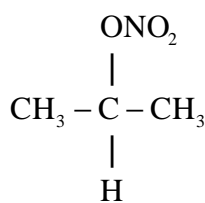| Temperature [K]	Pressure [atm]	*n*-Decane [%]	O$_2$ [%]	f	Ignition Time [ms]
1470	1.23	0.2	3.1	1.0	180
1445	1.24	0.2	3.1	1.0	290
1397	1.26	0.2	3.1	1.0	480
1456	1.24	0.2	3.1	1.0	235
1434	1.23	0.2	3.1	1.0	320
1516	1.22	0.2	3.1	1.0	124

B.5 Ethylene/O₂/Ar

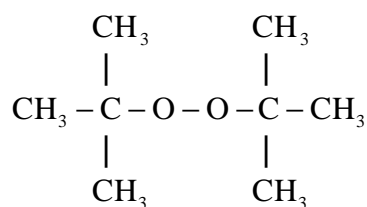| Temperature [K]	Pressure [atm]	Ethylene [%]	O$_2$ [%]	f	Ignition Time [ms]
1541	1.10	2.0	6.0	1.0	66
1465	1.14	2.0	6.0	1.0	93
1409	1.19	2.0	6.0	1.0	115
1316	1.23	2.0	6.0	1.0	200
1286	2.17	2.0	6.0	1.0	190
1329	2.13	2.0	6.0	1.0	132
1360	2.10	2.0	6.0	1.0	105
1395	2.08	2.0	6.0	1.0	84
1294	3.86	2.0	6.0	1.0	134
1253	3.98	2.0	6.0	1.0	221
1354	3.80	2.0	6.0	1.0	76
1314	1.29	4.0	12	1.0	99
1336	1.19	4.0	12	1.0	89
1311	1.35	4.0	12	1.0	101
1276	1.32	4.0	12	1.0	125
1280	1.33	4.0	12	1.0	121
1257	2.15	4.0	12	1.0	129
1283	2.11	4.0	12	1.0	101
1296	2.06	4.0	12	1.0	88
1477	1.29	1.0	3.0	1.0	148
1402	1.23	1.0	3.0	1.0	220
1517	1.26	1.0	3.0	1.0	120
1572	1.25	1.0	3.0	1.0	96
1347	2.14	1.0	3.0	1.0	248
1396	2.12	1.0	3.0	1.0	182
1450	2.11	1.0	3.0	1.0	123
1498	2.04	1.0	3.0	1.0	95

Appendix C

Effect of Additives on *n*-Heptane Ignition

The effect of fuel additives on the ignition delay of *n*-heptane was studied in the high-pressure shock tube (HPST) in order to simulate the low-temperature, high-pressure conditions that are typical for diesel engines. The parent fuel selected to this study was *n*-heptane, which is a good diesel fuel surrogate since its cetane number ($\approx$ 56) is comparable to that of most diesel fuels. The additives studied include isopropyl nitrate (IPN) and di-*tert*-butyl peroxide (DTBP), which have been used in the petroleum refining process to raise the cetane number of diesel fuels. Two additional additives - dimethyl ether (DME) and cyclopropyl acetylene (CPA) - were also studied to assess their potential as possible ignition-enhancers. These four additives are illustrated below.

$$CH_3 - \underset{\underset{H}{|}}{\overset{\overset{ONO_2}{|}}{C}} - CH_3$$

iso-**propyl nitrate**

$$CH_3 - \underset{\underset{CH_3}{|}}{\overset{\overset{CH_3}{|}}{C}} - O - O - \underset{\underset{CH_3}{|}}{\overset{\overset{CH_3}{|}}{C}} - CH_3$$

di-*tert*-butyl peroxide

$$CH_3 - O - CH_3$$

dimethyl ether

$$\triangleright - HC{\equiv}CH$$
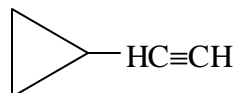
cyclopropyl acetylene

The ignition time definition employed in the HPST study was based on pressure measurements obtained by a pressure transducer that was mounted into the shock tube endplate. Thus, the endwall ignition time was measured directly, and the onset of ignition was based on the initial rise in pressure at the time of ignition. To more accurately determine the time at which ignition occurred, relatively strong test mixtures were studied in the HPST so that the pressure trace exhibited an abrupt increase at ignition (see Fig. C.1).
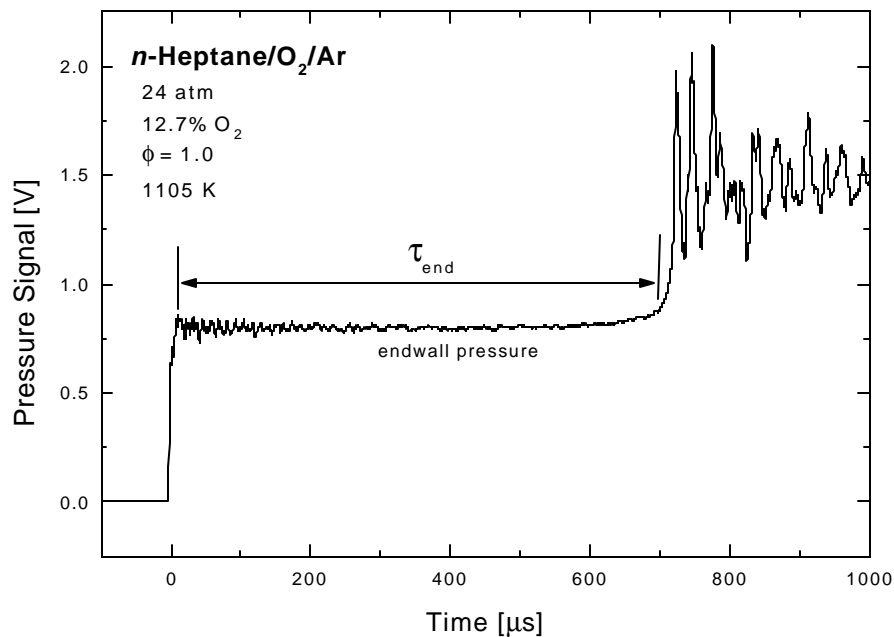
Fig. C.1 Endwall ignition time definition for the HPST study.

The method by which the fuel and additive test mixtures were prepared is as follows. For each test mixture, the n-heptane-additive molar ratio was set at 9 to 1. The stoichiometry of the mixture was then set to $\phi = 0.5$ based on the oxygen requirement of the fuel-additive mixture. The mixture strength was then set such that the total fuel-additive mole fraction was 0.60%. Due to the different stoichiometric oxygen requirements for each additive, the oxygen mole fraction of each fuel-additive test mixture varied from 12.3-13.3 % O_2.

The ignition time measurements obtained for each fuel-additive test mixture are compared to a baseline data set of *n*-heptane ignition time measurements (see Fig. C.2). Both DME and CPA are shown to have a weak inhibiting effect on the ignition delay of *n*-heptane, while IPN and DTBP were found to significantly accelerate the ignition process.
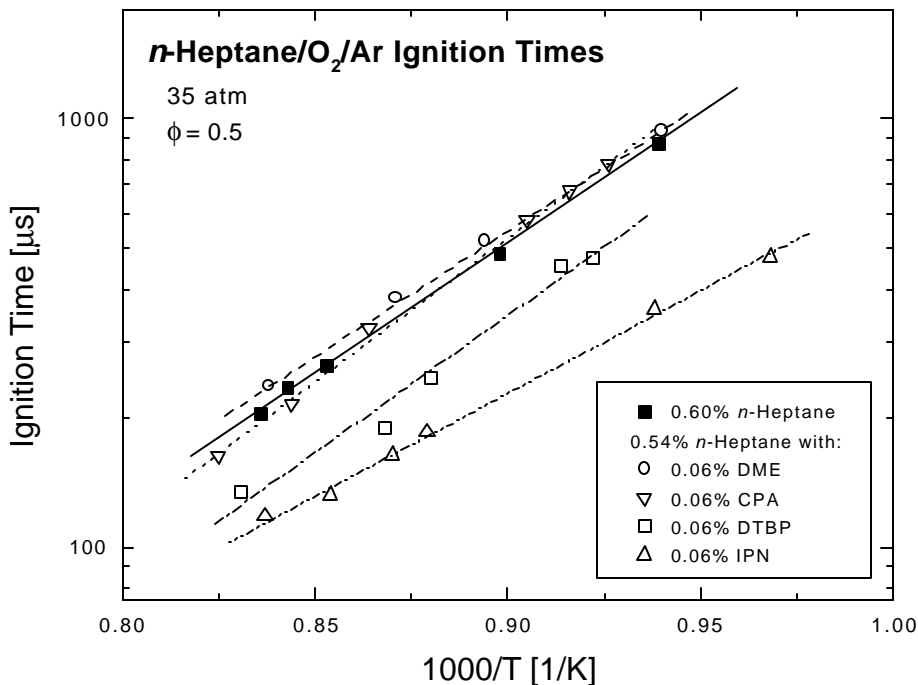

Fig. C.2 Effect of select additives on the ignition delay of *n*-heptane.

The accelerating effect of IPN and DTBP is likely a result of the rapid decomposition of the additive, which then facilitates the formation of the radical pool via the production of methyl radicals, as shown by the following decomposition reactions for IPN and DTBP, respectively.

$$i\text{-}C_3H_7ONO_2 \rightarrow CH_3 + NO_2 + CH_3CHO \qquad \text{[R C.1]}$$

$$(CH_3)_3COOC(CH_3)_3 \rightarrow 2CH_3 + 2(CH_3)_2CO \qquad \text{[R C.2]}$$
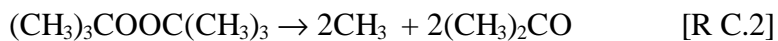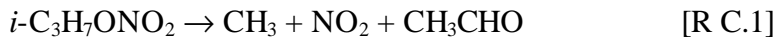
The formation of nitrogen dioxide (NO_2) from the decomposition of IPN may also enhance the ignition process by the following catalytic cycle,

$$NO_2 + H \rightarrow NO + OH \qquad [R\ C.3]$$

$$NO + HO_2 \rightarrow NO_2 + OH \qquad [R\ C.4]$$

for which the net effect is the production of two OH radicals for each H-atom consumed.

References

1. Siminski, V.J., Wright, F.J., Edelman, R., Economos, C., and Fortune, O, Technical Report AFAPL-72-24 Vol I and II, 1972.

2. Cavaliere, A., Ciajolo, A., D'Anna, A, Mercogliano, R., and Ragucci, R., *Combustion and Flame,* Vol. 93, 1993, 279-286.

3. Freeman, G. and Lefebvre, A. H., *Combustion and. Flame,* Vol. 58, 1984, 153-162.

4. Segal, C., Friedauer, M.J., Udaykumar, H.S., Shyy, W., and Marchand, A.P., *Journal of Propulsion and Power,* Vol. 13, No. 2, 1997, 246-249.

5. Siminski, V.J., and Wright, F.J., *AIAA*, Paper No. 72-71, 1972.

6. Spadaccini, L. J., and TeVelde, J. A., *Combustion and Flame,* Vol. 46, 1982, 283-300.

7. Minetti, R., Ribaucour, M., Carlier, M., and Sochet, L.R., *Combustion Science and Technology,* Vols. 113-114, 1996, 179-192.

8. Minetti, R., Carlier, M., Ribaucour, E., Therssen, E., and Sochet, L. R., *Combustion and Flame,* Vol. 102, 1995, 298-309.

9. Ribaucour, M., Minetti, R., and Sochet, L.R., *Twenty-Seventh Symposium (International) on Combustion*, The Combustion Institute, 1998, 345-351

10. Mohamed, C., *Combusiton and Flame,* Vol. 112, 1998, 438-444.

11. W.J., Westbrook, Curran, H.J., Pitz, C.K., Griffiths, J.F., Mohamed, C., and Wo, S.K., *Twenty-Seventh Symposium (International) on Combustion*, The Combustion Institute, 1998, 371-378.

12. Griffiths, J.F., Halford-Maw, P. A., and Mohamed, C., *Combustion and Flame,* Vol. 111, 1997, 327-337.

13. Inomata, T., Griffiths, J.F., and Pappin, A.J., *Twenty-Third Symposium (International) on Combustion*, The Combustion Institute, 1990, 1759-1766.

14. Halstead, M.P., Kirsch, L.J., and Quinn, C.P., *Combustion and Flame,* Vol. 30, 1977, 45-60.

15. Voinov, A.N., Skorodelov, D.I., Borisov, A.A., and Lyubimov, A.V*., Russian Journal of Physical Chemistry*, Vol. 41, 1967, 605-607.

16. Ryan, T. W., *SAE Transactions,* Paper No. 852103, 1985.

17. Ryan, T. W., and Callahan, T. J., *SAE Transactions,* Paper No. 881626, 1988.

18. Aradl, A.A., and Ryan, T.W., *SAE Transactions,* Paper No. 952352, 1995.

19. Siebers, D.L., *SAE Transactions,* Paper No. 852102, 1985.

20. Burcat, A., Farmer, R.F., and Matula, R.A*., Thirteenth International Symposium on Shock Tubes and Waves*, 1981, 826-833.

21. Colket, M.B., and Spadaccini, L.J., to be published in *Fourteenth International Symposium on AirBreathing Engines*, 1999.

22. Vermeer, D.J., Meyer, J.W., and Oppenheim, A.K., *Combustion and. Flame,* Vol. 18, 1972, 327-336.

23. Ciezki, H.K. and Adomeit, G., *Combustion and Flame,* Vol. 93, 1993, 421-433.

24. Coats, C.M., and Williams, A., *Seventeenth Symposium (International) on Combustion*, The Combustion Institute, 1979, 611-621.

25. Petersen, E. L., Davidson, D.F., and Hanson, R. K., *Journal of Propulsion and Power*, Vol. 15, No. 1, 1999, 82-91.

26. Burcat, A., and McBride, B., Technion Aerospace Engineering (TAE) Report # 804, June 1997.

27. Burwell, W. G. and Olson, D. R., *SAE Transactions*, Paper No. 650510, 1965.

28. Jaynes, D.N., and Beam, B.H., *Applied Optics,* Vol. 8, No. 8, 1969, 1741-1742.

29. Olson, D.B., Mallard, W.G., and Gardiner, W.C., *Applied Spectroscopy,* Vol. 32, No. 5, 1978, 489-493.

30. Zelson, L. S., Davidson, D. F., and Hanson, R. K., *Journal of Quantitative Spectroscopy and Radiative Transfer*, Vol. 52, 1994, 31-43.

31. Gutman, D., Hardwidge, E. A., Dougherty, F. A., and Lutz, R. W., Journal of Chemical Physics, Vol. 47, No. 11, 1967, 4400-4407.

32. Seery, D.J., and Bowman, C.T., *Combustion and Flame,* Vol. 14, 1970.

33. Brown, C.J., and Thomas, G.O., *Combustion and Flame,* Vol. 117, 1999, 861-870.

34. Burcat, A., Scheller, K., and Lifshitz, A., *Combustion and Flame,* Vol. 16, 1971, 29-33.

35. Tsang, W., and Lifshitz, A., *Annual Review of Physical Chemistry*, Vol. 41, 1990, 559-599.

36. Warnatz, J., *Twentieth Symposium (International) on Combustion*, The Combustion Institute, 1984, 845-856.

37. Burcat, A., Pitz, W. J., and Westbrook, C. K., *Eighteenth International Symposium on Shock Waves*, 1991, 771-780.

38. Burcat, A., Lifshitz, A., Scheller, K., and Skinner, G.B., *Thirteenth Symposium (International) on Combustion*, The Combustion Institute, 1971, 745-755.

39. Gray, J.A., and Westbrook, C.K., *Journal of Chemical Kinetics*, Vol. 26, 1994, 757-770.

40. Qin, Z., Lissianski, V.V., Yang, H., and Gardiner, W.C., to be published in *Twenty-Eighth Symposium (International) on Combustion*, The Combustion Institute, 2000.

41. Pfahl, U., Fieweger, K., Adomeit, G., and Gelfand, B.E., *Twentieth International Symposium on Shock Waves*, 1995, 1027-1032.

42. Ragland, K.W., and Garcia, C.F., *Combustion and Flame,* Vol. 18, 1972, 53-58.

43. Pfahl, U. and Adomeit, G., *Twenty-First International Symposium on Shock Waves*, 1997, 273-278.

44. Drummond, L.J., *Aust. Journal of Chemistry*, Vol. 21, 1968, 2641-2648.

45. Hidaka, Y., Kataoka, T., and Suga, M., *Bull Chemical Society Japan*, Vol. 47, 1974, 2166-2170.

46. Glassman, I., Combustion, 3rd Ed., Academic Press, San Diego, CA, 1996.

47. Marinov, N. M., Pitz, W. J., Westbrook, C. K., Vincitore, A. M., Castaldi, M. J., and Senkan, S. M., *Combustion and Flame,* Vol. 114, 1998, 192-213.

48. Held, T.J., Marchese, A.J., and Dryer F.L., *Combustion Science and Technology,*Vol. 123, 1997, 107-146.

49. Lindstedt, R.P., and Maurice, L.Q., *Combustion Science and Technology,* Vol. 107, 1995, 317-353.

50. Curran, H. J., Gaffuri, P., Pitz, W. J., and Westbrook, C. K., *Combustion and Flame,* Vol. 114, 1998, 149-177.

51. Hawthorn, R.D., and Nixon, A.C., *AIAA*, Vol. 4, 1966, 513-520.

52. Lindstedt, R.P., and Maurice, L.Q., *AIAA*, Paper No. 97-2836, Thirty-Third Joint Propulsion Meeting, Seattle, WA, 1997.

53. Smith, G. P., Golden, D. M., Frenklach, M., Moriarty, N. W., Eiteneer, B., Goldenberg, M., Bowman, C. T., Hanson, R. K., Song, S., Gardiner, W. C., Lissianski, V. V., and Qin, Zhiwei, http://www.me.berkeley.edu/gri_mech/.

54. Lifshitz, A., and Frenklach, M., *Journal of Physical Chemistry*, Vol. 79, No. 7, 1975, 686-692.

55. Hidaka, Y., Oki, T., and Kawano, H., *International Journal of Chemical Kinetics*, Vol. 21, 1989, 689-701.

56. Al-Alami, M. Z., and Kiefer, J. H., *Journal of Physical Chemistry*, Vol. 87, No. 87, 1983, 499-506.

57. Tsang, W., *Journal of Physical and Chemical Reference Data*, Vol. 17, No. 2, 1988 887-951.

58. Hautman, D. J., Santoro, R. J., Dryer, F. L., and Glassman, I., *International Journal of Chemical Kinetics*, Vol. 13, 1981, 149.

59. Pitz, W. J., Westbrook, C. K., and Leppard, W. R., *SAE Transactions*, Paper No. 912315, 1991.

60. Tsang, W., and Hampson, R. F., *Journal of Physical and Chemical Reference Data*, Vol. 15, No. 3, 1986, 1087-1279.

61. Tsang, W., *Journal of Physical and Chemical Reference Data*, Vol. 20, 1991, 221.

62. Leung, K. M., and Lindstedt, R. P., *Combustion and Flame*, Vol. 102, 1994,129-160.

63. Lindstedt, R. P., and Skevis, G., *Combustion and Flame*, Vol. 99, 1994, 551.